Adiabatic Motion and Dynamics of the Outer Radiation Belt

by

Daniel. E. da Silva

B.S., University of Maryland, College Park, 2014

M.S., Johns Hopkins University, 2021

A thesis submitted to the

Faculty of the Graduate School of the

University of Colorado in partial fulfillment

of the requirements for the degree of

Doctor of Philosophy

Department of Aerospace Engineering Sciences

2024

Committee Members:

Prof. Xinlin Li, Chair

Dr. Scot Elkington, Research Chair

Prof. Robert Marshall

Prof. Zoltan Sternovsky

Dr. Michael Wiltberger

da Silva, Daniel. E. (Ph.D., Aerospace Engineering Sciences)

Adiabatic Motion and Dynamics of the Outer Radiation Belt

Thesis directed by Prof. Xinlin Li

In this dissertation, we investigate the radiation belts as a dynamic system, paying particular attention to adiabatic motion and the related adiabatic invariant coordinate system. The theoretical foundations, based on classical mechanics and single particle plasma physics, are reviewed to provide a framework for the dissertation. With this foundation, we develop numerical methods to implement the calculation of adiabatic invariants from magnetic field models, being the first to do so in the literature with a concentrated focus on (a) rigorously documenting each computational step, (b) addressing significant sources of uncertainty, and (c) justifying selections of algorithm parameters. We apply these methods to quantifying the global adiabatic motion patterns of electrons in the outer radiation belt through a new computational method called invariant matching. These global adiabatic motion patterns are visualized as vector plots showing the displacement of mirror points throughout the magnetosphere. The plots display established features of radiation belt dynamics, such as the Dst effect, drift orbit bifurcation, and drift shell splitting. Finally, we combine four magnetic field models (two empirical and two magnetohydrodynamic) with observational satellite data from the Van Allen Probes. A study is designed to bolster existing results around the significant open question of what causes outer radiation belt electrons to accelerate to relativistic levels. Modern and highly cited results from the literature are reevaluated using the dissertation's rigorous tooling and, for the first time, multiple magnetic field models. By using multiple magnetic field models, this dissertation demonstrates that the results are generally model-independent, which strengthens the conclusion that acceleration is primarily (but not always) driven by whistler-mode chorus waves. This dissertation is tied together by the theory of dynamical systems, the development of rigorous numerical methodology, and the purpose of describing the causal dynamics of electron acceleration in the outer radiation belts.

Dedication

This dissertation is first dedicated to my wife, Antonya da Silva, whose loving guidance and support were essential to its completion. The second dedication is to my father, who gave me the inspiration to start.

Acknowledgements

Throughout my graduate academic career, I received significant support from people at CU Boulder, Johns Hopkins University, and NASA Goddard, who encouraged me to pursue my education to the highest level and excel in research.

I would first like to thank my advisors, Dr. Scot Elkington and Dr. Xinlin Li, for providing a supportive research environment from beginning to end. Finding my terrific advisors would not have been possible without the invaluable support of Dr. Barbara Thompson, who introduced me to Dr. Daniel Baker, through which Scot and I were encouraged to work together. During my studies, Dr. Anthony Chan, Dr. Mary Hudson, and Dr. Karlheinz Trattner also played crucial roles in creating a positive research atmosphere.

I would also like to thank the mentors I met before starting the PhD, who encouraged me to follow this path to completion. These include (in order of working together) Dr. Gregory Leptoukh, Dr. Christopher Field, Timothy Cole, Dr. Alex Barrie, Dr. Barbara Giles, Dr. Conrad Schiff, Dr. Li-jen Chen, Dr. John Dorelli, and Dr. Charles Nick Arge.

I would also like to acknowledge peers who have helped me find my place in research, including Dr. Jason Shuster, Dr. Christopher Bard, Dr. Michael Kirk, Dr. Shaela Jones, Dr. Raphael Attie, Dr. Shan Wang, Dr. Samantha Wallace, Dr. Nat Matthews, and Suhail Aldhurais.

Contents

Chapter

Tables

Table

Figures

Figure

Chapter 1

Introduction and Background

1.1 Basics of the Magnetosphere

The near-Earth space environment is a dynamic region governed by the dual influences of the Earth's magnetic field and the incoming solar wind. This introductory chapter will discuss the Earth's magnetic field, solar wind influences, and specific a magnetosphere component known as the radiation belts.

The magnetic field within the magnetosphere is often decomposed into two terms added together: the internal field and the external field. The internal field owes itself to currents interior to the Earth, while the external field owes itself to currents exterior to the Earth [64]. The internal magnetic field of Earth is largely generated by the motion of conducting liquid iron in Earth's outer core. This motion can be modeled as a magnetic dipole to a first-order approximation.

A mixture of permanent and transient currents in the magnetosphere generates the external field. To understand the current systems that contribute to the external field, we must first discuss the solar wind and its interaction with Earth. The solar wind consists of plasma material and an associated magnetic field streaming outward from the sun. Due to a plasma physics phenomenon known as the frozen-in condition, which occurs for certain regimes of the plasma β variable ($\beta = \frac{nk_BT}{B^2/2\mu_0}$ where n is the number density, k_B is the Boltzmann constant, B is the magnetic field strength, and μ_0 is the magnetic constant) the magnetic field becomes "stuck" to the plasma material and moves along with it [17]. With limited exceptions, the solar wind flow velocity is mainly radial. However, the solar wind magnetic field is not necessarily radial and broadly follows

a structure known as the Parker Spiral, which arises from rotation of the sun coupled with the frozen-in condition (exceptions to solar wind following the Parker Spiral owe to turbulence, shocks, and co-rotating interaction regions). At Earth, the solar wind number density is around 5-10 cm^{-3} with flow velocities between 400-700 km/s (again, with some exceptions, such as disturbances associated with coronal mass ejections).

When the solar wind reaches Earth, the plasma material and magnetic field which are both supersonic and super-alfvenic interact with Earth's magnetic field. Individual particles are shocked by the increasing magnetic field strength, forming a buildup region known as the magnetosheath. At the inner boundary of the magnetosheath, these particles broadly experience a deflection force and ultimately flow around the Earth's magnetic field. This abrupt bullet-shaped surface boundary between higher-density shocked solar wind particles and the lower density inside of the magnetosphere is known as the magnetopause. Due to charge-dependent forces acting on the individual particles at the magnetopause, a current is generated across this surface. This current, known as the magnetopause current or Chapman-Ferraro current, is one of the major sources that contributes to the external field[25]. Other major currents that contribute to the external field include the ring, Birkeland (polar), and tail currents.

Electromagnetic theory dictates that charged particles may become trapped in dipole-like magnetic fields. By saying this, we use the word "trapped" similarly to a moon being trapped by gravity around a planet or an asteroid being trapped around a star, but distinct in that the controlling forces are electromagnetic, and the trajectory is not a conic section. One such population of trapped charged particles is the radiation belts, which is the focus of this dissertation. James Van Allen initially discovered the radiation belts with the Explorer 1 satellite during the dawn of the space age in 1958. Shortly after, the theory of trapped charged particles was established to explain Van Allen's observations. The region was more extensively mapped using the Explorer 3, 4, and Pioneer 3 satellites during the following years.

During this time, it became established that the radiation belts consist of an inner belt and an outer belt: the inner belt composed of electrons and protons, and the outer belt primarily

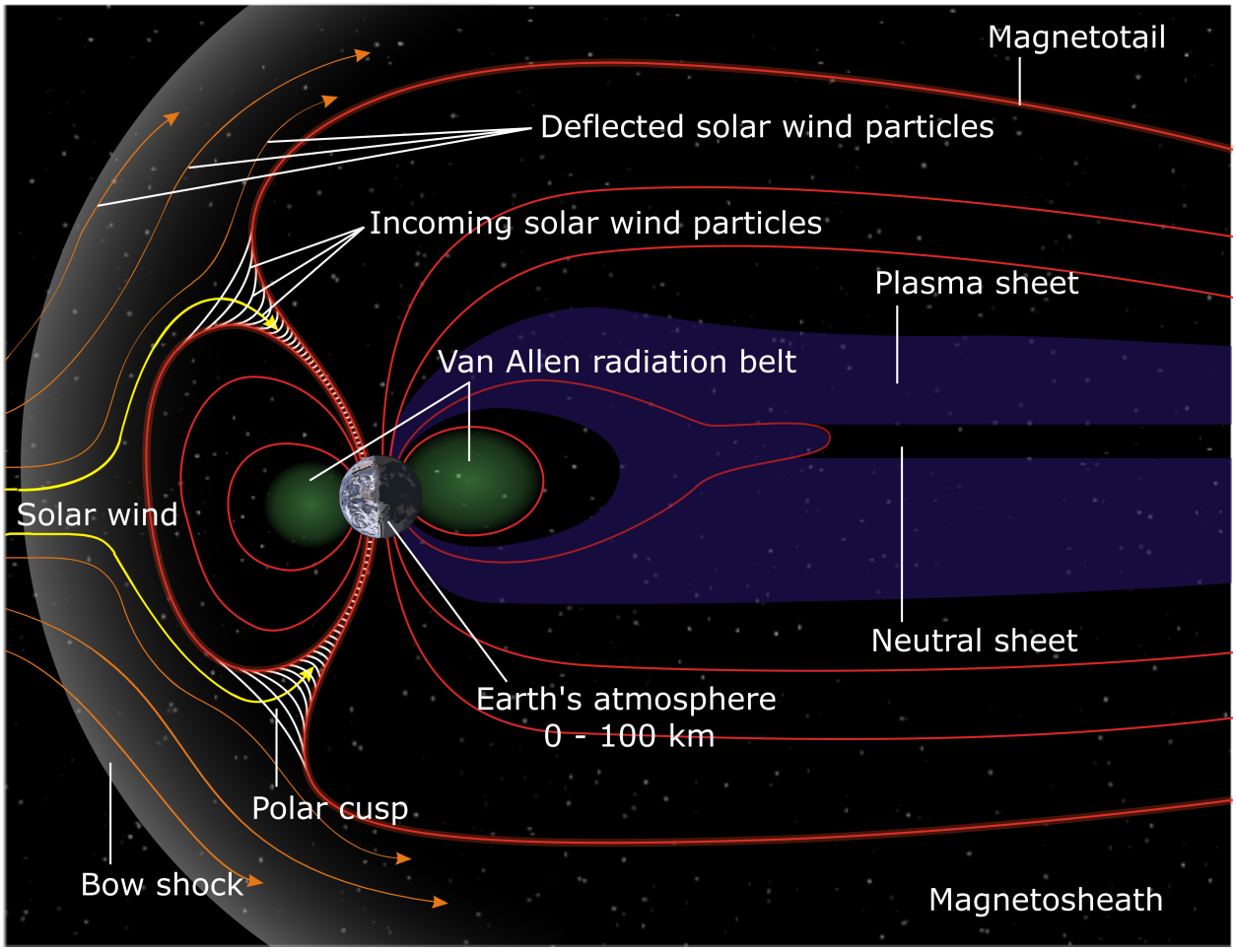

Figure 1.1: Illustration of Earth's magnetosphere and the structure therein. Image courtesy of the NASA/GSFC and Wikimedia Commons.

electrons. A significant observation from this period was that fluxes of each species increase and decrease in time, indicating what is now understood to be a signature of complex enhancement and loss processes. This display of complex dynamics led to the birth of the field of study known as radiation belt dynamics, which seeks to understand the radiation belts and the processes that occur in them as a dynamical system.

While interesting for academic reasons, studying the magnetosphere has significant practical applications. Advances in magnetospheric physics, including radiation belt physics, have made us realize the critical link between plasma in the near-earth space environment and technology. This applied, technology-focused field has since been known as Space Weather. Many technological effects are studied in space weather, and I will name but a few here relating to the radiation belts.

It is now well known that energetic particles impacting spacecraft may cause significant and detrimental effects on the spacecraft. Included in these damaging effects are:

- The accumulation of electric charge can result in electric discharges (sometimes known as "arcing"). These discharges, similar to very small lightning discharges, can damage electronic components on the aircraft and cause critical, irreversible damage. This phenomena is sometimes known as deep dialectric charging.

- Single event effects, which occur when charged particles impact circuits. This charged particle impact can "flip bits" and result in processors executing arbitrary routines (e.g., resets, attitude adjustment) or even trigger components into overdrawing current that ultimately damages electrons.

The international community studies space weather as spacecraft assets are increasingly central to the global economy. For more information on space weather and its effects on technology, the reader is referred to [72] and [20].

1.2 Trapped Particle Motion

The electromagnetic laws determining the trajectories of trapped radiation belt particles can be stated in a differential equation for single-particle motion. At the most direct, fundamental level, a charged particle in the radiation belts obeys the following differential equation,

$$m\frac{d\mathbf{v}}{dt} = q(\mathbf{E} + \mathbf{v} \times \mathbf{B}) + m\mathbf{g} \tag{1.1}$$

where $\mathbf{v}$ is the particle's velocity vector, m is the particle's mass, q is the particle's charge, $\mathbf{E}$ is the electric field vector, $\mathbf{B}$ is the magnetic field vector, and $\mathbf{g}$ is the acceleration due to gravity. Under uniform magnetic, a solution to this equation emerges known as gyromotion. In gyromotion, the particle follows a helix path where the radius of the helix (known as the gyroradius) is given by $r_g = mv_\perp/(|q|B)$ and the frequency of the circular motion (known as the gyrofrequency) is provided by $\omega_g = |q|B/m$. Gyromotion structure is also apparent in non-uniform fields, especially when the scale of the non-uniformity is large compared to the gyroradius and the scale of the time variation is large compared to the gyrofrequency.

Often, it is desirable to model the movement of the gyromotion helix without actually modeling the circular motion itself. This higher-level theory is known as *Guiding Center Theory*, where the equations of motion are written in terms of a guiding center state, which is that of the particle's trajectory averaged in a single circular loop of the gyromotion. The guiding center equations describe the drift of the entire gyromotion structure. The main forces we will discuss that act upon a particle in guiding center theory are known as (a) the $\mathbf{E} \times \mathbf{B}$ force (caused by the influence of the electric field), (b) the $\nabla_\perp B$ Force (caused by perpendicular gradients in the magnetic field strength), and (c) the $\nabla_\parallel B$ Force (caused by parallel gradients in the magnetic field strength) and the curvature drift (caused by curvature of magnetic field lines).

As previously stated, charged particles in a dipole-like magnetic field may become trapped. When this happens, they undergo three periodic motions throughout their trapped trajectory: (a) gyromotion about a field line, (b) bounce motion between off-equitorial "mirror points", and (c) drift motion about the Earth. These periodic motions necessarily emerge in the trajectory described

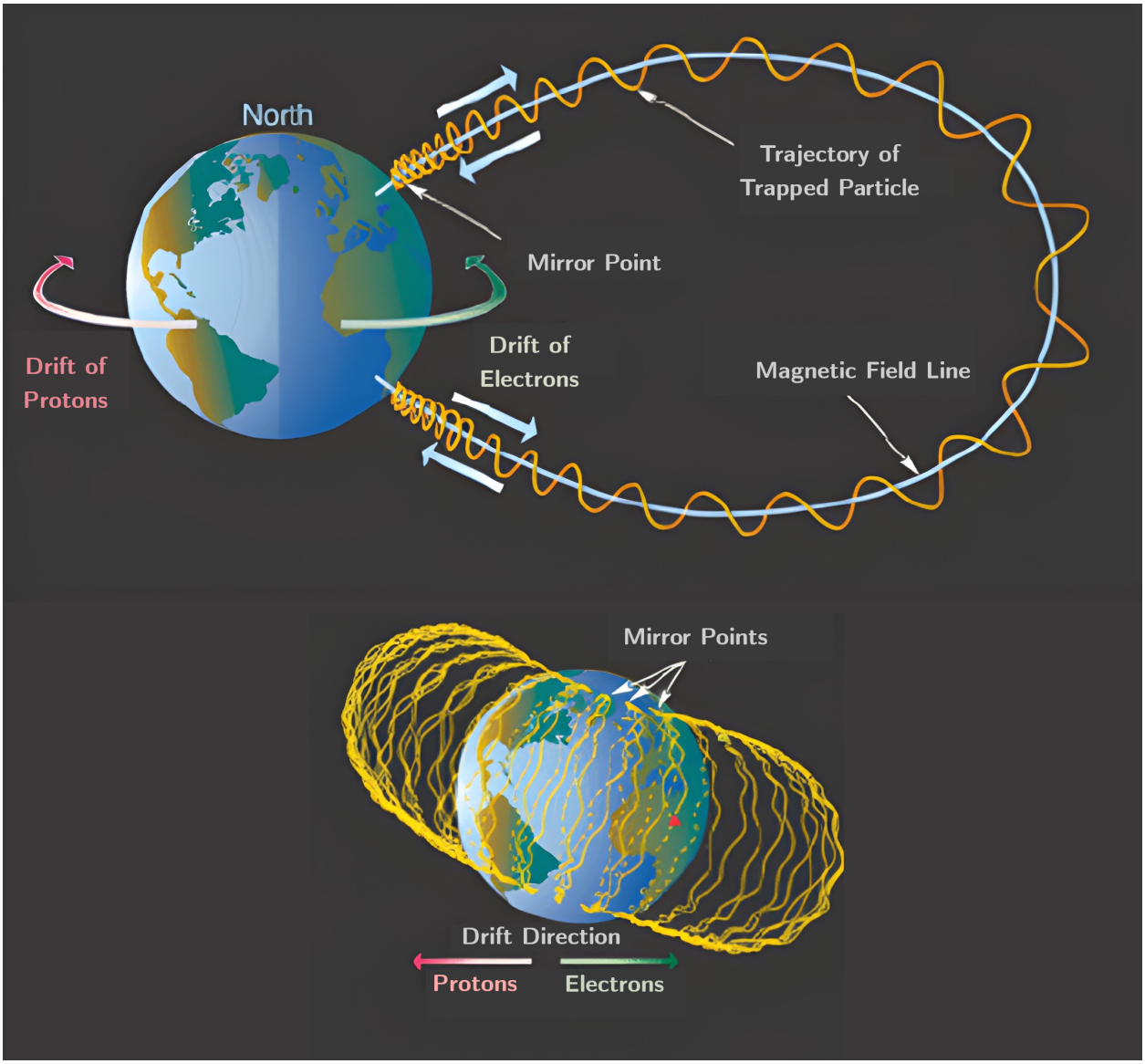

Figure 1.2: Illustration of the trapped motion of radiation belt particles. Image courtesy of Anagnostopoulos et al., 2010 [5] (with edits).

by Equation 1.1 when the particle is trapped. Of these three periodic motions, gyromotion occurs on the shortest time scale, and drift motion on the longest time scale.

Gyromotion is apparent in the motion of charged particles under most magnetic and electric field configurations. The occurrence of the bounce motion, however, is more circumstantial. The bounce motion is caused by the $\nabla_{\parallel}B$ force, which acts in a direction aligned with the guiding center vector. As the particle moves along the field line, the closer it gets to the Earth, the stronger the $\nabla_{\parallel}B$ force, which acts to decrease and eventually reverse the parallel velocity component. This causes the particle to "bounce" between fixed magnetic field strength endpoints. We note that the energy is conserved during this bounce motion, where $v_{\parallel}$ and $v_{\perp}$ trade-off values but the total v is constant. An illustration of a bounce motion can be found in the above Figure 1.2 in the orange line showing the trajectory of a bouncing particle.

The drift motion is primarily due to the $\nabla_{\perp}B$ force, which accelerates the particle in a direction perpendicular to the magnetic field line. The specific direction is given by $\frac{1}{q}(\mathbf{B} \times \nabla_{\perp}B)$, and we note that the factor of $1/q$ factor which carries a sign that causes protons and electrons to drift in opposite directions. This drift of charge in opposite directions induces an electric current and is the cause of a significant current system in the magnetosphere known as the ring current. The ring current is in a direction that depletes the Earth's magnetic field at the surface. This depletion of the magnetic field at the earth's surface is measured on the ground and reported to the international community through the Disturbance Storm-time (Dst) index. The strength of ring current, and in turn the magnitude of the field depletion at the surface, is related to the energy density of the trapped particle population through a phenomenon known as the Dessler-Parker-Sckopke (DPS) relation [34, 105].

1.3 Adiabatic Invariants Basics

To fully understand the nature of a trapped particle, we must also consider how it is affected by global changes to the magnetosphere's magnetic and electric fields. Well-understood changes to the magnetic field in the magnetosphere include (a) the compression of the dayside magnetic field

structure in response to increasing solar wind dynamic pressure P_{dyn} (b) convection of field lines driven by a magnetic reconnection (an interaction between the solar wind and the magnetosphere), and (c) changing intensities of currents which add a new deviation to the existing magnetic field.

Overall, trapped particles generally remain trapped unless the particle is absorbed by the inner boundary (Earth's ionosphere) or its outer boundary (the magnetopause). Major known outside forces that change trapping include those associated with stochastic motion of particles known as radial diffusion. Changes to the field that can cause loss include magnetopause incursion and outwards transport of particles through the magnetopause [58, 112, 113].

Through the development of classical mechanics, it is known that any system with one or more periodic motions has a constant quantity along each motion, which can be derived from the Hamilton-Jacobi action integral [103],

$$J_i = \oint [\mathbf{p} + \left(\frac{q}{c}\right) \mathbf{A}] \cdot d\mathbf{s}_i, \tag{1.2}$$

where $\mathbf{p}$ is the particle momentum, $\mathbf{A}$ is the vector potential, q is the particle charge, and c is the speed of light. We call these constants of motion *adiabatic invariants* when two conditions are met [26]. First, there must be a specific set of reversible changes to the system, and they must occur slowly compared to each periodic motion, and within small spatial scales compared to the periodic motion. In our context, these reversible changes are changes in the magnetic field compared to the periods of gyromotion, bounce motion, and drift motion. Second, the exact trajectories of the periodic motions, $(\mathbf{x}(t), \mathbf{p}(t))$, must be altered with the changes to the system, but in a way such that work is not done.

Adiabatic invariants are powerful tools when used to describe the trapped state of a radiation belt particle. When the exact trajectory of a radiation belt population is altered due to slow changes to the magnetic field, the adiabatic invariant coordinate remains constant, and the shift in the trajectory is *reversible adiabatic motion.* If the magnetic field deviates from a nominal state and then returns to its nominal state, so does the particle's trajectory. This is worth contrasting to

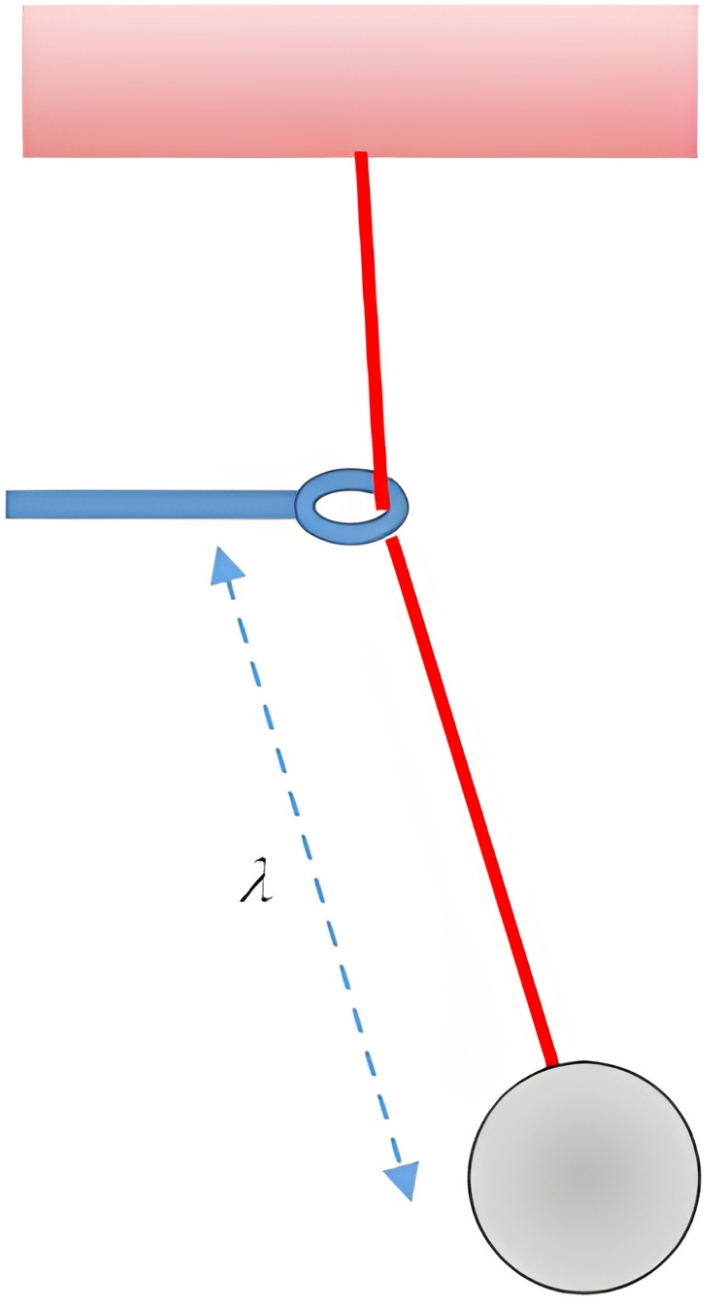

Figure 1.3: Example of 1-D Periodic System with a constant of motion (conserved when λ is changed slowly). Image courtesy of Prof. Michael Fowler, University of Virginia.

irreversible non-adiabatic motion, which alters the particle trajectory, such as in the case of wave-particle interactions on temporal or spatial scales commensurate with one of the periodic motions. Therefore, the adiabatic invariant description serves as a more vital state variable, capturing the essence of the trapped nature in a way that is resistant to slow changes to the global magnetic fields.

There is one adiabatic invariant for each periodic motion. The canonical adiabatic invariants are often denoted by (M, J, Φ), corresponding to the gyromotion, bounce motion, and drift motion, respectively. The community has widely adopted an alternative form of (M, J, Φ), denoted (M, K, L^*). The coordinates (M, K, L^*) can be calculated directly from (M, J, Φ) (and are equivalently invariant) but provide several convenient and desirable properties over their predecessors. We also note that the first invariant M has a non-relativistic counterpart μ, related by the equation $M = \gamma\mu$, where γ is the Lorentz factor and μ is the magnetic moment of the particle. The magnetic moment μ is an adiabatic invariant only in non-relativistic scenarios.

The second invariants J and K are related through the following equations taken from [100],

$$K = J/(2\sqrt{2m_0 M}) = \int_{s_1}^{s_2} \sqrt{B_m - B(s)}\, ds. \tag{1.3}$$

The primary advantage of K is that it can be computed directly from a field line trace as it depends on $\mathbf{B}$ alone. In contrast, calculating J requires tracking the particle's exchange of parallel and perpendicular momentum over a bounce. We note, however, that K is only invariant if there are no parallel forces over the bounce path (this is not true for J). The adiabatic invariant Φ is identical to the magnetic flux through the drift orbit. The more convenient form of Φ is the dimensionless L^*, defined as

$$L^* = 2\pi\mu_E R_E^2/\Phi \tag{1.4}$$

where μ_E is the magnetic moment of the Earth and R_E is the radius of the Earth. L^* has the desirable property that in a dipole field, a particle found on an L-shell L will have $L^* = L$. This allows L^* to be used as a reference in comparison to L. Subsequently, the occurrence of particles

found on an L-shell L with $L^* > L$ or $L^* < L$ indicates that the magnetosphere has deviated from a dipole in such a way that the particle underwent outwards or inwards adiabatic motion, respectively, as a result of the magnetospheric reconfiguration. This is in contrast to the cause necessarily and solely being due to non-adiabatic transport from work done by wave-particle interactions, such as betatron/Fermi acceleration [22, 138, 46, 57].

The equations for the adiabatic invariants are summarized below,

$$M = \frac{p_\perp^2}{2m_0 B} = \frac{p^2 \sin^2(\alpha)}{2m_0 B} \tag{1.5}$$

$$K = \int_{s_1}^{s_2} \sqrt{B_m - B(s)} ds \tag{1.6}$$

$$\Phi = \int_\Pi \mathbf{B} \cdot d\mathbf{S} \approx B_E R_E^2 \int_0^{2\pi} \sin^2(\theta(\phi)) d\phi \tag{1.7}$$

$$L^* = \frac{2\pi B_E R_E^2}{\Phi} \tag{1.8}$$

where p is the relativistic momentum, α is the pitch angle, B_m is the magnetic field mirror strength, θ is the colatitude of the drift shell field line footpoint, ϕ is a magnetic local time in units of radians, B_E is the magnetic field strength of the earth at the surface, and R_E is the radius of the earth.

With such a coordinate for each particle, the trapped phase space density defined as the number of particles per unit volume per momentum, $f(\mathbf{x}, \mathbf{p})$ is equivalent to $f(M, K, L^*, \varphi_1, \varphi_2, \varphi_3)$, where φ_1, φ_2, and φ_3 are the phases associated with each periodic motion for M, K and L^* respectively. In practice, the phase space distribution is largely not phase-dependent, so it is accepted to recast $f(M, K, L^*, \varphi_1, \varphi_2, \varphi_3)$ as the phase-averaged distribution $\bar{f}(M, K, L^*)$. The main advantage of the phase-averaged distribution is that it only has three dimensions compared to the six dimensions prior (not counting time).

To study the charged particle populations of the radiation belts, particle flux distributions are measured in-situ by spacecraft instrumentation [79, 39]. By combined count rates and instrument calibration parameters, the particle's momentum, and the spacecraft's orientation/position, velocity distributions in the form of $f(\mathbf{x}, \mathbf{p})$, $f(\mathbf{x}, \alpha, W)$ or $f(x, \phi, \theta, W)$ can be collected [100]. In these expressions $\mathbf{x}$ is the position in space, $\mathbf{p}$ is the particle relativistic momentum, α is a pitch angle

Table 1.1: Magnetospheric Waves Relating to Radiation Belt Dynamics

Name	Type	Source
Whistler-mode Chorus	Electromagnetic	Electron Temperature Anisotropies
Alfvenic	Plasma (Magnetohydrodynamic)	Shocks / Kelvin Helmholtz
Magnetosonic	Plasma (Magnetohydrodynamic)	Magnetopause Motion
Hiss	Electromagnetic	Chorus waves propagating inside plasmasphere, and lightning (when seen in L under 3)
EMIC (Electromagnetic ion cyclotron)	Electromagnetic	Ion Temperature Anisotropies

between $\mathbf{p}$ and $\mathbf{B}$, W is a particle energy, and ϕ/θ are the azimuthal/elevation look directions. From these base forms of the distribution function, missions studying radiation belt dynamics will convert the distribution function to $f(M, K, L^*)$ to aid scientific analysis.

1.4 Wave Particle Interactions

The magnetosphere is home to much-varied wave activity in the form of electromagnetic and plasma waves. Waves that interact with a particle can alter the particle's trajectory. The primary method of doing work on a particle in the magnetospheric context is through *resonant interactions*, wherein particles interact with waves of frequencies commensurate with particle gyro, bounce, or drift motions.

The most influential types of magnetospheric waves are listed for background in Table 1.4. While many other types of waves exist in the magnetosphere, these are believed to be the most important in determining the radiation belt dynamics relevant to the science questions mentioned later in this paper. In radiation belt dynamics, wave-particle interactions are generally considered the primary source of work done on the particles. As we study radiation belt dynamics, we consider the influence of these waves and their varying spatial, temporal, and directional occurrences as drivers that change the state of the global system [119].

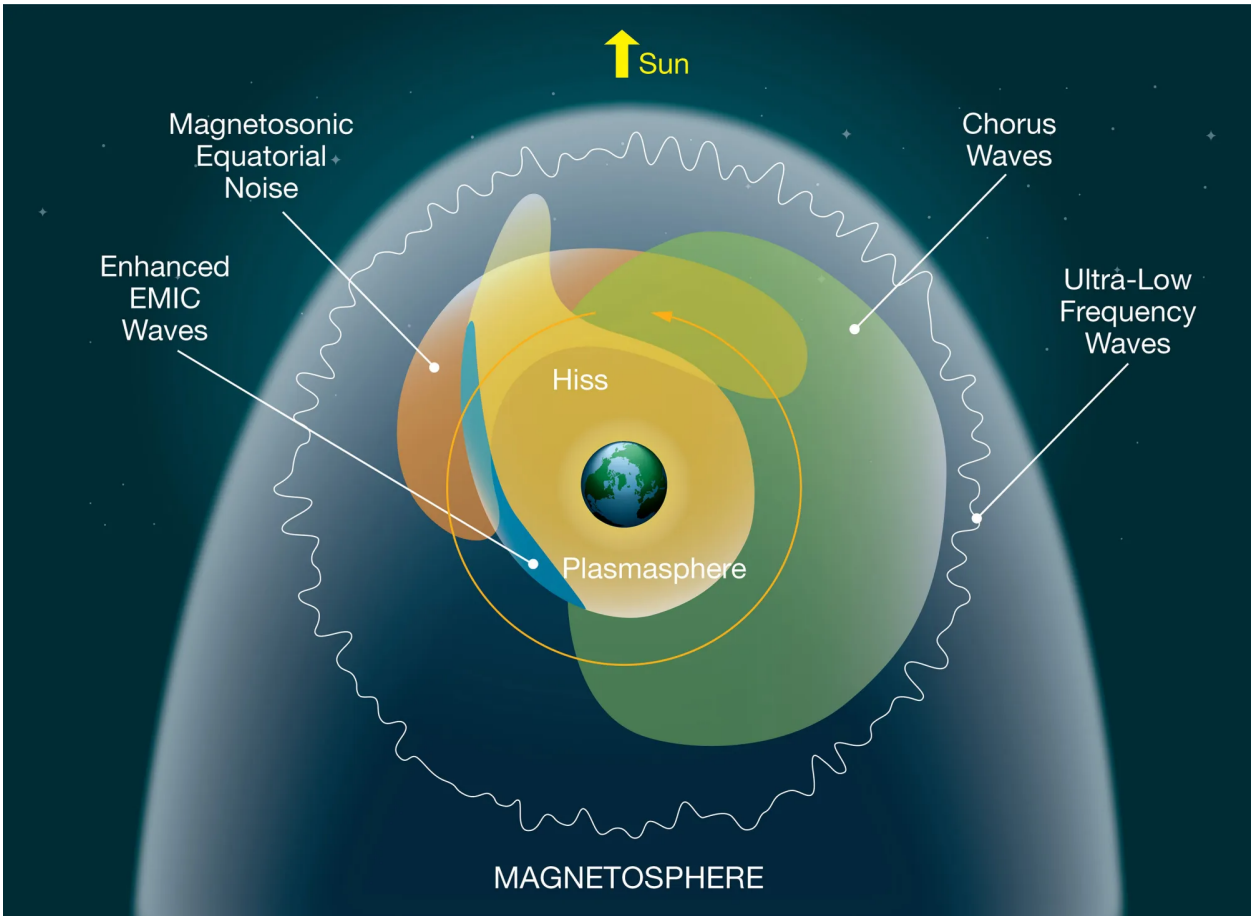

Figure 1.4: Illustration of different types of magnetospheric waves and where to find them. Image courtesy of NASA.

1.5 Dynamics of Outer Radiation Belt Electrons

The outer radiation belt is home to fluxes of energetic (MeV) electrons, notably due to their presence alongside critical spacecraft assets vulnerable to adverse side effects from energetic particle impacts. The variability over time of such electron fluxes is known to span many orders of magnitudes. While the fundamental periodic motion of these trapped particles is understood [100], many open questions around the processes involved in their acceleration and loss remain [98, 46].

Many candidate mechanisms that could affect the radiation belt populations have been identified. Loss is generally understood to occur (a) from precipitation into the atmosphere or loss to a steady magnetopause, forced by diffusive changes to the distribution function from wave-particle interactions, or (b) abrupt changes to the magnetopause location that remove particles from their trapped trajectories ([58]) .

Acceleration is understood to arise from two families of wave-particle interactions, distinguished by the time-varying patterns in the global distribution of trapped particle states. These two patterns are *radial transport* and *local acceleration* [46, 22]. Radial transport (including forms referred to as *external acceleration or radial diffusion* in the literature) is understood to occur from Ultra Low Frequency (ULF) wave-particle interactions, which move particles across L-shells faster than the particle's drift can adiabatically adjust, causing the particle energy to increase to preserve its first invariant in a stronger magnetic field. Local acceleration (sometimes referred to as *growing peak acceleration or internal acceleration* in the literature) is most often driven by gyro-resonant waves (such as chorus) and accelerate particles at their existing locations around $L < 6.6$ [54, 120]. The question of which mechanisms accelerate electrons is further complicated by the possibility that a mix of mechanisms may exist simultaneously, with recent work suggesting that internal acceleration may be dominant for some energy ranges (3–5 MeV electrons) while radial transport may be dominant for others ($\sim$7 MeV) [149].

The observational study of outer radiation belt electron enhancements is made difficult due to the changing global magnetospheric magnetic field. The directly observed flux distribution is

typically measured in the form $j(E, \alpha; \mathbf{x}, t)$, where j is the flux, E is the electron energy, α is a local pitch angle, $\mathbf{x}$ is the location of the spacecraft, and t is the time of measurement. Even without accelerating wave-particle interactions, a particle measured at a local time with distribution coordinate (E, α) may never return to that local time with the same (E, α). This is due to adiabatic changes to its cartesian trajectory, pitch angle, and drift shell from changes to the global magnetospheric magnetic field. For reasons such as these, studies tracking immediate observable such $j(E_0, \alpha_0; \mathbf{x}, t)$, where E_0 is a fixed energy and α_0 is a fixed local pitch angle, are severely limited.

Instead, combining the global magnetospheric magnetic field modeling with observation has become common by casting the flux in terms of adiabatic invariant coordinates. These coordinates function as an underlying measure of the trapped state and remain constant provided the global magnetospheric magnetic field changes slowly compared to the drift period. The conversion of flux to phase space density and recasting of the coordinates in terms of adiabatic invariants is known as *phase space density analysis*, which results in the model-supplemented measurement $f(M, K, L^*)$, and is discussed in detail in Chapter 4.

A long-term principle question that this dissertation aims to address is that of what causes electron acceleration in the outer radiation belts. The leading method of addressing this question is through phase space density analysis. In this style of analysis, different proposed mechanisms are reasoned using fundamental physics to generate different structural changes in the time-dependent $f(M, K, L^*; t)$, and spacecraft measured $f_{obs}(M, K, L^*; t)$ are compared against those anticipated structural changes. Illustrations of anticipated structural changes in f are displayed in Figure 1.5 for magnetopause loss and in Figure 1.8 for acceleration mechanisms.

This method of analysis has been implemented using POLAR spacecraft in-situ data in e.g. [46, 106], and Van Allen Probes in-situ data in e.g., [99, 22]. In [46] and [22], a large number of events were analyzed and it was found that the structural changes in $f_{obs}(M, K, L^*)$ were most commonly aligned with local acceleration driven by chorus wave activity. In addition, the work of Allison et al., 2021 [3] provided a detailed analysis of the peaks in phase space density that corresponded

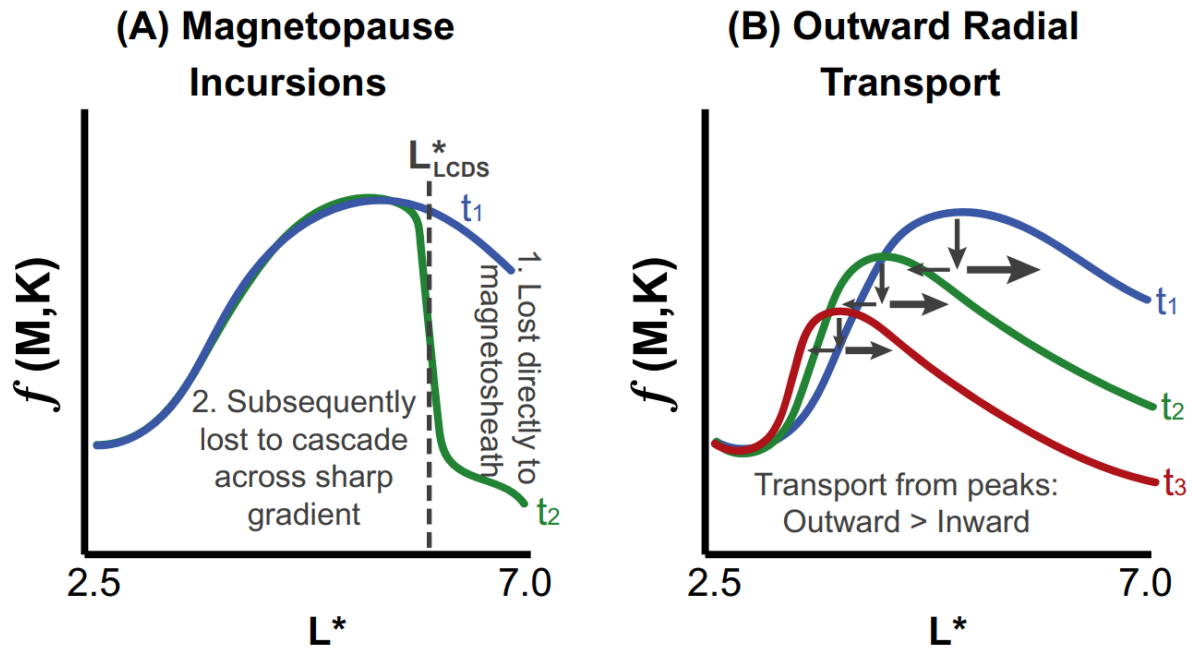

Figure 1.5: Signatures of two forms of the magnetopause loss phenomena. Image courtesy of Jaynes et al. 2019 [58].

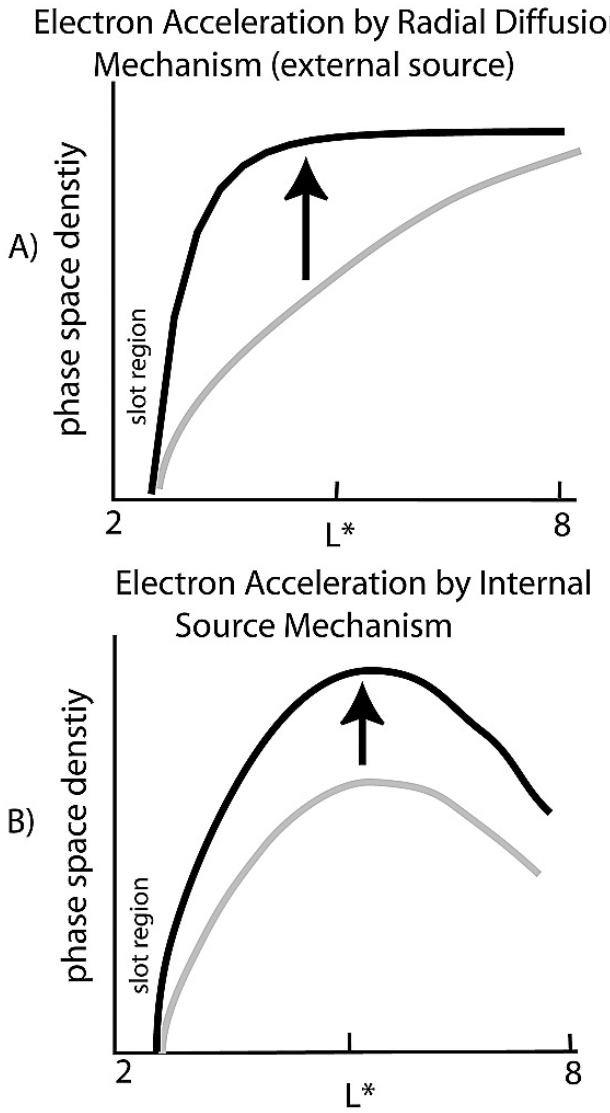

Figure 1.6: Signatures of two phenomena associated with the acceleration of outer radiation belt electrons. Image courtesy of Green et al., 2004 [46].

to the multi-MeV electrons. It was noted by Boyd et al., 2018 that chorus acceleration was only the case for 87% of the events, leaving uncertainty as to alternative mechanisms which, while the minority, still play a role in electron acceleration overall. The question as to what happens when evidence for local acceleration is absent is complicated by the fact that during these times, multiple mechanisms may be occurring simultaneously, possibly with secondary interactions.

In these studies, $f_{obs}(M, K, L^*)$ was computed using Tsyganenko empirical models, and Green et al., 2004 [46] warns as to the model-dependent nature of the calculation. In Chapter 4, we will implement phases space density analysis with multiple models, including magnetohydrodynamic (MHD) models. Immediate questions to come from the methods developed here of extending adiabatic invariant calculation to MHD models are (a) are the previous results in the literature reproducible when the invariants are calculated from MHD models? and (b) what is available in the global MHD model context (such as wave activity and, more generally, ρ, $\mathbf{u}$, p, and $\mathbf{E}$) that can inform us as to what physics may be simultaneously occurring that affects the acceleration?

1.6 Instruments and Data

Measurements of the magnetosphere date back to the earliest ground measurements of Earth's magnetic field. However, in-situ measurements of the radiation belts from space only began during the dawn of the space age, when the radiation belts were first discovered by John Van Allen in 1958 with instruments on board the the Explorer 1 spacecraft.

Spacecraft designed for the specific purposes of collecting scientific data are scientific experiments in themselves. To study complex scientific phenomena, and in particular phenomena of plasma physics in the magnetosphere, an assortment of parameters are necessary to fully describe plasma state in a way that provides closure on science questions [60]. The design and implementation of each scientific instrument– often a deep and challenging engineering problem in itself– centers around the science questions it aims to answer and, more specifically, the variables and ranges of values it expects to encounter.

In this study, we use data from Van Allen Probes Energetic Particle, Composition, and Ther-

mal Plasma (ECT) suite [117]. Specifically, we use the Level-3 RBSP-ECT Combined Pitch Angle Resolved Electron Flux Data Product [21]. This Level-3 dataset bins the data into three-minute time resolution and inter-calibrates the multiple ECT instruments of the (a) Helium, Oxygen, Proton, and Electron (HOPE) [43], (b) Magnetic Electron Ion Spectrometer (MagEIS [18]), and (c) Relativistic Electron Proton Telescope (REPT [11]). While the dataset includes precomputed values for invariants I and L^* using the Olson & Pfitzer Quiet-time Model for the external field [91] and the International Geomagnetic Reference Field (IGRF; [78]) calculated using LANLGeoMag software [52], we do not use those. We also use data from the Van Allen Probes magnetometer, Electric and Magnetic Field Instrument Suite and Integrated Science (EMFISIS; [65]). Specifically, we use the 4-second time resolution data product [24].

In this dissertation, we also use data from the GOES-13 satellite to provide magnetometer measurements from geosychronous orbit. This geosynchronous orbit sits at a fixed 6.6 R_E radial distance from Earth, which makes GOES a valuable monitor for the outer radiation belt.

1.7 Modeling and Simulation

Magnetic field models of the earth are essential tools which describe the magnetic field vector throughout the magnetosphere. As we seek to understand the changing trajectory of a particle in the context of the fields it exists in, it is essential to know what those fields are and how they change.

One type of these magnetic field models are the empirical models, which have been constructed since early in the space age. These models combine physical insight about the current structures throughout the magnetosphere with averages of spacecraft measurements, often collected from multiple satellites over decades. These two modeling paradigms (physical structure and observation) are combined to provide $\mathbf{B}(\mathbf{x})$ as a function of some geophysical state. This geophysical state is typically the solar wind magnetic field components, the solar wind dynamic pressure ($P_{dyn} = \rho v^2$ where P_{dyn} is the dynamic pressure, ρ is the solar wind mass density, and v is the solar wind flow velocity) , and a geomagnetic activity indicator such as Dst, K_p, or the

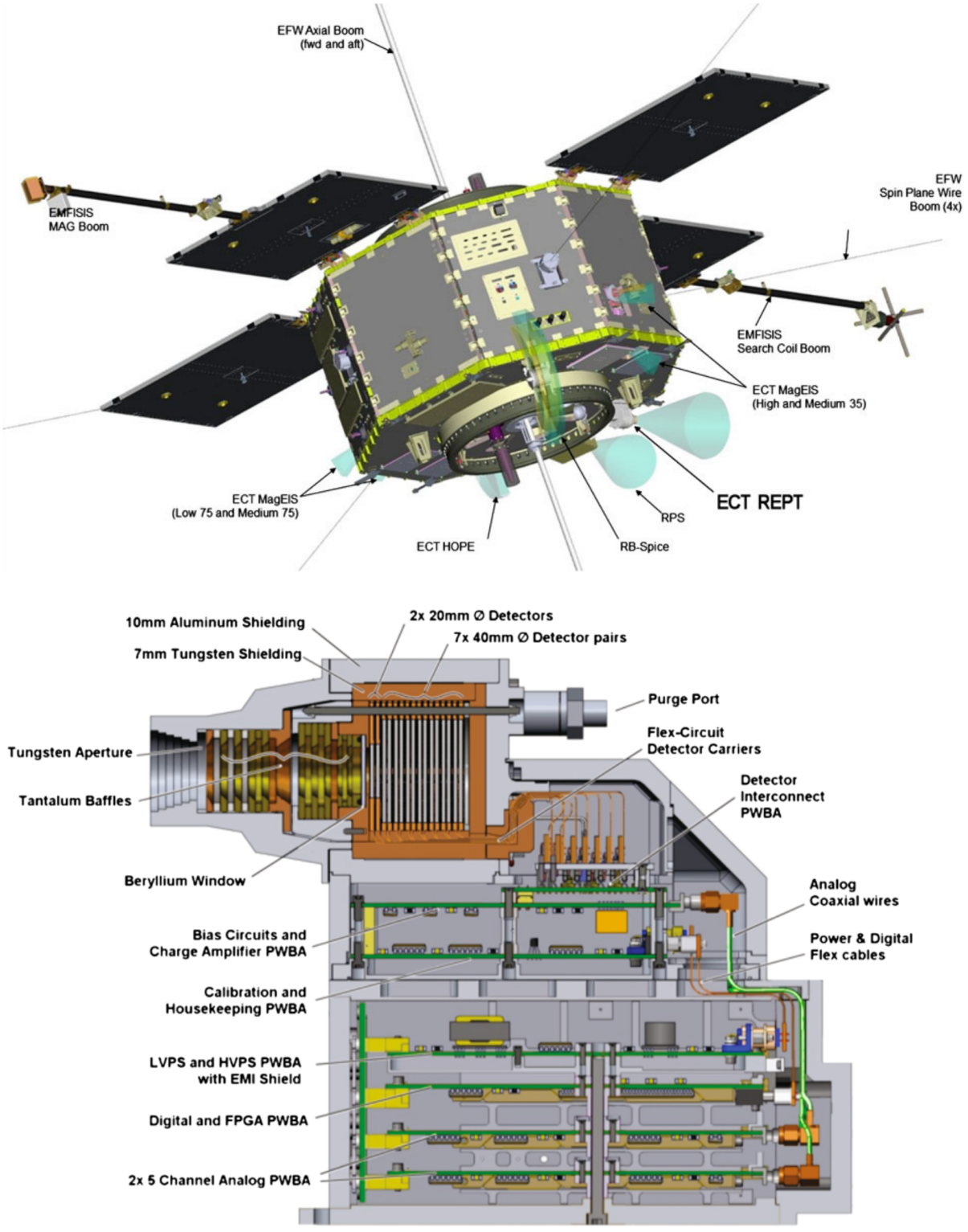

Figure 1.7: Top: A Van Allen Probes spacecraft with the location of each instrument labeled. Bottom: Design schematics of the REPT instrument. Images courtesy of Baker et al., 2014 [11].

Auroral Electroject (AE) index. The strengths of these models are their ability to capture large-scale features such as dayside compression and tail stretching. However, the semi-empirical models are typically instantaneous "snapshots" which lack time-dependent shock physics and generally do not include field perturbations due to waves. The main family of semi-empirical models we use are the Tsyganenko and Tsyganenko/Sitnov models, named by the year they were released: T89[132], T96[134], and TS05 [131]. Other empirical models we do not use, but have been significant historically, include Olson & Pfitzer (Quiet / Dynamic), Alexeev, Ostapenko & Maltsev, and Mead & Fairfield.

Of the Tsyganenko models, T96 and TS05 are used in this dissertation. Both are driven by a combination of interplanetary magnetic field (IMF) and Dst index measurements, but the TS05 model is also driven by by precomputed "W" parameters, $W_1 - W_6$. These W parameters model persistence in the magnetosphere, such as that associated with buildup of the ring current during a geomagnetic storm. Throughout this work, the IMF and W parameters used are supplied by the 5-minute time resolution Qin-Denton dataset, hosted at George Mason University.

A more sophisticated, albeit computationally expensive, class of magnetospheric magnetic field models is that of full-scale MHD simulations. MHD is a theory of time-dependent plasma dynamics in the continuum limit, where the plasma density, temperature, flow velocity, and pressure are modeled as a continuum. In a very simple sense, MHD is to continuum plasma physics what the Navier Stokes equations are to continuum fluid dynamics (although the emergent, qualitative features of each system often differ drastically). Like the Navier Stokes equations, MHD is commonly simulated with finite volume simulations, adapted or adaptive grids, and large parallel supercomputer solvers. MHD simulations are capable of capturing large-scale features of the magnetosphere, including dayside compression, tail stretching, separation of regions, dynamic time-varying currents, and MHD plasma waves.

However, MHD simulations are not without limitations. Foremost, MHD, by design, cannot model particles at high energies outside the Maxwellian (thermal) bulk. This is notable for this dissertation because radiation particles are such particles. However, MHD simulations *can* provide

the global magnetic and electric fields which the radiation particles exist in, as the feedback inserted from the current of radiation belt particles is generally negligible.

This dissertation uses multiple MHD simulation models, including the Lyon–Fedder–Mobarry code (LFM; [77]) and the Space Weather Modeling Framework (SWMF; [122]). Other notable models that exist in the community but are not implemented here include the Open Geospace General Circulation Model (OpenGGCM; [97]) and the Grid Agnostic MHD for Extended Research Applications (GAMERA; [148]).

To create more realistic simulations in areas where the MHD equations may not be appropriate, simulations often couple MHD solvers with other models on a region-by-region base. In our work, the most prominent example of this is a specialized multi-fluid formalization for the ring current known as the Rice Convection Model (RCM [121, 94]). In this work, LFM and SWMF are both coupled with comparable implementations of RCM and are sometimes referred to as LFM-RCM and SWMF-RCM when an emphasis on coupling is desired.

Many of the simulation runs used here were performed using the Community Coordinated Modeling Center (CCMC) Run-on-Request system (`https://ccmc.gsfc.nasa.gov/`), which is a service provided by NASA to perform simulation runs for the public. The 2023 version of SWMF was used, with the auroral ionosphere conductance setting and no corotation velocity applied at the inner boundary. The SWMF simulation was performed on a grid with 4,873,456 cells with 1/8 R_E resolution at the inner boundary. The LTR-2_1_5 version of LFM was used, with the auroral ionosphere conductance setting and no corotation velocity applied at the inner boundary. The LFM simulations used were performed on a grid with 1,302,528 cells (106×96×128), sometimes called "Quad" resolution. The inner boundary for LFM simulations is at 2.1 R_E, with the full computational domain extending from +30 R_E to -300 R_E along the sun-earth line (SM x-axis) and from -150 R_E to +150 R_E along the SM y-axis and z-axis.

The LFM and GAMERA simulations operate on a static and structured grid specially designed for magnetospheric applications. While each cell contains six faces and an associated connection to neighbors at each, the spatial density of cells is not uniform. These simulations strategically

place more cells in the inner magnetosphere and bow shock where increased resolution is desired to capture the desired physical information. Fewer cells are placed in the magnetotail, where the physical phenomena that arise there do not demand increased resolution. We note that while LFM and GAMERA use similar grids, they are not one-for-one identical.

The SWMF simulation model uses a different approach to resolution. The component of the SWMF simulation, which evolves the MHD state, is named Block-Adaptive Tree Solarwind Roe-type Upwind Scheme (BATS-R-US; [123]). BATS-R-US uses a block-adaptive grid, where the resolution in different parts of the domain is determined at run time as a function of the physical state. As a result, the output of SWMF and BATS-R-US is therefore not a typical n-dimensional array as is the case with LFM and GAMERA; it is a tree structure where each cell of a nominal grid is optionally further represented by sub-cells (and so-on recursively).

In this dissertation, the tools we will develop will require the magnetic field to be specified on a structured grid. At first, this is not the case for the T96 and TS05 models: the models themselves provide $\mathbf{B}(\mathbf{x})$ at arbitrary input locations; it is also not the case for SWMF as the data is in a tree structure. To use these models with the code developed for a structured grid, unless otherwise noted, these models were evaluated or regridded to a specific rectilinear grid. The specifications of the rectilinear grid were such that each X, Y, and Z axes were between -10 R_E and +10 R_E with a grid spacing of 0.15 R_E. This outer boundary of $\pm$ 10 R_E is safely outside the Van Allen Probes apogee of 5.8 R_E, to accommodate the times when combination with Van Allen Probes data is needed.

To regrid the SWMF model output, an averaging method was used. For each grid cell center in the rectangular grid, points from the SWMF model output within a spherical neighborhood of that grid center were averaged using a weighting scheme that gave preference to points closer to the grid cell center. That average value then became the value of the rectangular grid at that grid cell center.

Throughout this dissertation, experimentation was done with the grid resolution, and it was found that using a lower grid resolution did not change the results of this work. For a visual

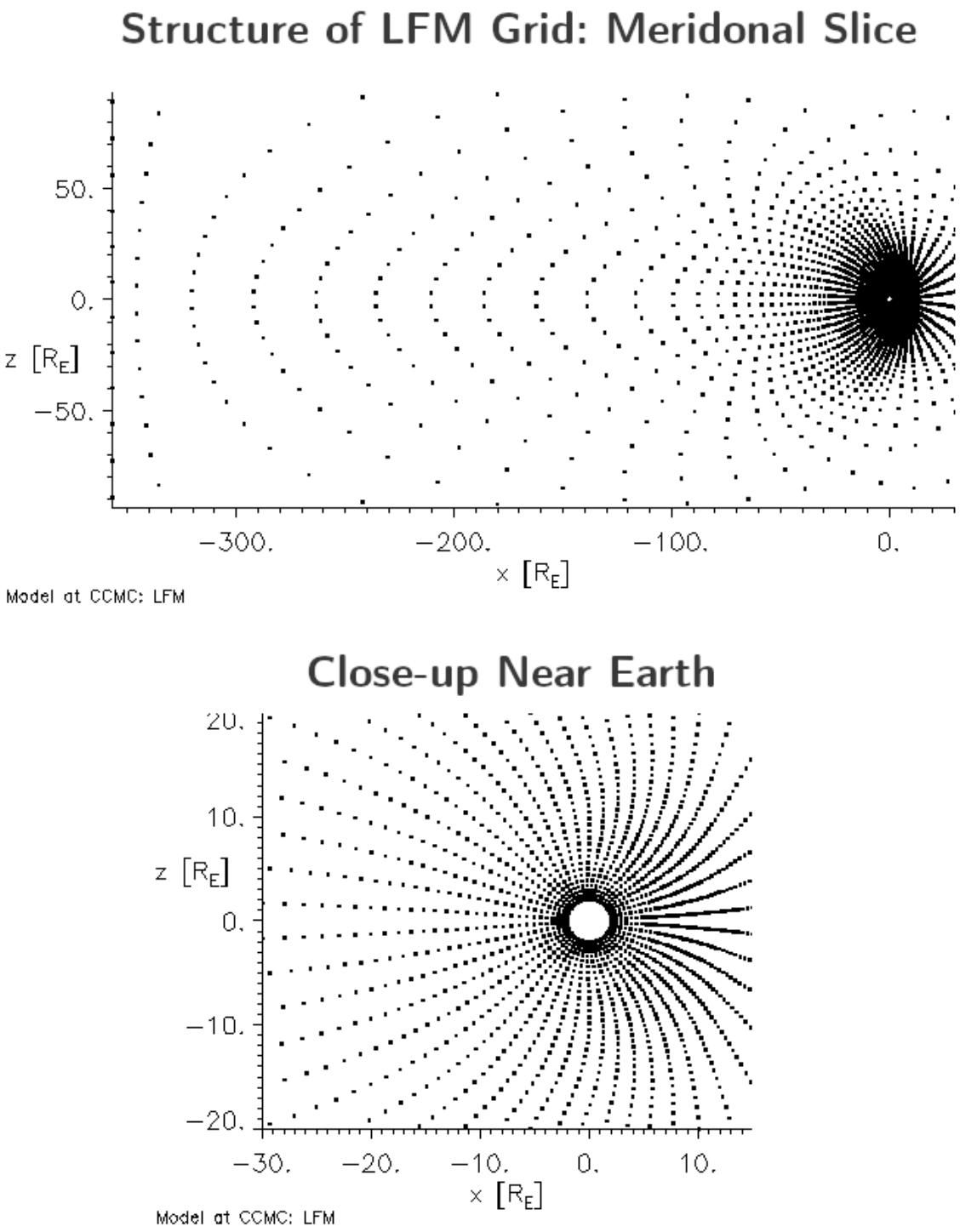

Figure 1.8: Structure of the LFM Grid to illustrate spatial distribution of cell density. Not all points are shown to increase visual clarity. Image courtesy of the CCMC at NASA/GSFC.

comparison of this rectangular grid and the LFM grid, see Appendix D.

1.8 Review of Literature on Outer Radiation Acceleration

This work focuses more on the question of outer radiation belt acceleration than on loss mechanisms. Key results in the literature are reviewed here to appropriately follow up on the current state of the art.

We will first review the work of Green et al., 2004 [46]. At the time of this paper's writing, the community had identified two competing candidate methods: internal methods (energization by cyclotron-scale wave/particle interactions in the inner magnetosphere) and external methods (energization by movement of particles through radial diffusion).

Green sought to make progress on the question by applying an adiabatic invariant analysis to in-situ plasma observations from the POLAR spacecraft. The study frames the problem as differentiating between two structures in the time-dependent phase space density profile as a function of L^* at fixed M (labeled in their work as μ) and K. It can be argued from underlying physics that internal methods would produce the pattern seen in the top right of Figure 1.8; similarly, external methods would produce the pattern seen on the bottom. In Green's paper, data analysis is performed to determine which pattern best matches the data. Green also provides an excellent discussion of how errors in the magnetic field model could skew the results.

The conclusion of Green et al., 2004 indicates that the data best matches the internal method, specifically with a peak in f around $L \approx 5$. Though not without limitations, this result strongly suggests that wave/particle interactions occurring in the inner magnetosphere are responsible for electron energization to relativistic levels.

The work of Reeves et al., 2013 [99] was an early report from the Van Allen Probes era. This paper presents a similar analysis to Green et al., 2004, but focuses on a single storm, and uses Van Allen Probes data instead of POLAR data. It finds a similar result to Green et al., 2004, in that the pattern of local acceleration is observed in the phase space density signatures, albeit with some signatures of radial diffusion. The main addition of this work was that it was done with better

instrumentation (including resolution and resistance to penetrating radiation) and with a better orbit (very low inclination). Because Green et al., 2004's conclusion was able to be reproduced with stronger scientific instrumentation and radiation belt specific mission design, it was made stronger.

We next look at the work of Thorne et al., 2014 [120], which convincingly demonstrated through simulation that chorus wave emissions play the largest role in electron acceleration. It uses a global model of chorus emissions and an electron population and was validated with Van Allen Probes measurements where the two overlapped. Within the overlapping region between the model and the Van Allen Probes, the agreement was strong, which is used to argue that the model does well outside the overlapping region. This paper was significant because it narrows the multiple candidates Green et al., 2004 identified to internal mechanisms. From this paper, we have better confidence that internal methods are predominantly chorus wave driven.

The most recent paper we review here is the work of Boyd et al., 2018 [22], which presents a statistical survey of phase space density signatures using dual coverage from the Van Allen Probes and THEMIS. In the paper's data analysis, data from the Van Allen Probes are used for lower L measurements of outer radiation belts, and THEMIS data are used for higher L. This is the most prominent study that has looked at the phenomena from a statistical perspective. The team studied 80 events and found that 87% of those events showed signatures of internal method acceleration. They found other classes of phase space density they call "flat gradients" and "positive gradients," which are the exceptions to following the internal mechanism pattern. They note that the signature of internal method acceleration is not always obvious unless you include high L coverage from a mission like THEMIS. These contributions are important because they reveal the "sometimes-but-not-always" nature of outer radiation belt electron acceleration and expose the limitations of using just the Van Allen Probes to study the outer radiation belts for this problem.

Chapter 2

Algorithms for Computing Adiabatic Invariants

The text in this chapter is based on the publication "Numerical Calculations of Adiabatic Invariants from MHD-Driven Magnetic Fields" by da Silva et al., published in the Journal of Geophysical Research: Space Physics, 2024.

2.1 Introduction

The canonical adiabatic invariants of a trapped particle are (M, J, Φ), derived from the Hamilton-Jacobi action integrals associated with the three periodic motions which trapped particles undergo [48, 103]. The advantage of the adiabatic invariant coordinates is their nature as an essential state variable independent of the changing global magnetic field. During a geomagnetic storm, the shape of the Earth's magnetic field will change in response to storm-time influences. In turn, the exact velocity $\mathbf{v}$ of trapped particles will change in response to the changed magnetic field. However, the adiabatic invariant coordinate (M, J, Φ) will remain constant provided (a) no work is done on the particle and (b) the global magnetospheric fields change sufficiently slowly. The adiabatic invariants are themselves a representation of the particle's velocity, being a function of both the (v_x, v_y, v_z) velocity representation and the instantaneous magnetic field throughout the drift shell.

Currently, in the radiation belt research community, the conversion of a spacecraft measured $f(\mathbf{x}, \mathbf{v})$ to $f(M, K, L^*)$ is done with empirical magnetic field models. Common codes include LANL-Star [146], IRBEM (`https://prbem.github.io/IRBEM/`), SPENVIS (`https://www.spenvis.oma.`

be/), LANLGeoMag (https://github.com/drsteve/LANLGeoMag) [51], and direct particle tracing methods. Out of all these tools, only LANLGeoMag supports MHD model output by letting the user provide the global magnetic field in an unstructured array as points. Reasons most tools have not been adapted to MHD magnetic field models include the immediate availability of empirical models and the difficulties associated with calculating using MHD magnetic field models. Such difficulties include (a) the more involved task of looking up $\mathbf{B(x)}$ due to non-uniform adapted grids, (b) the computational cost associated with running MHD simulations, and (c) the storage cost associated with preserving large MHD simulation output. Still, this is a missed opportunity, as the modeling capabilities of MHD simulation offer, at the very least, complementary insight into empirical models for most studies using adiabatic invariants. This point will be expanded further in Section 2.3.

This work documents a rigorous treatment of the calculation of adiabatic invariants with MHD fields, presented as a stepping stone for exploratory modeling work in radiation belt dynamics using MHD simulation. As a mode of study to compliment (not replace) analysis using empirical fields, scientific inquiry using MHD simulation allows one to powerfully (a) access the otherwise-unavailable global state such as the density, flow velocity, pressure, and electric field and (b) experiment with impact of particular physics. In the past, access to the self-consistent global state from MHD simulations has allowed the community to answer questions on the now widely accepted importance of ULF waves on radial diffusion [41] and drift-resonant electron interactions [38, 37, 102]. In addition, the work of Olsen et al., 2000 [90] discussed the possibility of generating the peaks in phase space density profiles driven solely by Ultra Low Frequency (ULF) waves, and [75] explored the calculation of radial diffusion coefficients using MHD modeling.

Broadly, MHD simulations offer the ability to inspect and evaluate wave propagation in the mHz frequency range, which is not included in empirical magnetic field models. Similarly, MHD simulation provides access to the global self-consistent physical variables mentioned, which are unavailable in empirical models like Tsyganenko. While empirical models of these variables exist, they generally do not contain wave propagation and are not self-consistent with the empirical

magnetic field model. However, such variables are crucial to describing the complete magnetospheric system. Furthermore, it is common for MHD simulation codes to have "optional" features, such as the inclusion of the Hall term [55], which can lead to qualitatively different results in the global magnetosphere [16]. Other optional features include coupling the simulation with other models that cover aspects of the magnetospheric system known to be inaccurate with MHD alone (such as the ring current) [50, 121].

In Section 2.2, we outline the numerical techniques developed to accomplish the adiabatic invariant calculation and the tuning of key algorithmic parameters. Section 2.3 analyzes a storm to note the differences between the MHD-driven LFM/LFM-RCM and the empirical Tsyganenko T96 and TS05 models. In this section, a time series of L^* is also presented and compared between the LFM and LFM-RCM models. In Section 2.7, we summarize the work performed.

Related to this chapter are two appendices. In the Appendix A, we provide supporting data of the OMNI IMF Parameters during the 2 October 2013 Storm, and in Appendix B, we display an example of a non-closed drift shell with features that complicate the calculation of L^*.

2.2 Algorithms and Methods

Charged particles trapped in the radiation belts undergo three fundamental periodic motions. These period motions are gyration perpendicular to a magnetic field line, magnetic mirroring along a magnetic field line (bounce motion, sometimes called magnetic bottling), and azimuthal drift about the Earth. The first periodic motion, gyration, is the outcome of the continuous influence of the Lorentz force as it alters the direction of $v_\perp$, causing the particle to track a helix path. The second periodic motion, magnetic mirroring, is the outcome of the exchange of velocity between $v_\parallel$ and $v_\perp$ as the particle moves to increasing field strengths while conserving its kinetic energy and first invariant. For particles with a pitch angle outside a critical loss-cone threshold [61, 135], the particle will encounter a sufficiently strong field that will transfer any remaining parallel velocity into perpendicular velocity before reversing the particle in the direction from which it came. The third periodic motion, azimuthal drift, is caused by a combination of ∇B drift due to gradients

in the magnetic field strength along the bounce path and curvature drift due to the curvature of field lines along the bounce path [42, 26]. Both of these influences act in a different direction based on the charge, and as a result, protons and electrons azimuthally drift in opposite directions. The surface covered by the particle as it bounces northward/southward along field lines and its azimuthal drift about the Earth is called the particle drift shell. When combined, these three structured and periodic motions (gyration, bouncing, and drifting) account for the trajectory of trapped particles when no outside work is being done.

The adiabatic invariants in this paper are calculated using numerical methods as a function of global magnetic field output from the LFM model and empirical models and initial particle velocity/position state.

Each adiabatic invariant corresponds to an integration over a path/surface associated with the respective periodic motion in the action integral. For the first invariant M, this periodic motion is the path of a single gyration; for the second invariant K, this is the bounce path; and for the third invariant L^* this is the drift shell. In the case of most geomagnetically trapped charged particles, the gyro radius is sufficiently small compared to the scale of structure in the magnetic field such that we can consider B constant over the entire gyration, and thus, no integration is required. We note that there are some scenarios where this is not the case, such as with electron motion under very strongly curved field lines relative to the gyroradius [8]. Therefore, the calculation of the first invariant is trivial but is discussed here for completeness.

The first adiabatic invariant, M, is calculated directly with the equation given in Roederer & Zhang 2016 [100] and Murphy 2017 [83]. In this equation, p is the momentum, m_0 is the rest mass, $\bar{B}$ is the magnetic field strength averaged over a gyration [26], $p_\perp$ is the perpendicular momentum, and α is the particle's pitch angle.

$$M = \frac{p_\perp^2}{2m_0\bar{B}} = \frac{p^2\sin^2(\alpha)}{2m_0\bar{B}} \tag{2.1}$$

The second adiabatic invariant is calculated using the bounce path. The bounce path is

determined as a portion of the field line trace done in both directions from the point in question. Given a starting point, the bounce path extends northward and southward, necessarily between the first occurrence of the magnetic mirroring strength B_m in each direction.

In this work, the field line trace is done by using the Runge-Kutta 4-5 method [40]. In mathematical terms, the trace of the magnetic field line is computed by solving

$$\mathbf{x}(0) = \mathbf{x}_0, \quad \dot{\mathbf{x}} = \frac{d\mathbf{x}(t)}{dt} = a\hat{\mathbf{B}} \tag{2.2}$$

where $\mathbf{x}(t)$ is the position of the field line trace at position t, $\mathbf{x}_0$ is the starting point of the trace, $\hat{\mathbf{B}}$ is the local direction of the magnetic field, and a is a constant to convert from units of magnetic field intensity to units of space over time [67]. We note that we typically start the field line trace at the magnetic equator, in practice, using Runge-Kutta 4-5 twice: once forward (for $t > 0$) to go northward and once backward (for $t < 0$) to go southward. The trace is terminated when the inner (outer) boundary is reached, indicating a closed (open) field line.

The most common scenario for a field line in the inner magnetosphere is that the field strength is the strongest at the Earth's surface, declines monotonically towards a minimum value, and then increases again as the field line comes back towards the Earth. In this case, the selection of any point along the same field line will produce the same bounce path. This is not the case for certain dayside field lines and associated values of B_m associated with drift shell splitting [108, 80]. For these types of field lines, the field line intensity versus magnetic latitude will have two "wells" or local minima, which will encapsulate the bounce path for sufficiently small B_m, whereas sufficiently large B_m will not be affected by this structure. Therefore, particles with sufficiently low B_m mirroring on such a field line may be trapped on a different bounce path depending on their starting location or bounce phase when entering the Shabansky region.

Because of this phenomenon, the bounce path is determined as a function of two parameters: the starting point and B_m. Specifically, the path is determined by iterating southwards and northwards along the field line trace until B_m is encountered. The starting point is not important if B at the starting point is less than B_m. When B_m is low enough for the particle to become trapped

in one of the two bottom wells, a Shabansky orbit will occur.

Once the bounce path is determined, the next step is to integrate along the bounce path using the equation also derived in Equation 1.3 [100]. In this equation, $\mathbf{B}(s)$ is the magnetic field strength at the position along the trace, B_m is the magnetic mirroring strength, and ds is the differential length along the trace path. Numerically, in this work this equation is integrated using trapezoidal integration with $ds \to \Delta s$ estimated as spatial distance between steps in the field line trace. The S.I. units of K obtained through this method are $\mathrm{km} \cdot \sqrt{\mathrm{nT}}$.

The final third adiabatic invariant, L^*, corresponds to the total magnetic flux outside the particle's drift shell. To calculate L^*, we first evaluate the drift shell for the particle. As the particle moves along its bounce path, it also undergoes an azimuthal drift based on its charge due to curvature of the field line and radial gradients in the field strength. The surface spanned by the particle's bounce motion and azimuthal drift is known as the drift shell. This surface necessarily never extends to either magnetic pole. It visually appears as a belt or ring around the earth. For a summary of the forces which contribute to the azimuthal drift, the reader is referred to [88].

The classic way of calculating the drift shell is through a full particle trace. This involves solving a differential equation for the particle's position and momentum throughout its drift orbit and field line trace, for all points along its trajectory. However, this is computationally very expensive and most notably can be simplified using known physics. When it is known that the particle is trapped, the particle will necessarily move spatially inwards or outwards during the azimuthal drift to conserve its second invariant K corresponding to the fixed B_m [100]. This key simplification allows us to determine the drift shell by iterating through magnetic local times (MLT's), and selecting the field line to find one which conserves K from the fixed B_m. This selection of the field line is significantly less computationally expensive than a full particle trace, though it leaves the question as to how many MLT's and how many field line searches to match K from B_m are required to accurately describe the drift shell.

Drift shell splitting is an important feature to capture in these calculations of the drift shell. The foundational work of [104] established that drift shell splitting arises from either of two local

time asymmetries in the magnetosphere: (a) local time asymmetries in the magnetic field, and to a lesser extent (b) from the presence of an electric field, such as the dawn-to-dusk electric field [141]. The Roederer method used in this work addresses the drift shell splitting from (a) but not (b), due to the electric field being a lesser source of drift shell splitting and the effects complicating the key simplifications that make the algorithm computationally efficient.

We present two methods for calculating the drift shell of a particle, the first which does so from fixed and equally spaced magnetic local times (MLT's) around Earth, and the second does so using automatically spaced MLT's. The automatically spaced MLT mode is backed by a Runge-Kutta algorithm which varies the spacing to meet user-specified absolute and relative error tolerances.

The overall equation used to calculate L^* in this work is,

$$L^* = \left(\frac{R_{inner}}{R_E}\right) \frac{2\pi}{\int_0^{2\pi} \sin^2(\theta_{inner}(\phi))d\phi}, \tag{2.3}$$

where R_{inner} is the inner boundary of the model, θ_{inner} is the northern most colatitude of the field line trace at the model inner boundary, and ϕ is the MLT as an angle between 0 and 2π. This is a modified [100] Equation 3.40, with a scaling of $Rinner/R_E$. This scaling is derived by extending the field line at the inner boundary of the model to 1 R_E using the dipole model, and in particular the equation $r = L\sin^2(\theta)$. When this equation is applied at the footpoint at both the model inner boundary location and at the magnetically connected surface footpoint, we can derive the equation,

$$\sin^2(\theta_{surface}) = \frac{R_E}{R_{inner}}\sin^2(\theta_{inner}), \tag{2.4}$$

where $\theta_{surface}$ is the northern most colatitude of the field line at the surface of Earth. Through this method, we evaluate L^* at 1 R_E, while simultaneously accommodating magnetic field models with inner boundaries above 1 R_E.

In the fixed and equally spaced mode, the drift shell field line is specified at N_{MLT} unique and equally spaced MLT's around Earth. We denote the MLTs as ϕ_i for $i = 1, 2, ..., N_{MLT}$. First, a field line trace and accompanying $K(\phi_1, d_1)$ is found for the starting point at distance d from the magnetic equator.

Next, a field line search is done at each MLT to place the drift shell field line there. The search varies the candidate field line by way of the equatorial distance d, and continues to vary it until a field line is found which produces the desired $K(\phi_i, d_i) \approx K(\phi_1, d_1)$ using the same B_m. We note that in the case of equatorial mirroring particles, a shortcut exists, wherein one can instead search for d in $B_{min}(\phi_i, d) \approx B_{min}(\phi_1, d_1)$, a computationally simpler task because no field line trace is required, as this inherently satisfies the second invariant K when $K = 0$. This shortcut essentially amounts to finding an isoline of B_{min} around Earth.

To perform the search, candidate distances are tested using a linear search approach. A large step size is first used (called the initial step, equal to 0.05 R_E) to bracket the target, and then a smaller step size is used to refine the estimate (called the refined step, equal to 0.01 R_E). The stepping approach was used over bisection (as recommended in [83]) because complex magnetospheres were found where the curve $K(\phi, d)$ vs. d possessed multiple matching K. When this occurred, the correct one (as determined by drift physics) is that which is closest to the previous drift shell field line. However, bisection would be unable to guarantee which matching solution would be obtained. For this reason, the algorithm was designed to gradually approach the target with carefully chosen step sizes. The sizes of both the major and refined steps were chosen to be smaller than the distances observed between multiple matching K in these complex magnetospheres.

When the iteration of refined steps identifies an interval of the refined step size holding d, the final interval is interpolated. A more controlled use of bisection was experimented with to replace this interpolation, where it would be used just over this final interval. The advantage would be that it could guarantee arbitrary error control between the target and acquired K values. However, we found that this approach resulted in code which was 2.5 times slower (with relative error set to 10^{-5}), and the impact on the final L^* was less than 0.1%. For this reason, it was deemed that the interpolation approach was sufficient.

In the automatically spaced MLT mode, the method for searching field lines at each MLT is similar. The key difference is that the MLTs selected are found while continuously solving the integral in Equation 2.8. Specifically, the integral is solved using Explicit Runge-Kutta method of

order 4-5 (RK45) [35], as implemented in the SciPy package [140], which selects MLTs along the integral bounds. Specifically, it solves the integral $D(\phi_{up}) = \int_0^{\phi_{up}} \sin^2(\theta_{inner}(\phi))d\phi$ through the differential equation $\frac{dD}{d\phi} = \sin^2(\theta_{inner}(\phi))$ and $D(0) = 0$, particularly seeking $D(2\pi)$ to arrive at the integral in Equation 2.8. The method is configured with user-specified relative and absolute error tolerances, which are used to automatically select where $\frac{dD}{d\phi}$ is evaluated based on its rate of change.

We note that the method algorithm is also parameterized by initial and maximum MLT spacings. These were selected through an experiment performed using the fixed equally-spaced MLT mode of the code. In this experiment, we looked at both simple (quiet-time) and complex (disturbed) magnetospheres with different magnetic field models, and varied the number of local times. We visually inspected these plots to look for where the calculation became stable. Calculation stability is determined by using a sufficiently high local time resolution (number of local time points) to sufficiently capture all necessary drift shell information. The results of this experiment can be found in Figure 2.1. We concluded that in the best case, the calculation becomes stable around four MLTs (the left column), and at the worst, around 16 (most of the right column). Therefore, we set the maximum spacing to $2\pi/4$ and the initial spacing to $2\pi/16$.

We note that while the automatically spaced MLT mode provides desirable automated error control, it is usually 2-3 times slower than simply using the fixed equally spaced MLT mode with a safe spacing of $2\pi/16$. Therefore, we recommend that the fixed equally spaced MLT mode be used for "quicklook" initial data analysis, and the automatically spaced MLT mode be used for refined publication-quality results.

In Figure 2.2 we observe the automatically spaced MLT mode selecting a different number of MLTs throughout the course of a storm. The number of local times selected varies throughout the storm by a factor of two. The drift shells which required the highest number of MLTs to model occurred during the main phase of the storm. A second increase in drift shell complexity occurred later into the recovery phase, around where a secondary yet small drop in D_{st} occurred.

The automatically spaced MLT mode results in the completed integral; the fixed equally

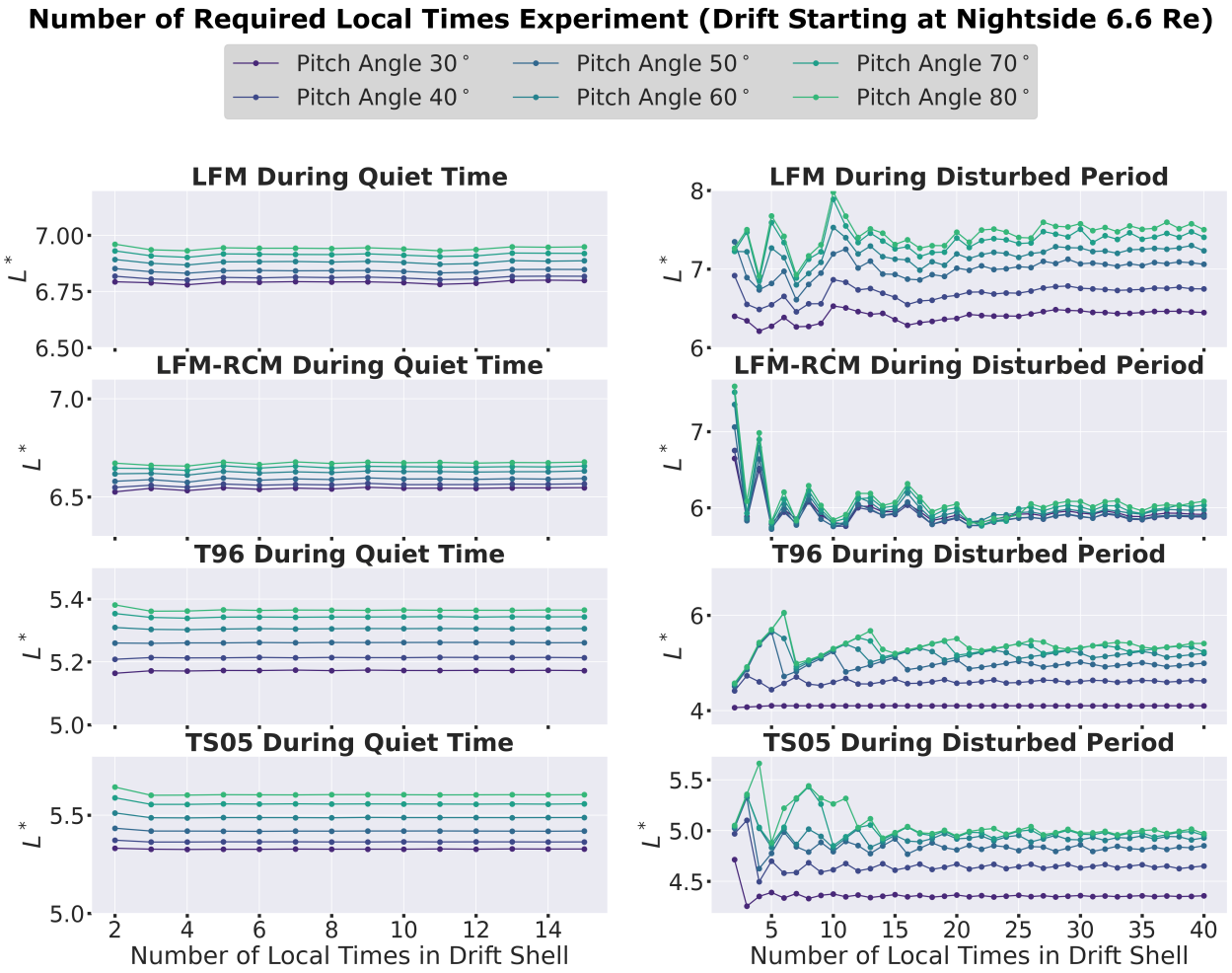

Figure 2.1: An experiment to investigate the minimum number of local times required in the drift shell to calculate L^* for simple (quiet time) and complex (disturbed period) magnetospheres. In this experiment, we increased the number of local times and visually inspected where the calculation became stable to determine at what point the number of local times is sufficient to model the drift shell.

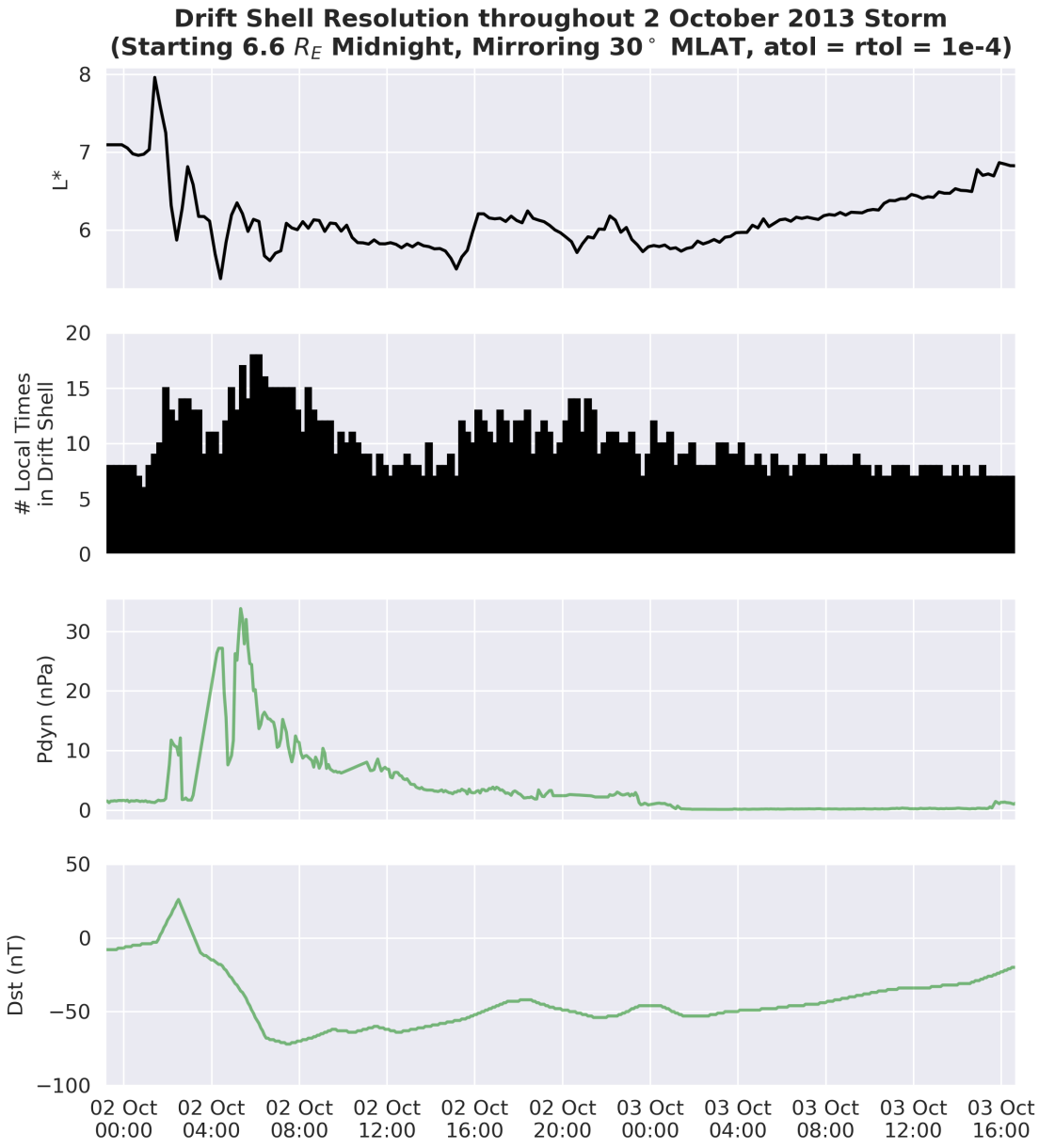

Figure 2.2: Changes in the automatically selected number of MLT's throughout the course of a geogmagnetic storm, when the automatically spaced MLT mode is used. In this plot, the absolute tolerance (atol) and relative tolerance (rtol) of the RK45 method was set to 10^{-4}.

spaced MLT mode still requires numerical integration. This is done through trapezoidal integration after smoothing the integrand to counter any numerical noise from the drift shell calculation in $\theta_{inner}(\phi)$. The smoothing is performed with a cubic spline constrained with a periodic condition forcing the derivative of the integrand and the integrand itself equal at the boundary.

We review that the integral evaluated is the modified integral given in [100]. Experiments were performed where the magnetic flux through the polar cap Φ was numerically integrated through

$$\Phi = \iint \mathbf{B} \cdot \hat{\mathbf{n}} \, dA, \tag{2.5}$$

with $\mathbf{B}$ provided by IGRF [90]. However, it was found that this approach changed L^* less than 1.5% throughout the outer radiation belt ($L^* > 3$), while being more computationally expensive, and therefore was not used. More information on this can be found in Section 2.5.

2.3 Dependence of Invariants on Magnetic Field Model

In this section, we study the dependence of invariant calculation on magnetic field models using data from the 2 October 2013 geomagnetic storm. This is done to motivate future work which will investigate the effects of magnetic field model used to organize spacecraft-collected phase space density data. The models studied in this section are (a) the two MHD models LFM and LFM-RCM and the empirical models (b) T96 and TS05, all driven by solar wind conditions provided by 5-minute OMNI and the 5-minute QinDenton dataset for TS05 W parameters. T96 and TS05 are evaluated on the LFM grid to avoid any question of grid effects on the results. In this section, we examine the adiabatic invariants calculated in each model, and discuss how features such as increased tail stretching, differing current structures, and off-equator dayside field line minima contribute to different invariant profiles.

Simulations of the 2 October 2013 geomagnetic storm were selected to provide a practical application for study. Through observation, the 2 October 2013 geomagnetic storm was classified as a G2 Moderate storm on the NOAA Space Weather Prediction Center (SWPC) scale, originating from a coronal mass ejection with an observed nominal solar wind speed of 600 km/s and

observed strongly southward B_z with an observed nominal intensity of -19 nT. The LFM and LFM-RCM simulations were driven by L1 satellite observations of solar wind conditions from the WIND spacecraft [45].

The structure of the inner magnetospheric fields holds key properties for understanding the orbit of geomagnetically trapped particles. The structure of the inner magnetospheric fields is determined from the currents in the magnetosphere and the Earth's geomagnetic dynamo. The Earth's dynamo largely corresponds to the internal field, while the currents in the magnetosphere correspond to the external field. To characterize the external field, the intensity of the current contribution originating from the external field is calculated using Ampere's law.

$$\mathbf{J}_{ext} = \frac{1}{\mu_0} \nabla \times (\mathbf{B}_{model} - \mathbf{B}_{dipole}) \tag{2.6}$$

Visualization of this quantity across a meridional slice shows much finer level of current detail in the LFM/LFM-RCM than T96/TS05 as show in Figure 2.3. T96/TS05 leave absent many field-aligned currents around the poles and into the tail, and greatly simplify the cusp currents. Finally, all models show different interpretations of night-side plasmasphere currents, with this current largely absent in stand-alone LFM. These multiple models also show the footpoint of the cusp current at roughly the same location.

Field line traces are added to show differences in tail stretching and dayside compression. The traces start at magnetic latitudes in the inner boundary corresponding to the footpoints of field lines associated with L-Shells of $L = 1, 2, 3, \ldots$ of a dipole model. We see a drastically higher level of stretching in the T96/TS05 models, and similar levels of stretching between LFM and LFM-RCM.

Magnetic field models can be compared in reference to geosynchronous magnetometer data orbiting at 6.6 R_E in Figure 2.4. In this figure, data from the GOES-13 magnetometer is plotted alongside the magnetic field obtained from each model, taken at the ephemeris location of GOES-

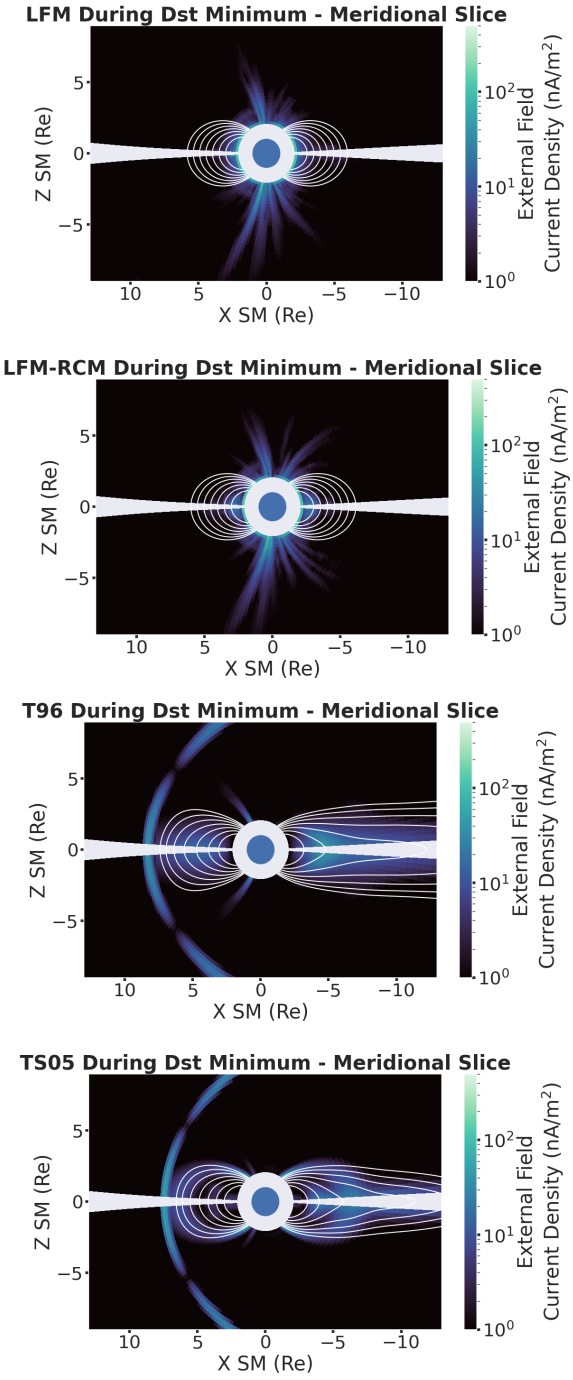

Figure 2.3: External field current density contribution from different magnetic field models in the inner magnetosphere, during D_{st} minimum of the 2 October 2013 storm. This quantity is calculated using Ampere's law in Equation 2.3. Field line traces are overlaid starting at magnetic latitudes on the inner boundary corresponding to the footpoint of field lines associated with L-Shells of $L = 1, 2, 3, ...$ in a dipole model. In this plot, we note the finer detail of current structures in LFM and LFM-RCM, increased tail stretching in T96 and TS05, and the differences in night-side plasmasphere currents between all models.

13. In the case of LFM/LFM-RCM, the magnetic field is linearly interpolated within a grid cell. In the case of T96/TS05, the model is evaluated directly at the GOES-13 satellite ephemeris.

This comparison illustrates agreement in B_x and B_y, but less so in the B_z. The disagreement in B_z is particularly emphasized during the main phase and early recovery period of the storm. During the extended recovery period, the shape of B_z is broadly retained throughout the recovery and during brief fluctuation (10/03, 18:00). We note that in LFM and LFM-RCM, B_z is offset from the observation even though the fluctuations match. This offset in B_z has been discussed in the literature and is understood to be related to tail stretching and LFM's tendency to produce weaker-than-reality currents in the plasma sheet [144]. A zoomed version of this plot is included in Appendix A, which highlights the differences in B_z during the main phase of the storm up to and slightly after the storm's minimum D_{st}.

The differences in B_z between approximately 2 October at 4:00 and 16:00 are now discussed in the context of Equations 1.3 and 2.8. When calculating K in this context, the parameters dependent on the magnetic field model are the mirror points s_1 and s_2, and the magnetic field strength along the bounce path, B(s). In our comparison, we see that $|B|$ differs between models by as much as 50%. Smaller $|B|$'s along the bounce path would make the bounce path longer (required to go to higher MLATs to reach B_m), and $B(s)$ smaller along the bounce path. These errors would propagate to errors in K, which would then propagate into an error in the drift shell and in turn L^*.

What is not immediately obvious from this figure are the differences during the main phase of the storm. A zoomed portion of that plot during the main phase of the storm (up until and slightly after D_{st} minimum) is presented here, with particular focus on the B_z panel.

In this plot, we notice that the shape of B_z observed by GOES-13 is much better captured by the MHD models (LFM and LFM-RCM) than by the empirical models (T96 and TS05). Up until around 2 October at 04:30, all models show a gradual decrease in B_z, though the arc is more closely captured by the MHD models. However, only the MHD models capture the increase in B_z following this period. In the final hour of this plot, GOES-13 observations show B_z reducing again,

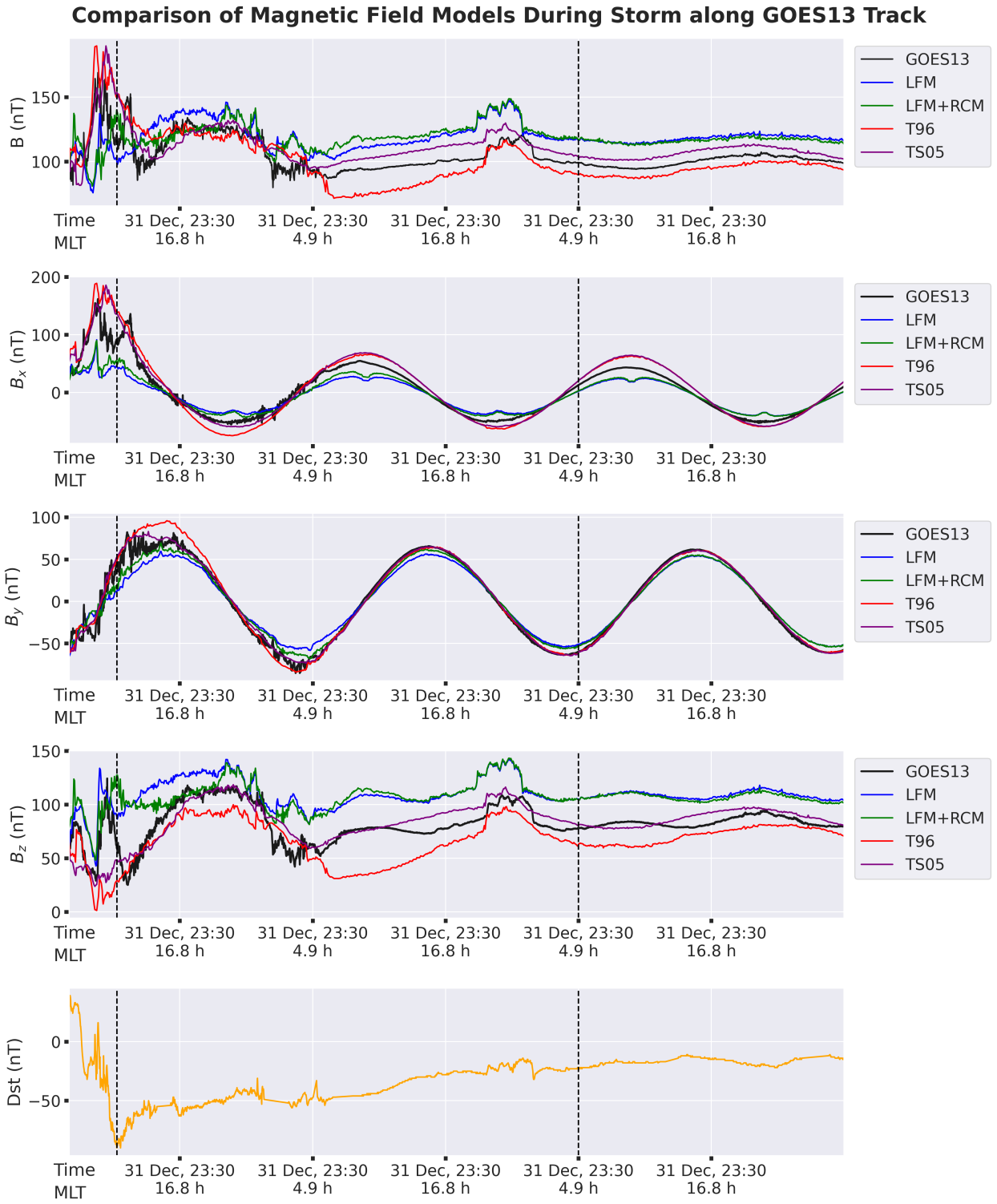

Figure 2.4: Magnetic field models compared to geosynchronous GOES-13 magnetometer data at 6.6 R_E. The magnetic field components are plotted in GSM coordinates. This comparison illustrates good agreement with observation in the B_x and B_y components for all models, and then much disagreement in the B_z particularly during the main phase and early recovery period of the storm. The two vertical bars identify the minimum D_{st} (left vertical bar), and the quiet time periods referenced in Figure 2.1 and Figure 2.6.

which is not captured well by any of the four models.

To illustrate this further, a profile of K is compared between models in Figure 2.6. In this visualization, the color at a particular location corresponds to the K associated with a particle mirroring on that magnetic field line at that magnetic latitude. The solid black lines are field line traces are each L-shell, and the dashed black lines are isolines of constant K. This plot was constructed with a 2D grid with linear spaced distances and mirroring magnetic latitudes. For each grid point, K was calculated for particles mirroring at the given magnetic latitude, starting at the point $(d, 0, 0)$ for distance d in the SM coordinate system.

A prominent feature of this plot is the abrupt upward trend for the $K = 0$ lines on the dayside. This is due to the moving location of the minimum field intensity further out into the dayside. The change in the minimum field intensity is understood to be due to the influence of the solar wind, the dipole tilt, Shabansky orbits and off-equatorial minima.

The K profile holds implications for the study of equatorially mirroring test particle simulations. An assumption of equatorially mirroring test particle simulations is that $K = 0$ at B_{min}, which also coincides with the magnetic equitorial plane in the simulation. This property is shown here to generally hold within $\approx 10\ R_E$, on both the dayside and nightside, but generally not farther out. This observation is reassuring for the ability for test particle simulations to model the outer radiation belt largely contained within this range. We notice that the shape of this $K = 0$ line is slightly different between each model, with T96 particularly having an out-of-trend shape.

In Konstantinidis et al., 2015 [66] magnetic field models were compared through the analysis of L^* vs increasing distances into the tail. The authors of this work report differences in adiabatic invariants between various empirical model tools, with variations in L^* as much as 5% at 6 R_E and 30% at 8 R_E. The tools examined by those authors included LANL* [146], IRBEM (`https://prbem.github.io/IRBEM/`), SPENVIS (`https://www.spenvis.oma.be/`), and a particle tracer. An analogous comparison is presented here using the models studied in this paper during a quiet magnetosphere, shown in Figure 2.7. In each plot, one can see separation between the MHD (LFM and LFM-RCM) and the empirical models (TS05 and T96). This is understood to be because the

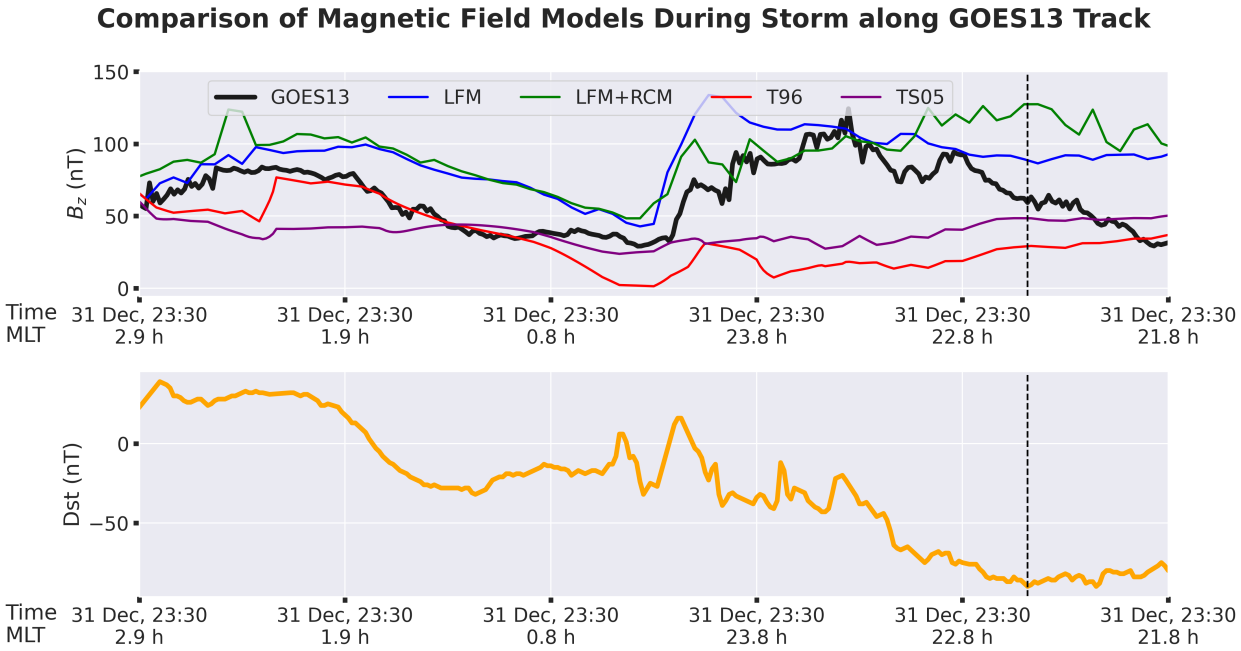

Figure 2.5: Zoomed Portion of 2 October 2013 Storm during the main phase of the storm (up until and slightly after D_{st} minimum). In this plot, we notice that the shape of B_z observed by GOES-13 is much better captured by the MHD models (LFM and LFM-RCM) than by the empirical models (T96 and TS05). Up until around 10/02 04:30, all models show a gradual decrease in B_z, though the arc is more closely captured by the MHD models. However, only the MHD models capture the increase in B_z following this period. In the final hour of this plot, GOES-13 observations show B_Z reducing again, which is captured well by no model.

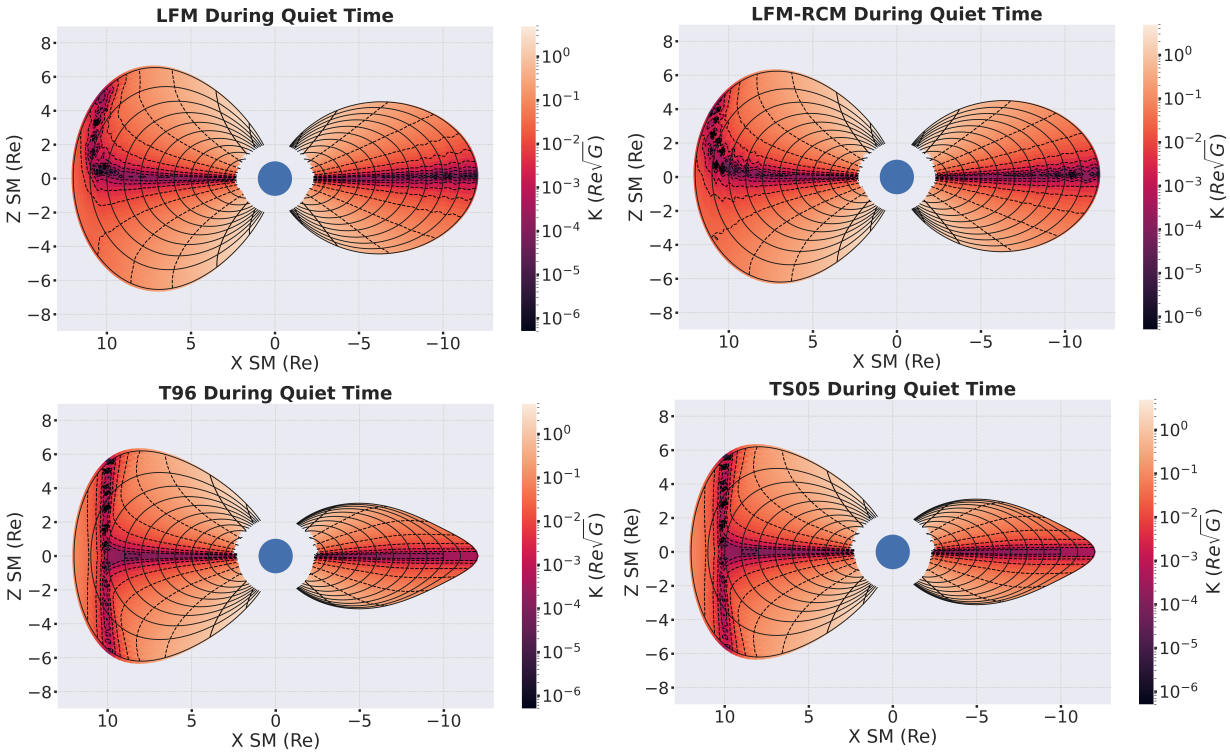

Figure 2.6: Profile of K (quiet times on left, disturbed times on right). In this visualization, the color at a particle location corresponds to the K associated with a particle mirroring on that magnetic field line at that magnetic latitude. The color of the plot is the value of K for a particle mirroring on that magnetic field line at that magnetic latitude. The dashed lines are isolines of constant K. The solid black lines are field line traces for each L-shell. A prominent feature of this plot is the abrupt upward trend for the $K = 0$ line on the dayside, which is slightly different shape for each model. This is due to the moving location of the minimum field intensity further out into the dayside.

MHD models contain less stretching than the empirical models, therefore yielding different K.

Finally, in Figure 2.8 we see L^* calculated at increasing distances into the tail and two mirroring magnetic latitudes (15° and 30°). The OMNI IMF parameters during this storm are provided in Appendix A. The most variation in L^* over the course of the storm occurs at larger distances into the tail, where the influence of the external field over the dipole is the greatest. It is noted that during the main phase of the storm, the drift shells associated with $d = -8\ R_E$ are largely not closed and do not allow the algorithm to converge. An example of a magnetosphere which contains such not closed drift shells can be found in Appendix B.

There are interesting differences between LFM and LFM-RCM during the beginning of the recovery phase on 2 October at 12:00 when the large magnetospheric field disturbances have completed but ring current enhancement continues. The decline in L^* for the $d = -8\ R_E$ lines is similar, but shows a much different shape around 2 October at 18:00. This is likely due to the more detailed ring current modeling that RCM provides that acts as a feedback, providing pressure modification to the MHD solution by LFM. The fluctuation in L^* around 3 October at 18:00 corresponds with a denser burst of solar wind traveling at the same velocity as the solar wind preceding and following. Both magnetic field models produce comparable L^*'s that reflect the magnetosphere's response to this small/brief solar wind density fluctuation.

2.4 Explanation of Systematically Larger values for L^* from MHD Models

In this section we address the observation that predictions of L^* are systematically larger when MHD models used over the empirical models used (TS05 and T96). As previously noted, the difference becomes larger further out in the magnetosphere. Later in this dissertation when we study the SWMF-RCM MHD model, it will become evident that L^* is systematically larger for that as well.

The calculation of L^* requires calculation of the drift shell. In Figure 2.9, we show the bounce paths in two drifts drift shells: LFM-RCM (an MHD model) and TS05 (an empirical model). In this experiment, the results were computed at increasing radii into the tail for a particle with an

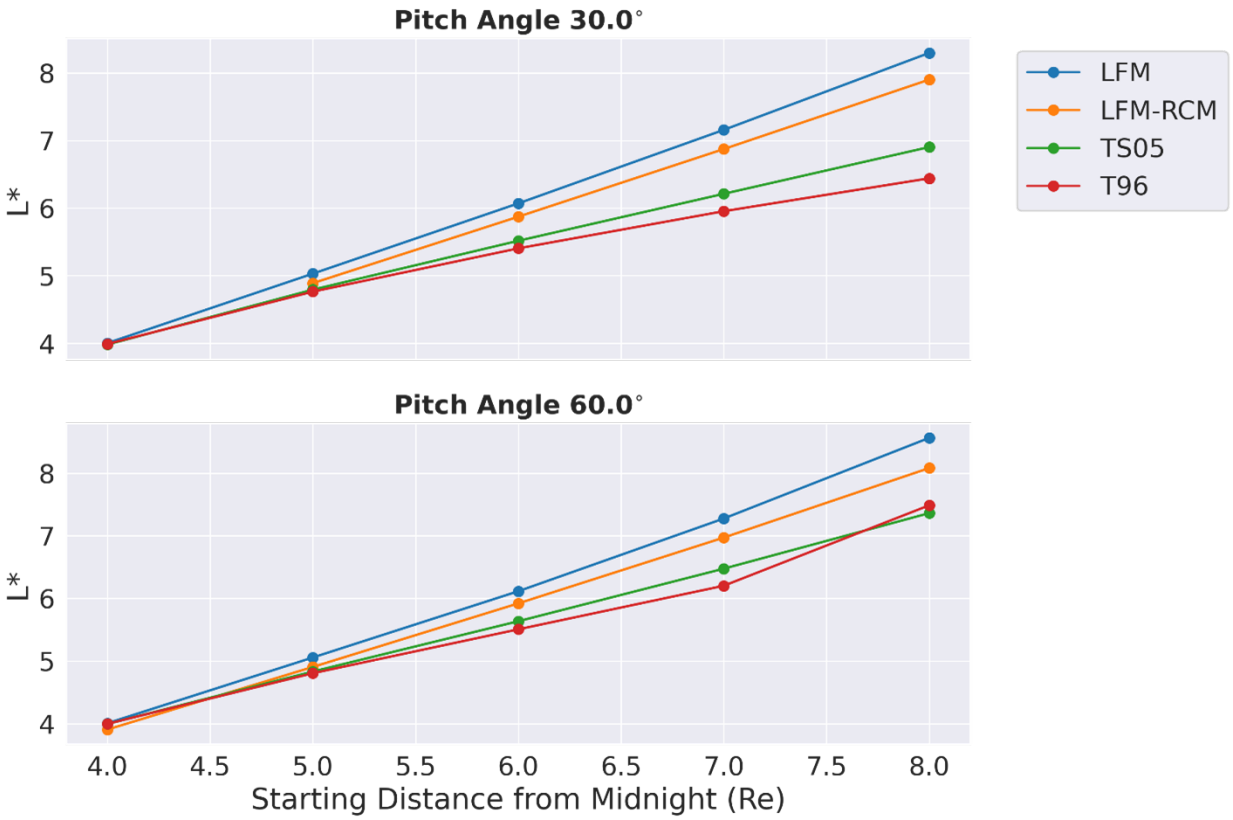

Figure 2.7: Calculation of L^* at increasing distances into the tail between magnetic field models during quiet-time conditions. We note that LFM and LFM-RCM contain less stretching than the T96 and TS05 models, and therefore starting the same point in the represent notable different values of K. This plot reflects a similar visualization as found in [66] where LANLstar, IRBEM, SPENVIS, and a particle tracer were compared.

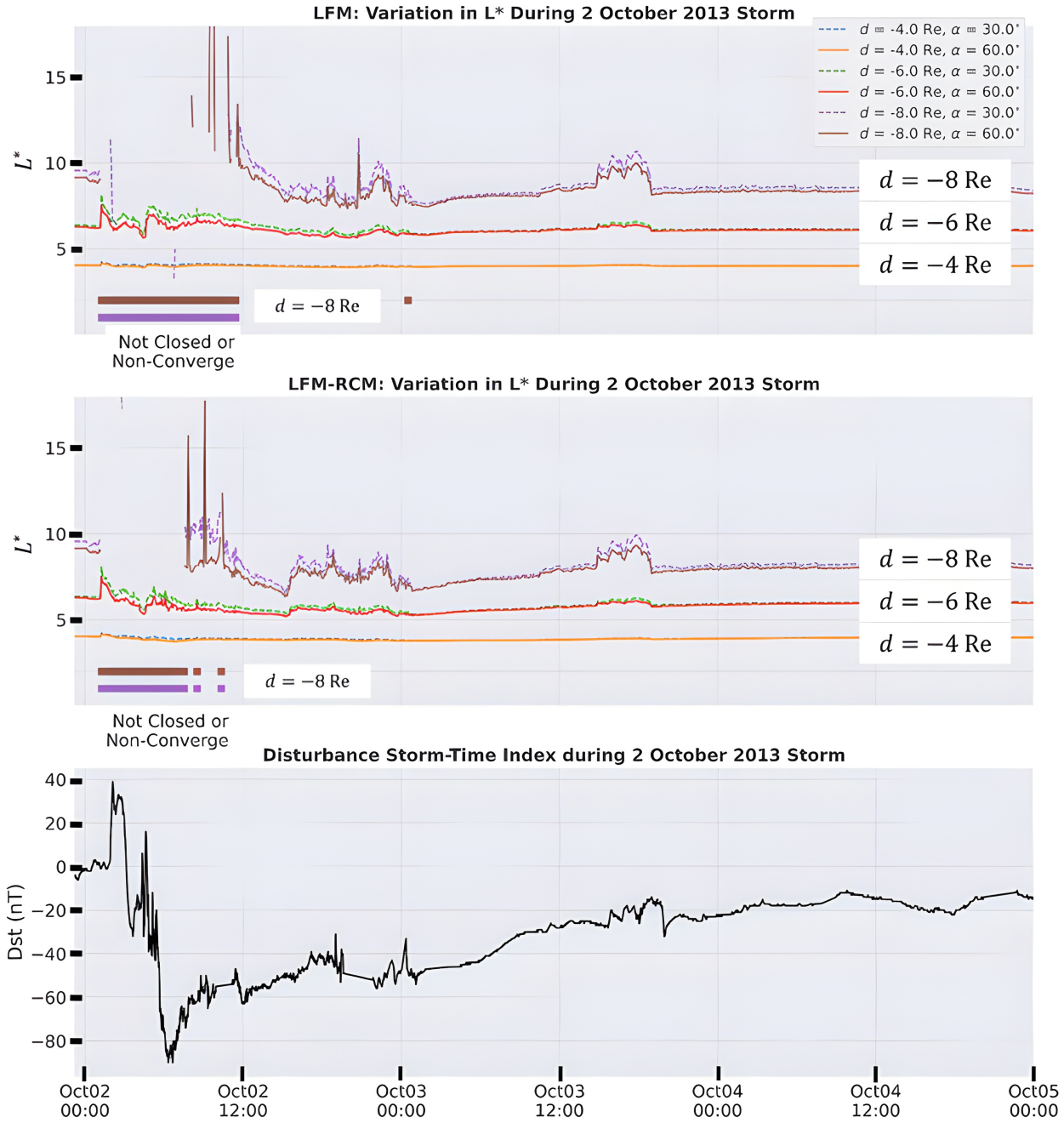

Figure 2.8: Values of $L*$ calculated at various distances into the tail during the 2 October 2013 Storm. We note that during the main phase of the storm many of the drift shells are not closed and resulted in L^* calculations that did not converge. Furthermore, the biggest deviations of L^* from the dipole L^* occur farther into the magnetosphere where the external field holds greater influence over the dipole field.

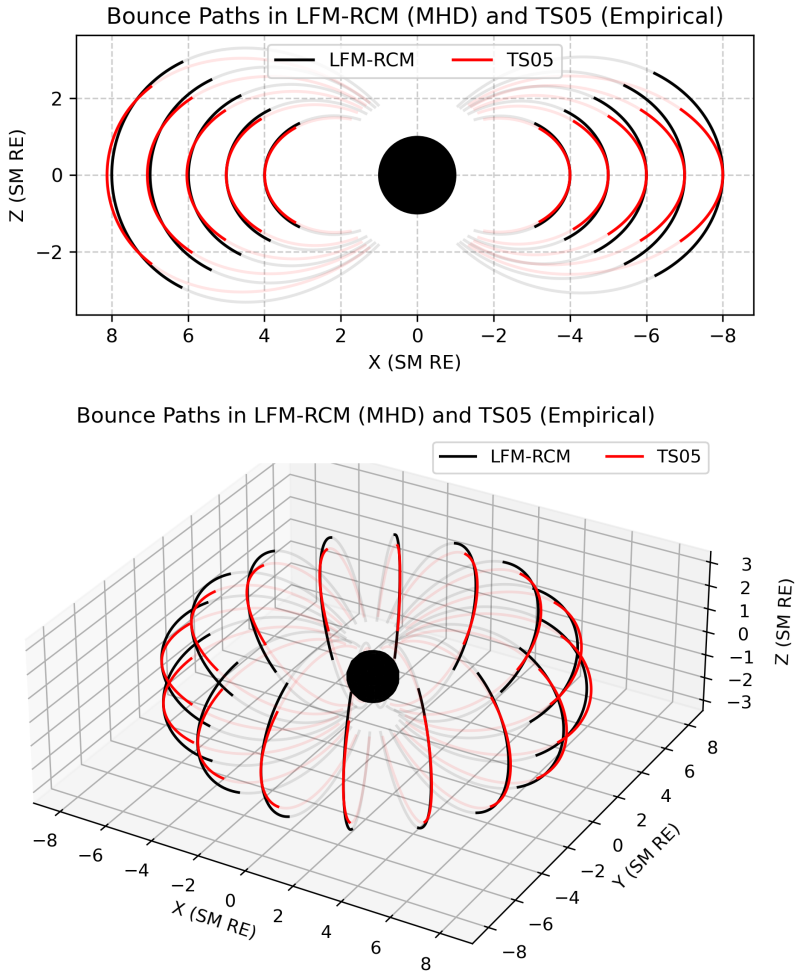

Figure 2.9: Bounce paths between an MHD model and an empirical model, showing differences in dayside compression and tail stretching. This leads to a different shapes in the polar cap surface Π, which by association changes Φ and L^*. Modeling is done for a particle with equatorial pitch angle $\alpha = 45°$.

equatorial pitch angle of $\alpha = 45°$. In this plot, the bounce path are plotted in bold colors, with the remainder of the field lines in faded colors.

By definition, $L^* \propto 1/\Phi$ where the variable Φ is the magnetic flux through the drift shell [100]. The variable Φ is given by

$$\Phi = \int_{\Pi} \mathbf{B} \cdot d\mathbf{S}, \tag{2.7}$$

where Π is the polar cap through the drift shell and $\mathbf{B}$ is the magnetic field. With the empirical

model, we observe increased stretching in the tail and compression that on the dayside that alter Π. At each radii considered, the field line of the bounce path with the empirical model stays closer to the equator, and in turns grows the size of the Π surface.

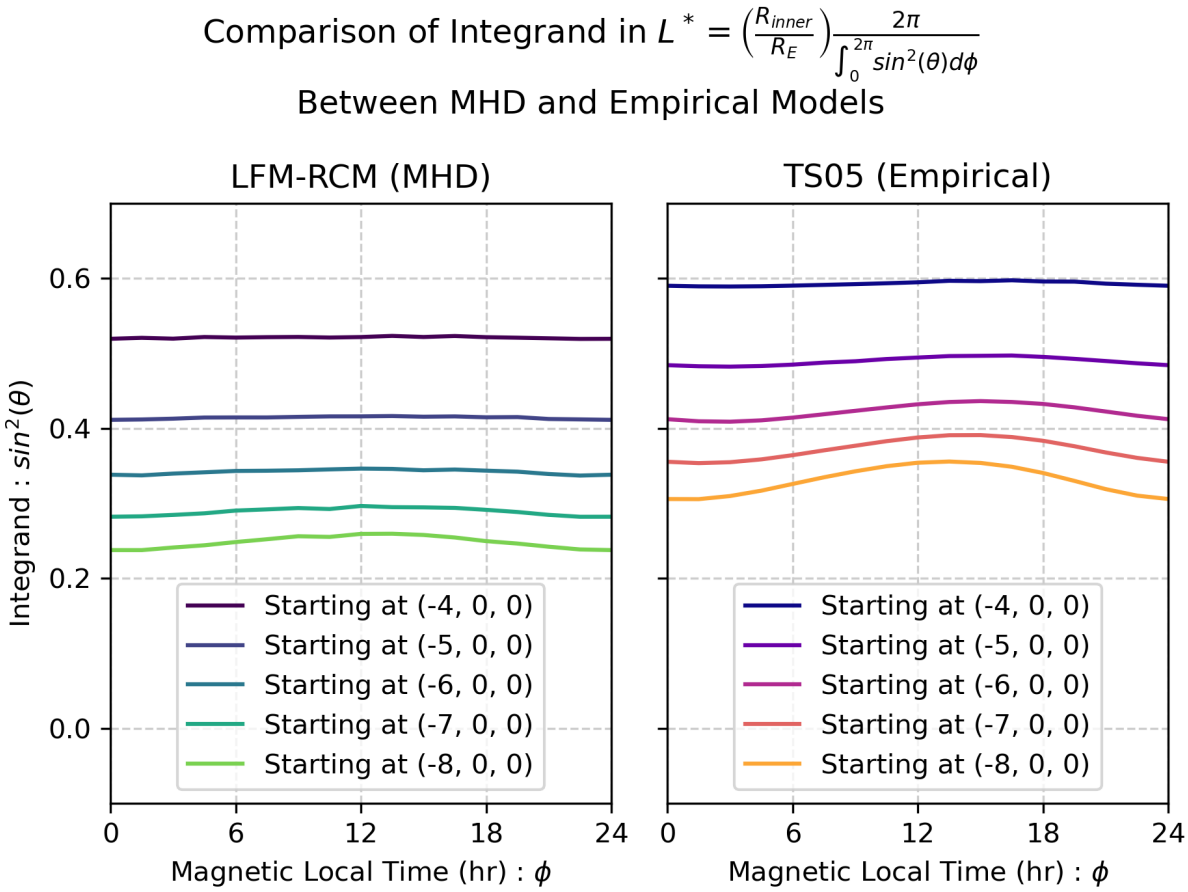

Figure 2.10: Inspection of the integral embedded in the equation we use for L^* ([31]). This plot inspects the integral between an MHD and empirical model. Calculations are done for a particle with equatorial pitch angle $\alpha = 45°$.

The equation we use for L^* is

$$L^* = \left(\frac{R_{inner}}{R_E}\right) \frac{2\pi}{\int_0^{2\pi} \sin^2(\theta) d\phi} \tag{2.8}$$

where R_{inner} is the inner boundary of the model, R_E is the radius of the earth, ϕ is the magnetic local time in radians, and θ is the northern most magnetic colatitude of the field line at each magnetic local time. The integral $\int_0^{2\pi} \sin^2(\theta) d\phi$ contains the same information found in Φ, albeit

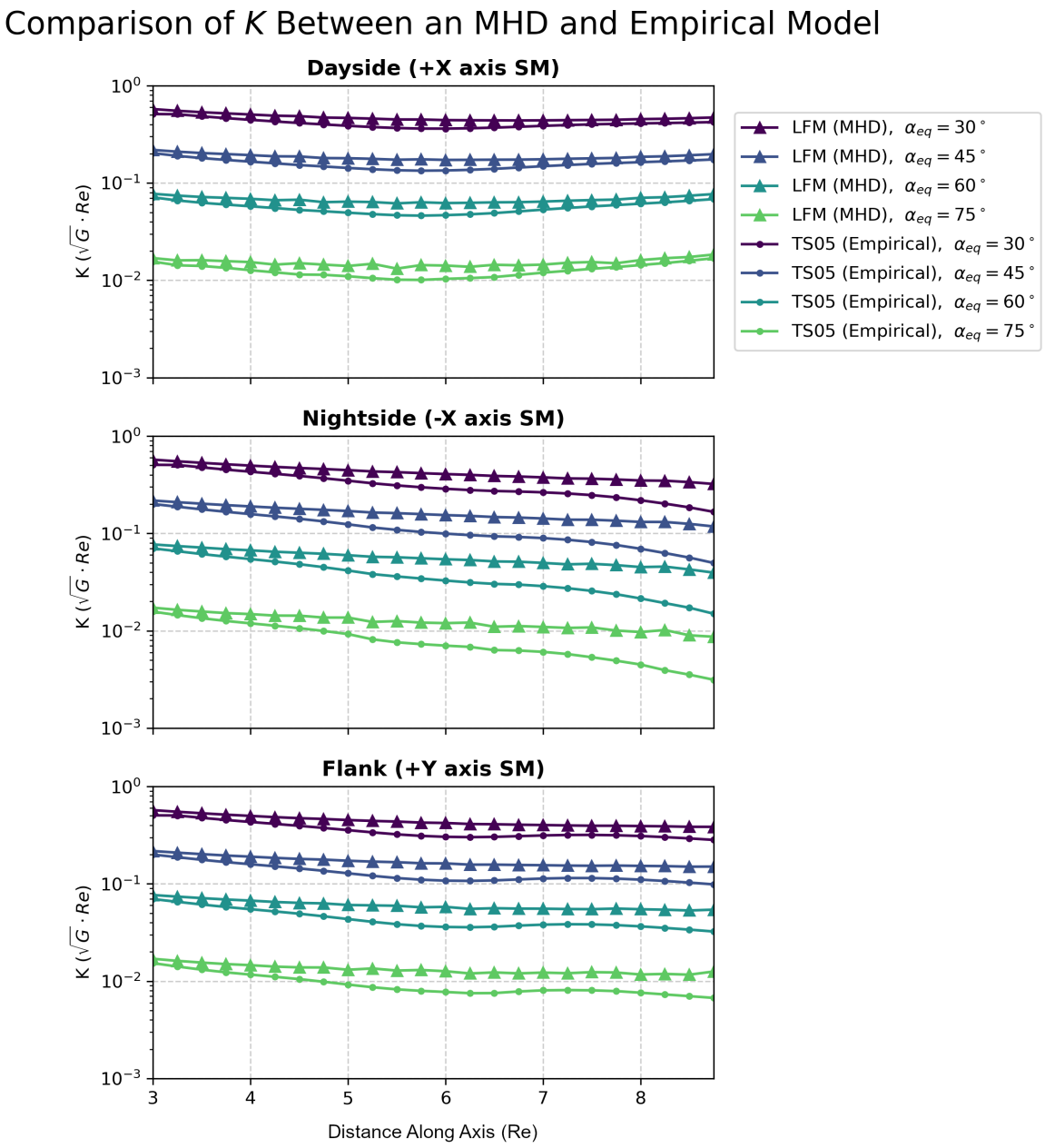

Figure 2.11: Comparison of K values between an MHD model and an empirical model (LFM is LFM-RCM).

with different units. Specifically, the dependence on the shape of Π in Φ is encoded in $\theta = \theta(\phi)$, and the dependence on $\mathbf{B}$ is removed after substituting the dipole equations.

The differences in the integral $\int_0^{2\pi} \sin^2(\theta) d\phi$ are described in Figure 2.10. For this experiment

we used the same drift shell calculations as in Figure 2.9. We observe that the empirical models generate lower values of $\sin^2(\theta)$ in general (which implies lower values of θ), and in general have a stronger day/night dependence.

With these observations we can have confirmed that the polar cap Π in the MHD models is smaller with the MHD models, especially on the day and night sides. From the equations, this leads to decreased Φ and in turn larger L^*.

Both empirical and MHD models capture the magnetopause (Chapman-Ferraro) current which flows *eastward* along the magnetopause and corresponds to compression and increased $|B|$ inside the magnetosphere on the dayside. They also both capture the ring current (to a greater extent when MHD is coupled with RCM as assumed for the MHD models here) which flows *westward* causing a decrease in $|B|$ in the region typically occupied by outer zone electrons [63]. The degree to which each current system is accurately captured in the statistical ensemble between Tysganenko and MHD models determines the relative difference between the two in mapping L^*.

Our finding that the MHD models yield a larger value of L^* is consistent with a stronger ring current in the MHD-RCM case than found in the empirical models. This has been found to be the case when examining solar energetic proton cutoffs in both types of models for a geomagnetic storm 7 – 8 September 2017 of comparable magnitude [74] to the three studied here (check). However, these cutoffs are dominated by fields at low L values (3 – 6). At higher L (andL^*) values, magnetopause currents play an increasingly important role. [73] have shown in an $L - L^*$ comparison for two different geomagnetic storms that IMF B_z, which controls the location of the magnetopause [114] and strength of the magnetopause current [130] an outward displacement of L^* relative to dipole L (r in the equatorial plane) when $B_z > 0$ and inward displacement when $B_z < 0$.

2.5 Evaluation of Alternatives: IGRF and 2D Polar Cap Integration

In this section, we evaluate alternatives to the methods presented in this manuscript. Previous works such as [106] have suggested that IGRF may be important to the calculation of L^*, and other works such as [1] suggest that L* be calculated through a 2D integration over the polar cap using

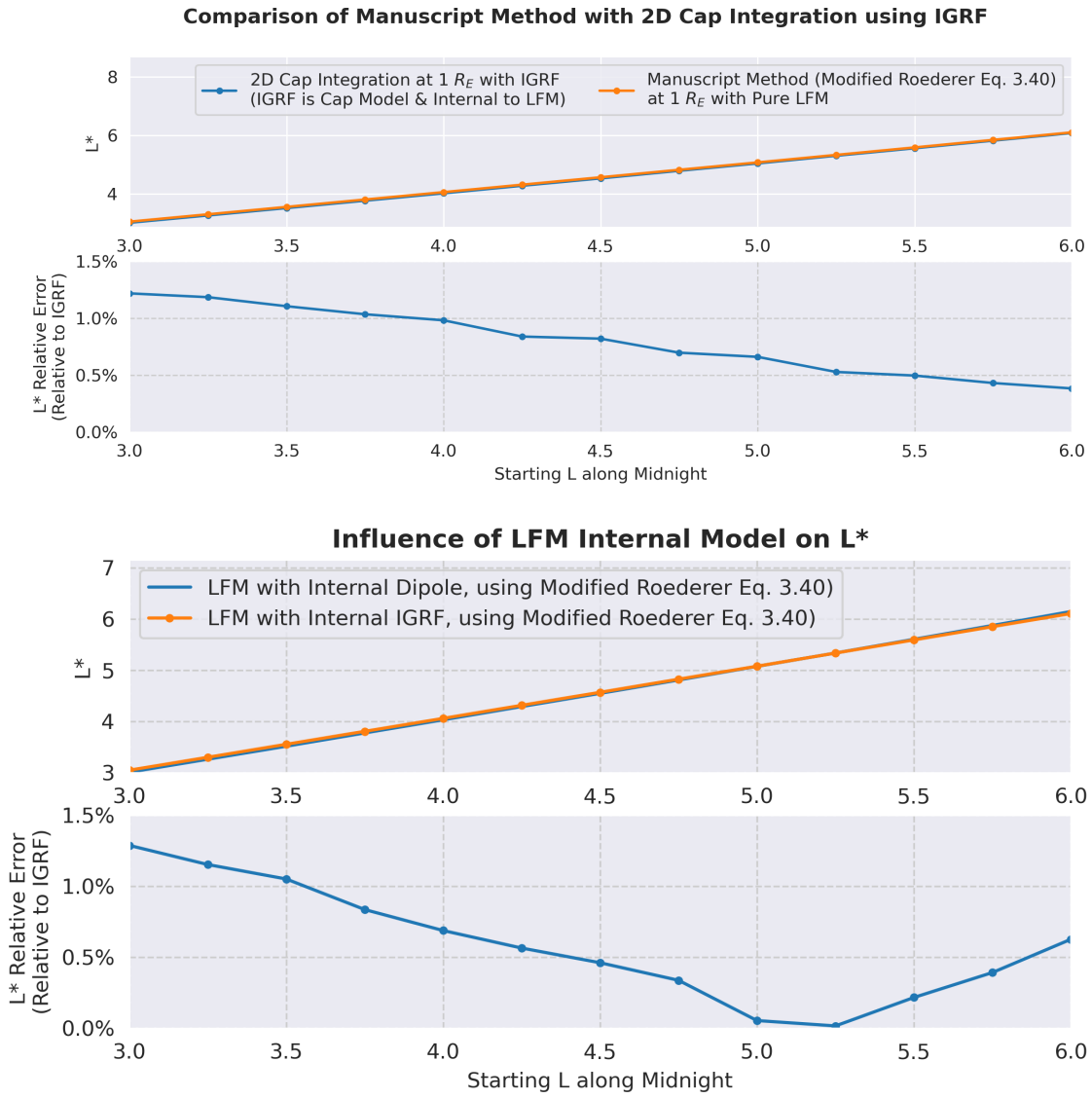

Figure 2.12: Top panel: Demonstration that using the 2D Polar Cap integration method with the LFM internal model changed to IGRF as a post-processing step has a negligible impact on L^* ($< 1.5\%$) for $3 \leq L \leq 6$ compared to using the method presented in this manuscript. Bottom panel: Demonstration without using the 2D polar cap integration, that the effect of changing the LFM internal model to IGRF as a post-processing step has a negligible impact on L^* ($< 1.5\%$) for $3 \leq L \leq 6$ compared to using LFM with an internal dipole (the official method of this manuscript).

the equation $L^* = 2\pi k_0/(\Phi R_E)$, where k_0 is Earth's dipole moment, and $\Phi = \iint \mathbf{B} \cdot \hat{\mathbf{n}}\, dA$ as in Equation 2.5. This is in contrast to the Modified Roederer Equation 3.40 presented in Equation 2.8, whose derivation starts with the 2D integral form of Φ, applies the dipole model to provide $\mathbf{B}$ [100], and is modified against using the dipole model to extend each footpoint from the model inner boundary to Earth's surface (a contribution of this work).

IGRF is an empirical model of Earth's internal magnetic field designed to capture deviations from the dipole and drifts in the magnetic structure over time. We investigate using IGRF in two ways. First, we evaluate IGRF serving as an internal model for LFM, wherein the for each point on the model grid the dipole field is subtracted and the IGRF field is added to replace it as a post-processing step. We note that this results in more realistic non-dipiolar near-Earth fields for the L^* calculation, but also removes the consistency of the fields with the MHD model physics used to produce them (which assume an internal dipole). Second, we evaluate using IGRF to trace each drift shell footpoint at the model inner boundary down to Earth's surface, at which point the 2D integration over the polar cap would be performed.

An experiment is performed to evaluate the effect of doing both these alternatives at the same time. The results are displayed in the top panel of Figure 2.12. To perform the 2D polar cap integration at 1 R_E, we numerically integrated,

$$\Phi = \int_{\phi=0}^{\phi=2\pi} \int_{\theta=\theta_{surface}(\phi)}^{\theta=\pi/2} B_r \sin(\theta) R_E^2 d\theta d\phi, \tag{2.9}$$

where B_r is the radial magnetic field component, and $\theta_{surface}$ is the colatitude of the point which results from tracing the drift shell footpoint at the model inner boundary down to Earth's surface using IGRF. In this experiment, it is found for $3 \leq L \leq 6$ the difference in L^* between these two methods is within 1.5%. This was deemed a very small change which did not outweigh the cost associated with integrating IGRF into the final software and causing our results to now depend on the details of another model.

We further seek to understand whether spatial variations in the IGRF field strength are impactful to the calculation. To further check this, an experiment is performed where the 2D

integration method is applied to produce L^* corresponding to artificial circular polar caps spanning varying magnetic latitudes. The calculation is repeated with **B** provided by the standard dipole model and then again with IGRF. It was found that for polar caps extending between 30° and 60° MLAT, the difference between L^* calculated each way is less than 1.5%.

Furthermore, a calculation of the dipole strength of IGRF using the 2010 coefficients and Equation 6 of [2] produced a value of $B_0^{IGRF} = 29,950.126$ nT, which is within 0.2% of LFM's nominal $B_0^{LFM} = 30,000$ nT. However, we note that the IGRF dipole strength drifts year-by-year, and has drifted on the order of 5% between the years of 1900 to 2000.

A final experiment was performed to check the effect of replacing the LFM internal model with IGRF as a post-processing step, while holding the L^* equation unchanged. That was done to separate the effects of the 2D polar cap integration method from using IGRF as the internal model. The results are displayed in the bottom panel of Figure 2.12. It was found that when this the internal model was changed this way, the difference in L^* was again less than 1.5%. For the same reasons as before, this difference was deemed too small to be worth the cost.

2.6 Review of Alternative Approaches for Computing L^*

We have detailed the methodology which will be used in this dissertation for computing L^*, which will be applied in the subsequent chapters. This method is known as the "Roederer method", in tribute to Roederer's 1970 book (revised 2014 and 2016) [100]. For the stake of completeness, we will now mention alternative methods in the literature for computing L^*.

In the work of Albert et al., 2018 [1], a newly developed code named AFRL-Shell is presented which directly follows guiding center motion to trace the particle trajectory. Multiple variations of the guiding center equations exist, and AFRL-Shell uses the ubiquitous Brizard-Chan 1999 formulation [23] with neglected electric field effects. Albert et al., state they ignore electric field effects because a self-consistent electric field is not available with the Tsyganenko models they used. In AFRL-Shell, once the trace of the particle trajectory is found, the value of L^* is found by mapping the northern mirror points down to 0.8 R_E and computing the line integral around the

interior polar cap, similar to what was described previously in this dissertation.

In Appendix C of Selesnick et al., 2000 [106] another method was presented for computing the third invariant in the form of Φ. The technique sets the problem up as coupled differential equations, which are then solved numerically using standard techniques. These equations are:

$$\Phi = \oint \mathbf{A} \cdot d\mathbf{l}, \tag{2.10}$$

$$\frac{d\Phi}{dl} = R\left(A_\theta \frac{d\theta}{dl} + A_\lambda \sin\theta \frac{d\lambda}{dl}\right), \tag{2.11}$$

$$\frac{d\theta}{dl} = \frac{-dI/d\lambda}{R((dI/d\lambda)^2 + \sin^2\theta(dl/d\theta)^2)^{1/2}}, \tag{2.12}$$

$$\frac{d\lambda}{dl} = \frac{-dI/d\theta}{R((dI/d\lambda)^2 + \sin^2\theta(dl/d\theta)^2)^{1/2}}, \tag{2.13}$$

$$\frac{dI}{ds} = \left(1 - \frac{B}{B_m}\right)^{1/2}, \tag{2.14}$$

$$\frac{dx}{ds} = \frac{B_x}{B}, \tag{2.15}$$

$$\frac{dy}{ds} = \frac{B_y}{B}, \tag{2.16}$$

and (2.17)

$$\frac{dz}{ds} = \frac{B_z}{B}, \tag{2.18}$$

where $\mathbf{A}$ is the vector magnetic potential, l is the path around the polar cap, θ and λ are the spherical coordinate angles of a point on the polar cap, and I is the second invariant. Similar to the Reoderer method, this approach exploits the connection between the second and third invariants. The couple differential equations are solved using a Runge-Kutta method with adaptive step sizes [96].

Another approach is that of Min et al. 2013, [82], who derive a method of computing L^* using (U, B, K) coordinates [143]. Min's method requires an expensive preparation step of computing two-dimensional isoenergy contours that simplify the subsequent calculations. The preparation step needs only be done once per magnetic field timestep and can be reused for different L^* criteria. The method is perhaps unique from the Roederer and Selesnick methods in that it allows for constant electric potential along field lines.

While not necessarily a technique of calculating L^* as much as an implementation of regression to speed up results calculated using another tool, the LANL* software provides very efficient calculation of L^* using a pre-trained neural network [146]. The neural network itself is trained on millions of L^* calculations made using the IRBEM code (based on the Roederer method). The IRBEM code is parameterized by different backing models, and strictly speaking, there is a different LANL* method for each of these models. Models used to train LANL* include T96, T01 Quiet, T03 Storm, TS05, OP dynamic, and OP quiet. The inputs that the neural network learns to map to L^* vary based on the backing model, but generally reflect the similar inputs to those for the backing model. This approach, which essentially uses the neural network as a more capable agent for statistical regression, boasts the ability to generate L^* estimates in microseconds instead of the usual seconds. The work analyzes the error rigorously, which is found low enough for the approach to be applicable to most practical use cases.

2.7 Summary

In this chapter we present a rigorously developed methodology for calculating adiabatic invariants in MHD-driven fields, starting with those from LFM and LFM-RCM. Our methodology follows the groundwork laid out in Roederer and Zhang 2016 [100] (first edition published in 1970) and further refined in Murphy 2017 [83]. The rigorous development and documentation of this algorithm is a contribution to the research community as groundwork preceding later utilization.

In addition to the methodology, this chapter presented evidence to justify the effort spent developing tools for calculating adiabatic invariants around fields that originate from MHD-driven simulation. A detailed analysis of meridional current derived from LFM, LFM-RCM, T96, and TS05 was presented and showed differences that warrant consideration. In particular, we showed a much higher level of detail in current complexity in the MHD-driven models compared to the empirical models.

Calculation of L^* over the course of the 2 October 2013 storm for LFM and LFM-RCM showed that differences in L^* exist primarily at larger L^* in the magnetosphere where the external

field's influence over the dipole grows. The time series of the L^* calculation between LFM and LFM-RCM showed the influence of the ring current modeling as a feedback mechanism that affects L^*.

These tools are developed with the intent to enhance the capability of modeling studies using L^*, as well as extending the ability to accurately organize in-situ data using adiabatic invariants. In this chapter, we noted the difference in L^* structure based on whether LFM was coupled with the RCM model. A rich history of magnetospheric simulation has explored different variants of the MHD equations (such as Hall and Multi-Fluid), as well as complex many-model coupling [15, 95]. By establishing methodology and code to analyze the dynamics of trapped particles under simulated magnetospheres, we begin a period of science where the impacts of modeling choices on trapped charged particle dynamics can be studied.

Chapter 3

Quantifying Adiabatic Motion

The text in this chapter is based on the publication "Quantifying Adiabatic Motion in the Outer Radiation Belt and Ring Current with Invariant Matching" by da Silva et al., published in Frontiers in Astronomy and Space Sciences, 2024 [30].

3.1 Introduction

Adiabatic motion is fundamental motion in the radiation belts, of critical importance to the overarching theory of the dynamics that touches a wide range of scenarios. The ability to quantify the adiabatic processes that occur in the radiation belts is a powerful tool to have, with numerous applications. We will outline several applications here, surveying from both ends of the spectrum: from practical space weather operations to more academic research questions about the magnetosphere.

Geostationary satellites, which orbit in circular orbits with an apogee of 6.6 R_E, are critical assets embedded in the outer radiation belt region. In the later sections of this chapter, we will show that within a single storm, particles may move adiabatically inwards or outwards at scales up to 2 R_E. To better protect geostationary assets, we may ask: how much of the energetic particle population overlaps with geostationary orbit? We can reason that energetic particle populations interior to the geosynchronous radius of 6.6 R_E, which do not initially reach these satellites, may adiabatically move radially outwards until they intersect with geostationary orbit and pose a threat. Similarly, energetic particle populations currently posing a threat to geosynchronous and

other satellites may move inward and create a safety period. To best understand the time-varying energetic particle threats posted to geosynchronous satellites, we must understand these patterns of adiabatic motion.

A similar argument can be with the ring current population, and a corresponding space weather effect. In geostationary orbit, ring current particles accumulate on the spacecraft's surface, sometimes leading to spatial variation in surface charge. These spatial variations in surface charge (also known as "differential charging") can trigger pulsed discharges harmful to onboard electronics [70]. We can similarly ask: how does the adiabatic movement of ring current populations affect the time-dependent rate of spacecraft charging for satellites in geostationary orbit?

The adiabatic motion also has implications for research missions not in geosynchronous orbits, such as the Van Allen Probes [79]. The Van Allen Probes satellites orbited with an apogee of about 5.8 R_E, which serves as a radial upper bound for the mission's outer radiation belt coverage. However, because particles are known to adiabatically move inwards and outwards radially, they will inevitably transition in and out of the satellite's coverage. The extent to which this occurs is relevant to studies using such data, as well as the interpretation of outer radiation belt data.

Finally, we consider an application between adiabatic motion and induced field changes from the ring current. The ring current is the primary source of magnetic field depletion at the Earth's surface during geomagnetic storms, whose strength is often stated in terms of the D_{st} index. The induced change to the magnetospheric magnetic fields caused by the ring current can be calculated with the Biot-Savart law [147], $\mathbf{\Delta B}(\mathbf{r}) = \frac{\mu_0}{4\pi} \iiint_{\text{RingCurrent}} \frac{\mathbf{J}\times\mathbf{r}'}{|\mathbf{r}'|^3} dV$, wherein the change from magnetic field $\mathbf{\Delta B}$ due to the ring current is calculated through an integral over the ring current region, with current density $\mathbf{J}$, positions $\mathbf{r}$ and $\mathbf{r}'$, and infinitesimal volume dV. In this equation, we bring attention to the $1/|\mathbf{r}'|^3$ term, which shows that the $\mathbf{\Delta B}$ at a location in the magnetosphere is connected to its distance to each infinitesimal volume of the ring current having a notable current density. This change in the magnetic field strength due to changes in the ring current will alter the drift shells of trapped energetic particles.

In this dissertation, we quantify the adiabatic motion using a method centered around the

theory of adiabatic invariants. Our method, *Invariant Matching*, pairs mirror points of equal K and L^* over space from distinct magnetospheres. This can be viewed through the lens of a particle's drift shell adapting in shape to conserve K and L^* under newly encountered fields. We note that K and L^* alone dictate the drift shell structure because, for our considered populations, the gyro-radius is extremely small compared to the spatial scales of the bounce and drift motions.

Our method is a computationally efficient alternative to particle tracing when adiabatic motion free from non-adiabatic effects is considered. While it is well understood that non-adiabatic effects occur in nature, the results derived from our method can be interpreted as theoretical features pertaining to fundamental transitional behaviour between pairs of magnetospheres. We call this pure adiabatic motion between two sets of global magnetic fields *idealized adiabatic motion* to emphasize the calculation's independence from any non-adiabatic effects.

In this work, we model and discuss idealized adiabatic motion during a geomagnetic storm using the semi-empirical magnetic field model driven by L_1 solar wind measurements and the D_{st} index. We quantify the adiabatic displacement of mirror points between a storm time commencement, time of D_{st} minimum, and nominal recovery time to understand the scale at which particles move adiabatically within a storm.

Because changes to the global magnetic field are entirely driven by currents throughout the magnetosphere, we also study the adiabatic response to individual current system enhancements. The current systems we study are the ring current, tail currents, Birkeland currents, and Chapman-Ferraro currents. Specifically, we vary each current system individually and observe the adiabatic response. Because these currents ultimately drive each significant distortion of the global magnetosphere magnetic field, it is helpful to understand their respective contributions to adiabatic motion.

3.2 Current Systems and the TS05 Model

We use the Tsyganenko/Sitnov 2005 (TS05) model to model the global magnetospheric magnetic field. This semi-empirical model of the global magnetospheric magnetic field combines both

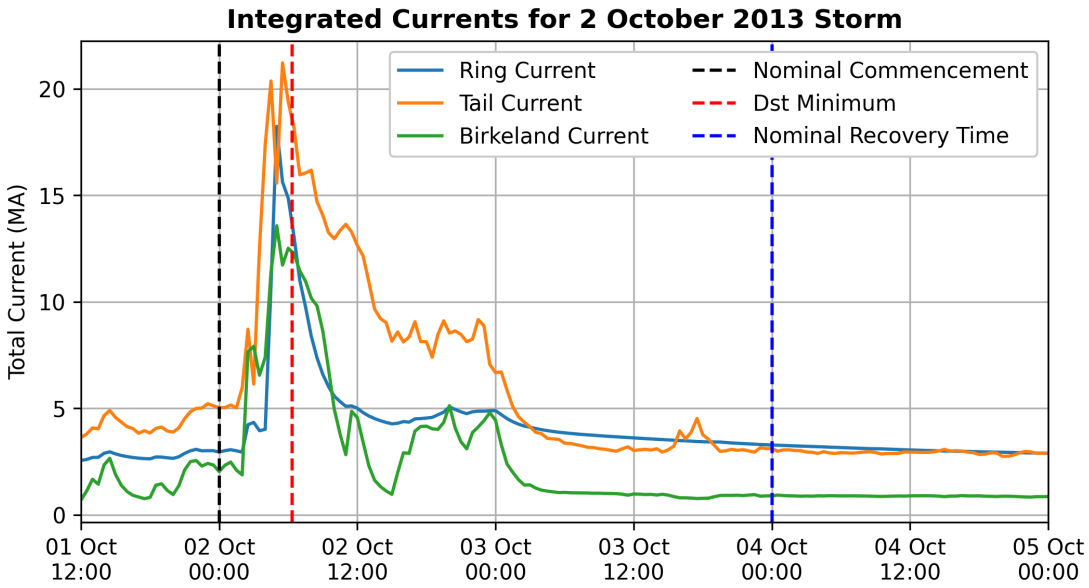

Figure 3.1: Integrated currents throughout a geomagnetic storm, showing variation on a scale of about 4X between the quiet-time intensity and the intensity at the time of D_{st} minimum.

physical modeling and a history of satellite observation in a comprehensive modeling approach refined over multiple decades [130, 129, 126, 128, 134, 124]. Interior to the magnetopause, this model calculates the overall magnetic field $\mathbf{B}_{\text{Final}}$ as the sum of seven contributing vectors,

$$\mathbf{B}_{\text{Final}} = \mathbf{B}_{\text{CF}} + \mathbf{B}_{\text{TAIL1}} + \mathbf{B}_{\text{TAIL2}} + \mathbf{B}_{\text{SRC}} + \mathbf{B}_{\text{PRC}} + \mathbf{B}_{\text{BIRK1}} + \mathbf{B}_{\text{BIRK2}} + \mathbf{B}_{\text{IMF}}, \tag{3.1}$$

where $\mathbf{B}_{\text{CF}}$ represents the contribution from the Chapman-Ferraro current system, $\mathbf{B}_{\text{TAIL1}}$ and $\mathbf{B}_{\text{TAIL2}}$ from two regions of tail currents, $\mathbf{B}_{\text{SRC}}$ from the "symmetric" ring current, $\mathbf{B}_{\text{PRC}}$ from the "partial" ring current, $\mathbf{B}_{\text{BIRK1}}$ and $\mathbf{B}_{\text{BIRK2}}$ from two regions of the Birkeland currents, and $\mathbf{B}_{\text{IMF}}$ from the penetrated component of the interplanetary magnetic field (IMF). We note that the penetrated component, unlike the others, does not nominally correspond to a magnetospheric current system for the purposes of this dissertation.

Tsyganenko describes their rationale for splitting some current systems into two terms [130]. For the tail currents , two distinct tail current regions are used to separately model inner and outer cross-tail current. Two Birkeland currents allow for shifting the current peaks longitudinally, where

Region 1 corresponds to current peaks at dawn and dusk and Region 2 corresponds to current peaks at noon and midnight. The symmetric ring current differs from the partial ring current in that the symmetric ring current is axially symmetric, while the partial ring current includes the effects of field-aligned currents associated with the local time asymmetry of azimuthal near-equatorial currents [128].

In Figure 3.1 we display time-varying metrics for current system intensity for three current groups during the geomagnetic storm beginning on October 2, 2013: the ring current ($\mathbf{B}_{\mathrm{PRC}}$ and $\mathbf{B}_{\mathrm{SRC}}$), tail current ($\mathbf{B}_{\mathrm{TAIL1}}$ and $\mathbf{B}_{\mathrm{TAIL2}}$), and Birkeland currents ($\mathbf{B}_{\mathrm{BIRK1}}$ and $\mathbf{B}_{\mathrm{BIRK2}}$). This demonstrates how the intensity of each current system varies overall on a scale of about 4X between the quiet time intensity and the intensity during the storm's D_{st} minimum. This plot is prepared with the total current integrated over a surface using the equation,

$$\mathrm{TotalCurrent} = \iint \frac{1}{\mu_0} |\nabla \times \sum \mathbf{B_i}| dA, \tag{3.2}$$

where $\mathbf{B_i}$ are the magnetic field vectors from the terms considered. The integration surface used is the midnight X-Z plane bounded by $X > -20\ R_E$ (Solar Magnetic coordinates) for the ring current and tail current. The integration surface for the Birkeland current is the X-Y plane at $Z = 1.1\ R_E$, to place the the surface where the Birkeland currents take their field-align direction.

The model itself computes each of the contributing vectors as a function of upstream solar wind conditions and geomagnetic state. Specifically, the input variables are the IMF B_y and B_z, the D_{st} index, the interplanetary dynamic pressure P_{dyn}, and six time-dependent parameters W_1 to W_6 that allow the model to account for the growth and decay of persistent currents.

This work investigates the adiabatic responses of ring current and radiation belt particles to individual current systems. An illustration of the combined current sources can be found in Figure 3.2, which shows the current density calculated from the equation

$$J_{ext} = \frac{1}{\mu_0} |\nabla \times \mathbf{B_{ext}}|, \tag{3.3}$$

where $\mathbf{B_{ext}}$ is the external magnetic field vector obtained from TS05, $\mathbf{J}_{ext}$ is the current density associated with the perturbed (non-dipole) fields, and μ_0 is the vacuum magnetic permeability. This

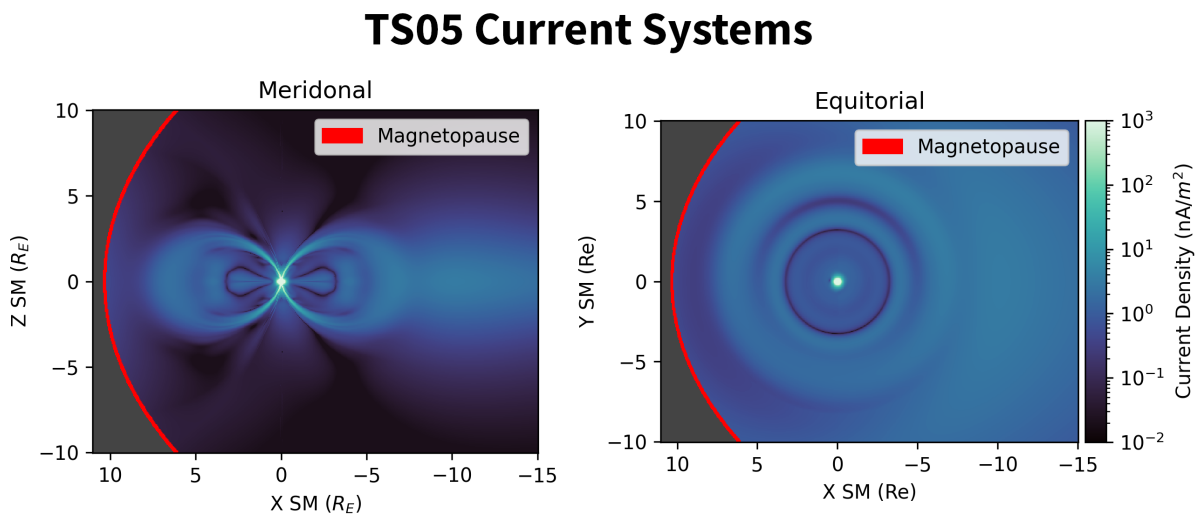

Figure 3.2: Model cuts displaying the current systems extracted from the Tsyganenko/Sitnov 2005 (TS05) model, using Equation 3.2.

example is driven by the inputs $P_{dyn} = 1.64$ nPa, $D_{st} = -7.0$ nT, $B_y = -2.7$ nT, $B_z = -1.2$ nT, $W_1 = 0.338$, $W_2 = 0.469$, $W_3 = 0.063$, $W_4 = 0.248$, $W_5 = 0.337$ and $W_6 = 0.58$. These inputs correspond to the commencement time of the storm, which will be described later. In this plot, we see a complex description of the global magnetosphere, including multiple layers of ring current, a tail current, and cavities of current density immediately around the polar regions.

Our work will investigate the influence of individual current systems by artificially scaling terms of Equation 3.1 to enhance each system. This is implemented using a modified version of the official Fortran TS05 code, with the original available at `https://geo.phys.spbu.ru/~tsyganenko/empirical-models/magnetic_field/ts05/`. Specifically, the function that holds the code that adds the contributing terms is modified to accept scale factors used to multiply each contributing term.

3.3 Invariant Matching Methodology

We seek to describe the adiabatic motion of ring current and radiation belt particles between a pair of magnetospheres. The key state of a trapped particle is its adiabatic invariant coordinate

(M, K, L^*) that describes its trapped state. For this manuscript, we will accept that the three adiabatic invariant coordinates (M, K, L^*) can be calculated in conjunction with a magnetic field model from a starting position $\mathbf{x}_0$, a particle rest mass m_0, and mirroring field intensity B_m.

The approach used is to associate particles mirroring at a known point along a fixed drift shell and, through computational methods, match them to the mirror point under a new drift shell they would adiabatically transition to under a modified global magnetic field, in the absence of any non-adiabatic effects such as wave-particle interactions. We calculate the idealized adiabatic motion between a starting and ending magnetosphere. The approach begins by preprocessing the ending global magnetic field. A grid of positions on an X-Z slice of Solar Magnetic (SM) space is associated with adiabatic coordinates corresponding to a particle thatch mirrors there. This produces a "mapped" dataset which maps a grid of mirror positions (X_{ij}, Z_{ij}) to adiabatic coordinates (K_{ij}, L^*_{ij}).

The invariant matching grid is irregular 0.1), and the magnetic latitude ϕ of a mirror point along each field line between $-61°$ and $61°$ (in increments of $2°$) with extra points placed at $\pm 0.1°$ around the equator. These extra points were placed to extend the minimum K which could be interpolated, due to the singularity that arises from interpolating K in log-space. Each mirror point magnetic latitude, whether positive or negative, yields the mirroring field strength B_m, which inherently specifies the opposite mirror point location along that field line. This grid is designed to cover the region of space occupied by outer radiation belt elections and includes a variety of mirroring states. Through this mapping process, each of the (L, ϕ) grid points is connected to a (K, L^*) coordinate.

The mapped dataset describing the ending magnetosphere is used to match adiabatic coordinates (K, L^*) from the starting magnetosphere with the mirror point locations in the ending magnetosphere. For each mirror point in the starting magnetosphere, the mapped dataset is interpolated to find the corresponding (X, Z) position where the mirror points displace to in the ending magnetosphere. In Figure 3.3 we show the adiabatic coordinates of the mapped ending magnetosphere mirror points colored by their X and Z coordinates, with the adiabatic coordinates

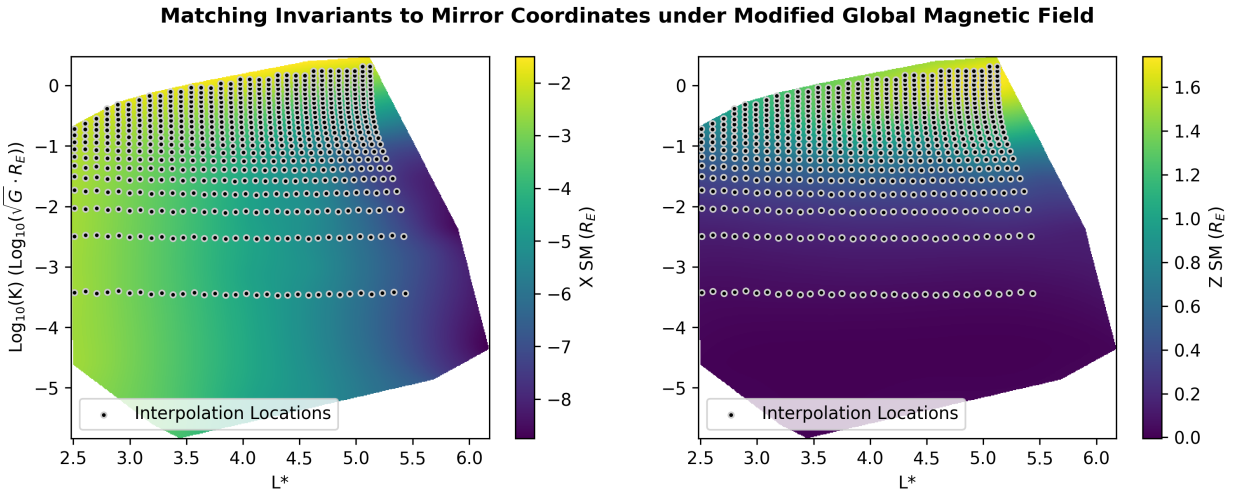

Figure 3.3: Adiabatic invariant coordinates (K, L^*) in the ending magnetosphere are computed for particles mirroring on a grid of L and magnetic latitude ϕ at a fixed local time. The X and Z variables correspond to the SM mirror point location at the local time. This mapping $(K, L^*) \mapsto (X, Z)$ is interpolated to find the location of the mirror point for a (K_0, L_0^*) particle originating from the starting magnetosphere.

of the starting magnetosphere mirror points as black/white circles.

The interpolation done is in log-scale for the K coordinate, which naturally spans about 7 orders of magnitude. To interpolate, a radial basis function method is used from the SciPy package [140]. Specifically, we use multiquadratic basis functions of the form $b(r) = \sqrt{(r/\epsilon)^2 + 1}$ where $b(r)$ is the radial basis function, r is the radius, and ϵ is equal to the average distance between data points. The smoothness setting is used to force the interpolation function to always go through the data points. This method was chosen because of its effectiveness working with scattered data. Care is taken not to extrapolate the mapped dataset; if at any time one of the interpolation locations is not fully within the enclosed bounds of the mapped data points then the adiabatic motion is not computed. This constraint is accomplished by checking whether the interpolation location is within the convex hull of the mapped data points.

We now discuss the scope of this methodology. This methodology may be applied where the three invariants are conserved for the particles in question. Previous studies of trapped particle motion have identified a number of cases where the invariants are not conserved, which we review

here. Generally speaking, if M is not conserved, then K and L^* are also not conserved, and if K is not conserved, L^* is not. Known scenarios where one or more invariants are broken include:

- **Highly curved field lines**, where the gyro radius approaches the curvature radius of the field line.
- **Spatially sheared field lines**, where there is a sudden large change in field line direction over space, such as around the magnetotail current sheet.
- **Drift Orbit Bifurcation (DOB)**, such as around the dayside Shabansky region.
- **Rapid changes to the magnetic field topology**, such as where there the global magnetic topology alters the motion of the particle on a scale faster than the drift period.
- **Large gradients in the field line strength**, such as around the magnetopause and magnetosheath boundary layer (MSBL).
- **Resonant Wave-Particle Interactions**, such as but not limited to chorus or ULF waves.

Detailed discussion of each of these scenarios is outside the scope of this dissertation. For issues regarding curvature of field lines and the magnetotail, see [6]. For wave-particle interactions see [137] and [37] when concerned with ULF waves, and [4] for chorus waves.

3.4 Results

3.4.1 Idealized Adiabatic Motion Between Storm Times

We now turn our attention to studying the idealized adiabatic motion during a geomagnetic storm, nominally beginning on 2 October 2013. This storm, studied in Chapter 2, was triggered by a coronal mass ejection (CME) [84] with mostly $B_y^{IMF} < 0$ plasma and flow speeds in excess of 600 km/s. The magnetosphere's response reached a minimum D_{st} of -90 nT during the peak of the storm.

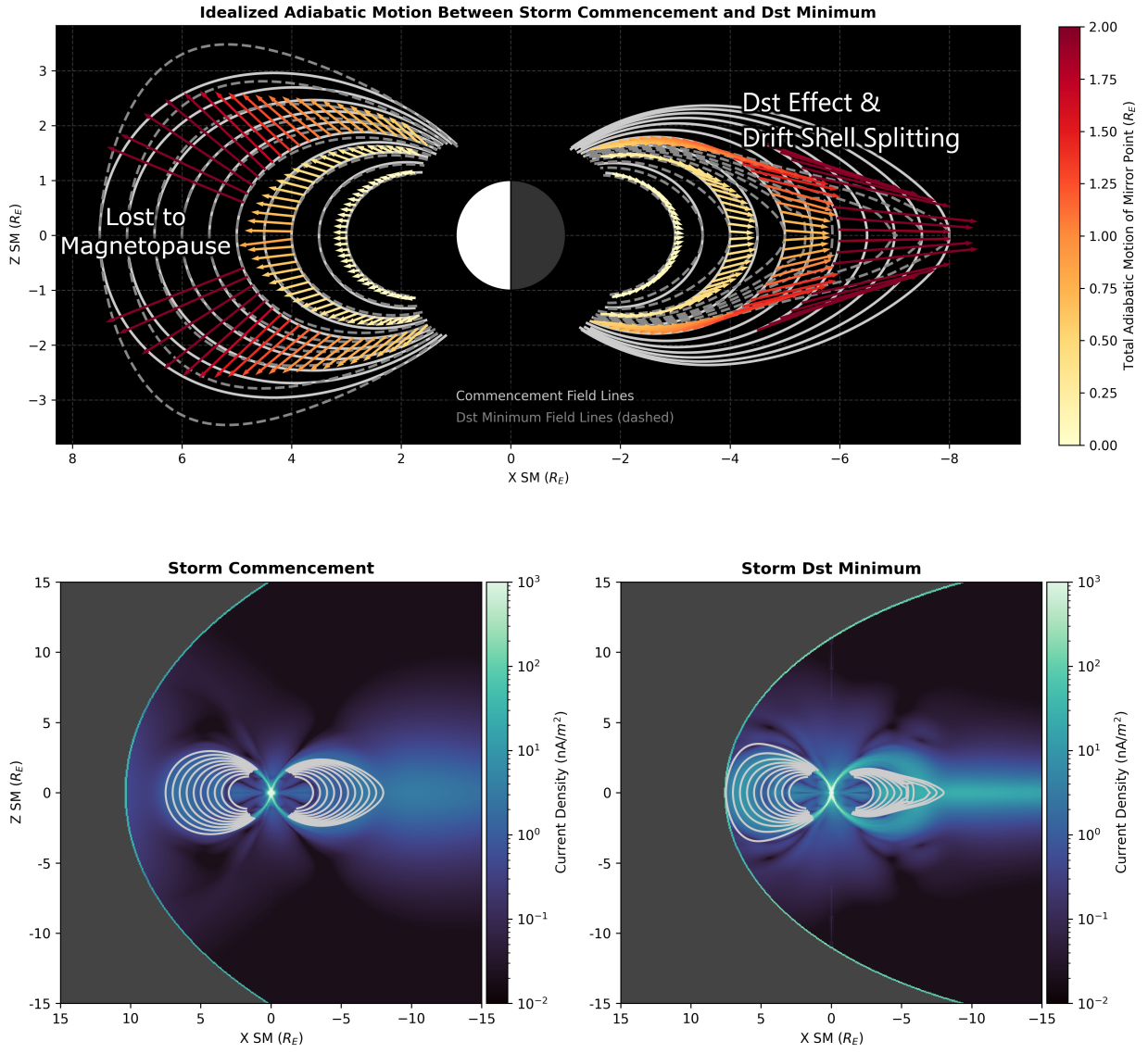

Figure 3.4: Idealized adiabatic motion between a nominal storm commencement time and the time of D_{st} minimum for the storm, displayed through the displacement of mirror points. The bottom two panels show the total external field current density, computing using Equation 3.3.

We study the idealized adiabatic motion between three times in the storm: (a) a nominal commencement time immediately preceding the CME, (b) the time of minimum D_{st}, chosen to reflect the most disturbed state, and (c) a nominal recovery time about two days after the commencement, when the solar wind dynamic pressure had since returned to its baseline value and

there no longer existed a strong southward B_z^{IMF}.

Though it is generally understood that adiabatic breaking behaviour would occur between the commencement and main phase, we apply this method to a storm to demonstrate the scale of adiabatic influence. The adiabatic motion between the storm commencement and the time of D_{st} minimum is displayed in the top panel of Figure 3.4 . Each of the vectors drawn in this plot is between a mirror point in the commencement magnetosphere and its corresponding adiabatically displaced mirror point in the D_{st} minimum magnetosphere. The bottom two panels show the external current densities (from all external current sources) for each magnetosphere computed using Equation 3.3. The commencement magnetospheric field lines are drawn in white, and the D_{st} minimum field lines are drawn in gray.

We notice a number of interesting features in these plots. The magnitude of the adiabatic mirror point displacement is largest furthest away from the Earth, where the external field dominates. As expected, the D_{st} minimum dayside magnetosphere is significantly more compressed than during the storm commencement. On the dayside, we also see that the adiabatic displacement of the mirror points tends to be broadly in the direction perpendicular to the field line. We label a region around the magnetic equator where the adiabatic motion would have displaced mirror points past the magnetopause, in a well-understood phenomena known as magnetopause shadowing or magnetopause incursion [58]. Magnetopause shadowing affects particles in pitch angle bands around 90°. Through the dropouts of particles in these pitch angle bands, the phenomena is known to instigate doubly-peaked "butterfly" pitch angle distributions. The features observed here are consistent with test particle simulations of magnetopause shadowing [101], Fokker-Planck simulations [145], and phase space density observations [118, 136, 111, 76, 115].

Moving on the tail portion of Figure 3.4, we observe a combined influence of the Dst effect and drift shell splitting. The experiment depicts latitude-dependent outward mirror-point displacement within the same starting field line (attributable to drift shell splitting), with the strongest displacement just outside the ring current region (widely known as the Dst effect). There are two peaks in total displacement magnitude at roughly the same absolute magnetic latitude. This can

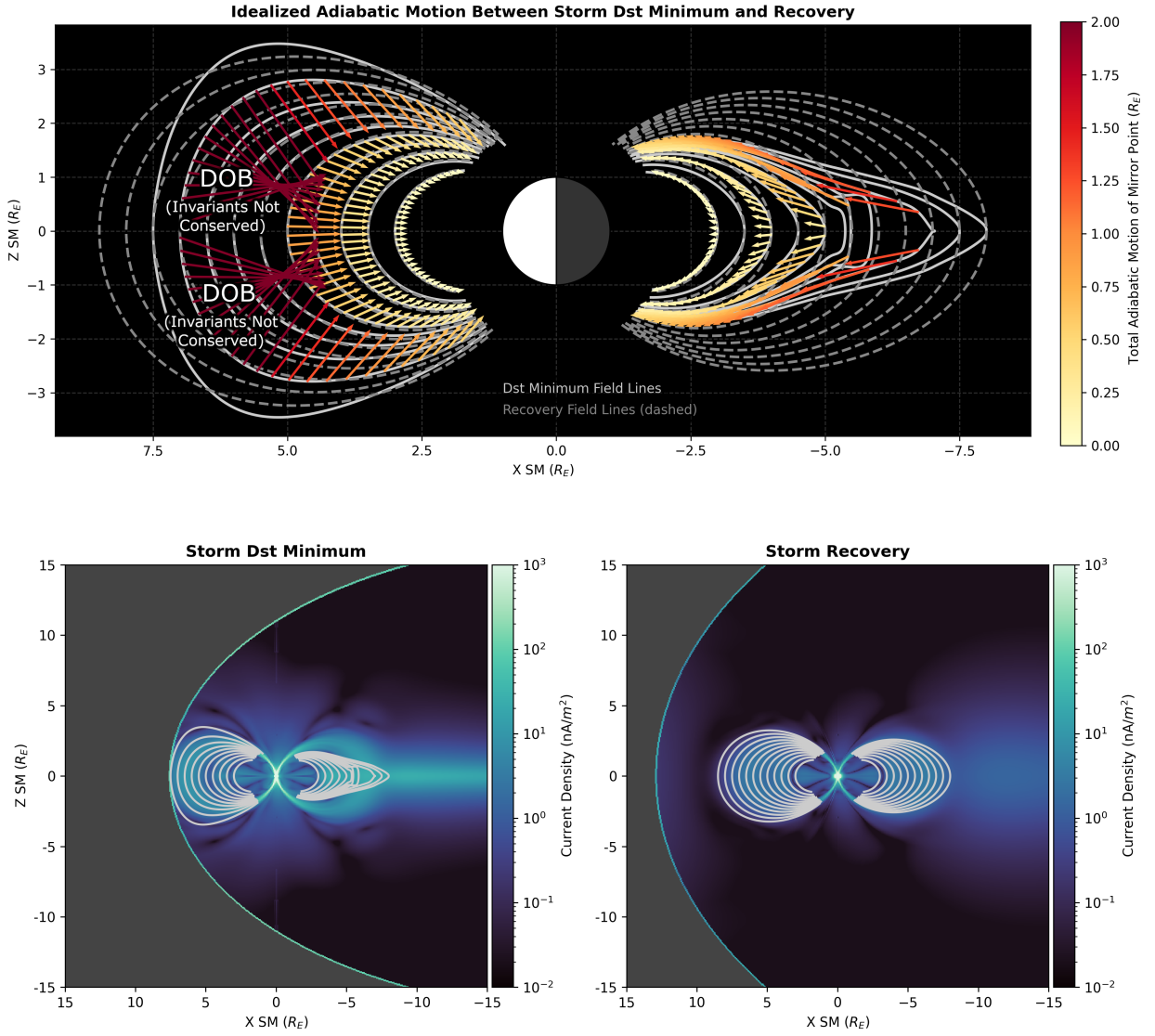

Figure 3.5: Idealized adiabatic motion between the time of minimum D_{st} for the storm and a nominal recovery time over 36 hours later, displayed through the relocation of mirror points. DOB stands for drift orbit bifurcation. The bottom two panels show the total external field current density, computed using Equation 3.3.

be expected to lead to interesting changes in the equatorial pitch angle distributions as would be measured at increasing L values into the tail. That is, the equatorial pitch angle distribution versus L would change in shape/structure from particles being exchanged in pitch angle dependent amounts across L-shells.

The adiabatic motion between the D_{st} minimum for the storm and the nominal recovery time over 36 hours later is displayed in Figure 3.5. We note signatures of a well known phenomena known as drift orbit bifurcation (DOB). This phenomenon occurs in a region of the dayside magnetic field known as the Shabansky region [108, 80]. In the Shabansky region, each magnetic field line is "hammer-head" shaped as it contains two local minima in magnetic field strength. Each of these local minima is located near each cusp [92]. Test particle simulations have confirmed that when particles of sufficiently low B_m pass through these regions they become trapped within one of the two local minima, with the minimum chosen being effectively stochastic [109].

In Figure 3.5, we observe the results of invariant matching on the dayside for drift shell mirror points subject to DOB effects at the time of D_{st} minimum but not during recovery. The pitch angle dependent dynamics of entering and leaving the Shabansky region have been reported in McCollough et al., 2012 [80]. McCollough et al.'s work describes three types of particles encountering the region, labeled as Type I, II, and III. Type I particles are those of high K that undergo dayside drifts without mirroring inside the bifurcated region; in many ways they are unaffected by the unique Shabansky structure. Type II and III particles are those which mirror inside the bifurcated region, spending their time at high latitudes while in the Shabansky region. The difference between Type II and III particles is that Type II particles have small K (which is conserved after leaving the Shabansky region), and Type III particles have an even smaller near-zero K (which is not conserved after leaving the Shabansky region). While mirroring inside the Shabansky region, a standard prescription is that the full value of K is partitioned between minima, such that $K = K_1 + K_2$. It is common, though not entirely accurate, to approximate K_1 and K_2 with $K_1 = K_2 = K/2$.

Our model of idealized adiabatic motion accurately describes Type I and II particles, but less so for Type III particles. This is necessarily because K, and therefore L^*, are not conserved after leaving the region for Type III particles, which violates a key assumption of the Invariant Matching method. The arrow crossing in Figure 3.5 can be understood to occur at the mirroring latitudes which effectively act as classification boundaries between Type I and II particles. We note that a similar but reversed DOB effect occurred between commencement and D_{st} minimum for particles

drifting on the dayside around $L = 6$ in the commencement magnetosphere, but it was cropped out of Figure 3.4 for visual simplicity.

We note that the changes to K and L^* for Type III particles were reported in McCollough et al., 2012 [80] be small within a drift. Their work showed at each drift, K about doubled in value when entering/exiting the Shabansky region a single time. This is notabaly small compared to the seven orders of magnitude of K across a field line observed in our work (Figure 3.3). It was reported in that work that this per-drift change in K and L^* would repeat in the form of a diffusive process. For this reason, we do not claim exact results for near-equatorial Type III particles in the Shabansky region.

3.4.2 Idealized Adiabatic Motion In Response to Current System Enhancements

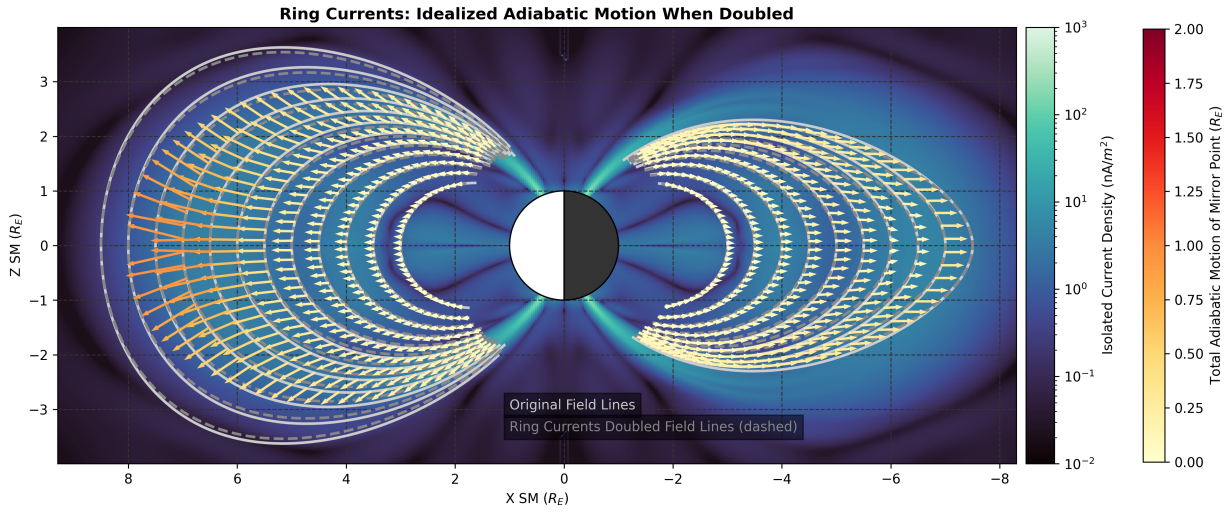

Figure 3.6: Idealized adiabatic motion when the ring current intensity is doubled. The background shows the external field density consisting of just the ring current source terms, computed using Equation 3.3.

Using this method as our tool of study, we now turn our attention to the relative role of magnetospheric current systems on adiabatic motion. We perform experiments for each of four major current systems: the ring current, the tail current, the Chapman-Ferraro current, and the Birkeland current. As outlined in Equation 3.1, the ring current corresponds to the field source

terms $\mathbf{B}_{\mathrm{PRC}}$ and $\mathbf{B}_{\mathrm{SRC}}$, the tail current to $\mathbf{B}_{\mathrm{TAIL1}}$ and $\mathbf{B}_{\mathrm{TAIL2}}$, the Chapman-Ferraro current to $\mathbf{B}_{\mathrm{CF}}$, and the Birkeland current to $\mathbf{B}_{\mathrm{BIRK1}}$ and $\mathbf{B}_{\mathrm{BIRK2}}$,

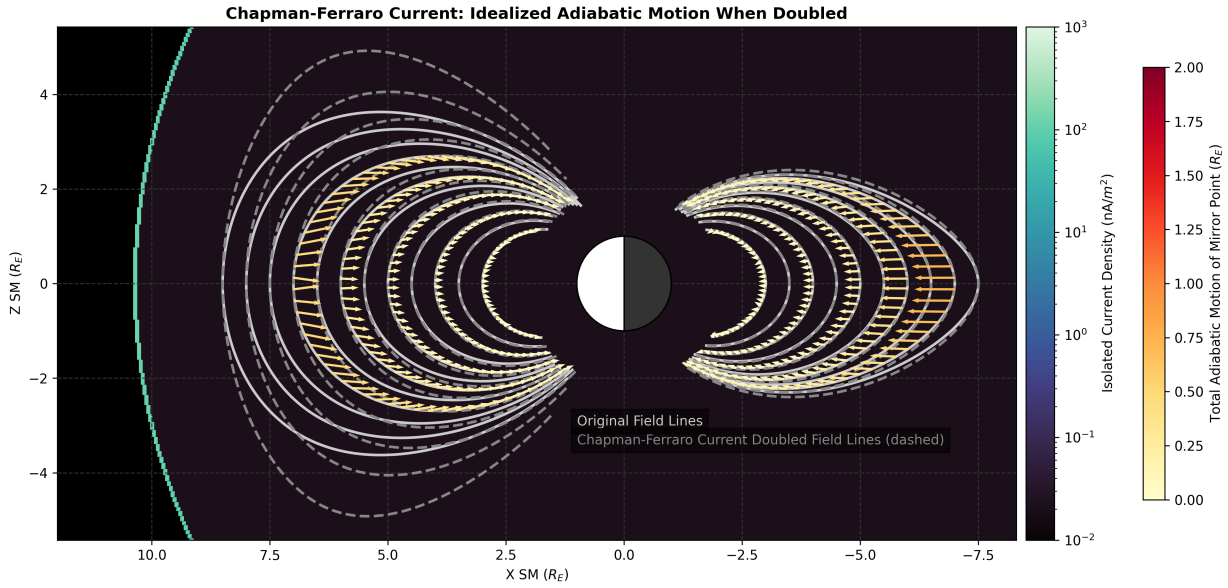

Figure 3.7: Idealized adiabatic motion when the Chapman-Ferarro current intensity is doubled. The background shows the external field density consisting of just the Chapman-Ferarro source, computed using Equation 3.3.

In this experiment, we use a nominal magnetosphere taken during the storm commencement (labeled in Figure 3.1) as the starting magnetosphere. For the ending magnetosphere, we double the intensity of the major current system being studied. This is done by doubling the corresponding field source terms in Equation 3.1. For example, when we compute a magnetosphere with a double the ring current intensity, we compute a new magnetosphere with the $\mathbf{B}_{\mathrm{PRC}} + \mathbf{B}_{\mathrm{SRC}}$ terms replaced with $2(\mathbf{B}_{\mathrm{PRC}} + \mathbf{B}_{\mathrm{SRC}})$, leaving the other terms the same.

The purpose of this exercise is to understand the adiabatic response of radiation belt and ring current particles to enhancements of each major current system. In Figure 3.1's display of integrated currents throughout a storm, we notice that the relative intensity of each current group

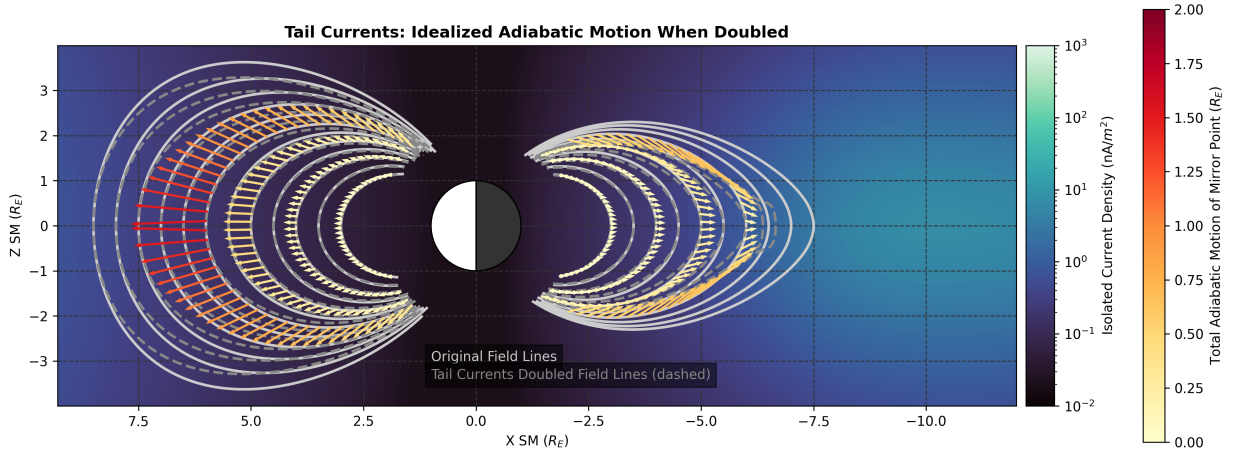

Figure 3.8: Idealized adiabatic motion when the tail current intensity is doubled. The background shows the external field density consisting of just the tail current source terms, computed using Equation 3.3.

varies throughout the storm. For example, we notice that while both the tail current and the ring current reach their maximum intensity around the time of D_{st} minimum, the ring current intensity in the model drops more rapidly than the tail current. By analyzing the adiabatic responses to each major current system, we move towards a more detailed understanding of the adiabatic responses throughout a storm on hourly time scales.

In Figure 3.6, we observe the effect of doubling the ring current intensity in our nominal magnetosphere. This enhancement results in outward displacement of mirror points on both the nightside and dayside. We observe that the vertical change Δz in the mirror point location is small on the nightside, but latitude-dependent on the dayside. On the dayside outer most field line with vectors plotted, we see the adiabatic motion begin to point to rearrangements (on the equator) around the equator corresponding to DOB. This result indicates that a ring current enhancement of the magnitude, alone, is enough to displace particles onto the DOB field lines, without any compression of the magnetosphere. This is notable, as it reminds us that ring current enhancement can push higher L particles into this region, even with a steady magnetopause location.

The adiabatic effects of doubling of the Chapman-Ferraro current, displayed in Figure 3.7,

shows a different story. This current doubling, which has a notable effect on the shape of the dayside field lines, overall results in inward mirror point displacement, with minimal Δz vertical movement on both the dayside and the nightside.

The effects of the tail current, displayed in Figure 3.8, show largely outward motion. On the dayside, the Δz of the mirror point displacement is clearly latitude dependent, with more Δz at higher magnetic latitudes. On the nightside, this relationship between magnetic latitude and Δz is missing lower at L, and at higher L is overcome by effects of the tail stretching.

Similar to the other analysis, the effects of the Birkeland current is also analyzed. It was found that when doubled, the adiabatic response to the Birkeland current is extremely small and most likely negligible compared to these other current systems.

3.5 Summary

In this work we present a new method for quantifying adiabatic motion for particles in the radiation belts and ring current. Our method works by tracking the displacement of mirror points, pairing a starting mirror point with its ending location using a mapped version of the ending magnetosphere. This approach makes it easy to compute and visualize vector fields corresponding to the relocation of mirror points throughout the magnetosphere. Though not pictured here, this method could be applied to the dawn/dusk local times in addition to noon and midnight.

Results from this method yield features such as magnetopause shadowing, drift orbit bifurcation, and a combination of the Dst effect and drift shell splitting. These features are found consistent with existing observations and test particle simulations in the literature [101, 145, 118, 136, 111, 76, 115], serving as a simple validation of the method.

In particular, the drift orbit bifurcation patterns can be explained by displacement to conserve B_m during a transition from Shabansky field line to a normal field line. In our observations of magnetopause shadowing, we observed how invariant matching can capture the effects of drift shells displacing past the magnetopause. The observation of L-shell spreading indicates that particles which once collocate a single field line at a given MLT can become spread out across multiple field

lines at that MLT from adiabatic effects alone.

The magnetospheric system's adiabatic response to enhancements of individual current systems was also analyzed. We looked at current groups as modeled through the TS05 model, including the ring current, the Chapman-Ferraro current, the tail current, and the Birkeland current. We noted that enhancements in the ring current and tail currents generates outward motion, an enhancement to the Chapman-Ferraro current generates inward motion, and the effect of the Birkeland current is largely negligible.

This work has presented analyses of adiabatic responses to storm-time magnetospheric deformations and responses to individual current system enhancements, which are important analysis tools to begin with when applying the method. Future potential applications include complementing existing modeling using this independent method which has the bonus of being more computationally efficient. Topics include modeling of magnetopause shadowing, such as quantifying the span of pitch angles at each L which undergo loss after an adiabatic response due to a changing location of the magnetopause. Other applications include addressing the topics mentioned in the introduction: (a) geosynchronous satellite vulnerability to single event effects and spacecraft charging, (b) outer radiation belt coverage for observational satellites like the Van Allen Probes, and (c) changes to $\mathbf{B}$ at Earth and throughout the inner magnetosphere due to displacement of the ring current.

Chapter 4

Phase Space Density Organized by Adiabatic Invariants

The text in this chapter is based on the publication "Radiation Belt Phase Space Density: Calculation Analysis and Model Dependence" by da Silva et al., accepted to Frontiers in Astronomy and Space Sciences, in 2024.

4.1 Introduction

The conversion of flux to phase space density and recasting of the coordinates in terms of adiabatic invariants is known as *phase space density analysis*, which results in the model-supplemented measurement $f(M, K, L^*)$ [56, 62], [27], [136]. Typically, to aid visualization, M and K are held constant, and one curve of $f(L^*)$ per inbound/outbound arm of an orbit is plotted. This curve can then be used to demonstrate changes to the (M, K) population at each L^*, which may occur from additions, losses, or redistribution of a (M, K) population across L^*.

The implementation details of combining a flux measurement with a global magnetic field model vary in the literature. Most commonly, the global magnetic field model used is an empirical model, often either Tsyganenko models TS05 and T96 [134, 130]. In this chapter, we seek to answer the question as to whether the interpretation of phase space density analyses differs dramatically when the same data is reprocessed using different models. In this chapter, we use data from two empirical models and two MHD-driven simulations: T96 (empirical), TS05 (empirical), the Space Weather Modeling Framework (SWMF; an MHD model; [122]) and Lyon-Fedder-Mobarry (LFM; an MHD model [77]), both at similar resolutions and coupled with the Rice Convection Model

(RCM; [121]) for stronger ring current modeling.

The magnetic field model is not the only implementation detail that varies in the literature. Aside from issues of the magnetic field model and calculating the invariants themselves, differences in the numerical methods to convert the flux measurement to phase space density at the given adiabatic invariant coordinate arise in the literature. Among these numerical differences are different approaches to fitting and interpolation, done with varying degrees of agency applied to smoothing the measurements.

To illustrate the numerical differences, we will give a motivating example. In the calculation, which will be described step-by-step later on, there is a step where the flux $j(E, \alpha)$ is put in terms of just $j(E)$, and it is required to interpolate this curve at a fixed E. Methods for interpolating $j(E)$ are as follows:

- Fitting $j(E)$ to a power law distribution [49]
- Converting $j(E)$ to $f(E)$ and fitting to an exponential distribution [46]
- Use of a smoothing spline the $j(E)$ curve with both the dependent and independent variables in log space [22, 21]

In this work, we will demonstrate that the choice for this step is in some cases significant enough that changing the approach causes a result that exhibits evidence of internal acceleration to change to a result that shows evidence of radial diffusion.

In order to strengthen the foundation of the phase space density analysis methodology and related results in the literature, this manuscript aims to study each effects of model dependence and as many implementation options as possible. By doing this, we aim to provide a more stable groundwork for this computational technique in relating radiation belt theory to observational evidence.

This chapter consists of three body sections. In the *Data and Models* section, we describe the data and models used for this study. In the *Calculation Analysis* section, we review each step of the calculation and the different implementation options known to exist. Discussion is made

between the various implementation options with commentary as to which are essential and which are minor, and plots are presented showing the differences in doing the calculation each way. This section intends to cover every numerical approach that may be used (such as those that would be impossible to cover within an article), but instead, it will cover the most reasonable and widely used techniques in the community. In the *Model Dependence* section, we use a set of nominal implementation options for the algorithm and apply them with different magnetic field models, studying the differences in the results for three distinct classes of radiation belt enhancements. These classes are taken from the previous work of Boyd et al., 2018 [22], and correspond to (a) Growing Peak Events, (b) Flat Gradient Events, and (c) Positive Gradient Events.

4.2 Calculation Analysis

In a phase space density analysis, magnetospheric magnetic field models are used to provide a value for $\mathbf{B}(\mathbf{x}, t)$ throughout the magnetosphere. Strictly speaking, it is only required to cover (a) the drift shell of the target (M, K) particle class at each L^*, and (b) the highest north/south latitude reached on the bounce path of the highest measured pitch angle at each spacecraft position. In practice, it is easiest to assume modeling capability for everywhere between the surface of the earth and a few R_E above the spacecraft apogee (to allow for effects such as drift shell splitting).

The only required measurement is that of a flux distribution $j(E, \alpha; \mathbf{x}, t)$ which, if not directly available in a mission dataset, can be computed from $j(\mathbf{v}; \mathbf{x}, t)$ or $j(\mathbf{p}; \mathbf{x}, t)$ where $\mathbf{v}$ is a velocity and $\mathbf{p}$ is a momentum and a value of $\mathbf{B}$ at the spacecraft location. Strictly speaking, a measurement of $\mathbf{B}$ is not required, as one can attempt to acquire $\mathbf{B}$ from evaluating the model at the spacecraft location, though that is less desirable.

The seven calculation steps are outlined in Figure 4.1. When applicable, different implementation options for fulfilling each step are presented. These options were collected by reviewing key examples in the literature and consulting with community members. They represent the most reasonable and common approaches rather than a fully extensive set of all possible approaches. In this section, we will walk through each step, discussing the different implementation options listed,

Calculation Steps

Step 1† Caclulate K for Each Pitch Angle α

Step 2 Interpolate $\alpha(K)$ at fixed K to Find Target α

Option 2a
Calculate B_m using
|B| from Magnetometer

Option 2b†
Calculate B_m using
|B| from Model

Step 3 Interpolate $j(\alpha, E)$ to $j(E)$ at Target α

Option 3a
Fit to function
$j(\alpha) = c_0 \sin(\alpha) + c_1 \sin^n(\alpha)$

Option 3b
Fit to function
$j(\alpha) = c \sin^n(\alpha)$

Option 3c
Fit to Legendre
Polynomials

Step 4 Find Target E from Fixed First Invariant M

Option 4a
Calculate B_m using |B|
from Magnetometer

Option 4b†
Calculate B_m using |B|
|B| from Model

Step 5 Interpolate $j(E)$ at Target E

Option 5a
Interpolate with
Smoothing Spline

Option 5b
Interpolate with Power
Law Fit
$\log_{10}(j(E))$
$= c_0 \log_{10}(E) + c_1$

Option 5c
Interpolate with with
Exponential fit to PSD
$f(E) = c_0 \exp(-c_1 E)$

Step 6 Convert $j(E_0)$ to $f(E_0)$

Step 7 Calculate L^*

Option 7a
Calculate B_m using |B|
from Magnetometer

Option 7b†
Calculate B_m using |B|
|B| from Model

† Depends on Magnetic Field Model

Figure 4.1: Steps of the phase space density calculation, per timestep, using a fixed M and K selected for the computation.

with a particular eye on how each option may affect the analysis's effectiveness at organizing the data to distinguish between signatures of internal acceleration and radial transport.

The calculation steps are presented in terms of what to do for each time step. The calculation is done for particular fixed M and K which is to be selected before hand. In general, higher K correspond to pitch angles farther away from 90°, and higher M correspond to higher perpendicular energies at the magnetic equator.

Step 1 begins with pairing each pitch angle α_i of the data with a counterpart K_i, using separate code to calculate the second invariant K using a magnetic field model. The work of Konstantinidis et al., 2015 [66] and has investigated the differences in the calculated second invariants (they used I of K) between codes and backing magnetic field models. They found that there was generally good agreement between the codes tested for evaluation of the second invariant. The codes evaluated in that work were IRBEM [19], SPENVIS [69, 53], and a particle tracer.

The second step is to interpolate the curve of (K_i, α_i) from the previous step to determine the calculation's target pitch angle from the target fixed K selected. A reasonable way to interpolate $\alpha(K)$ is so using linearly interpolation with K in log space. Experiments were performed where we interpolated $\alpha(K)$ using splines and it was found that differences were non-consequential.

Step 3 includes more variation in the implementation options. In this step, one interpolates the $j(\alpha, E)$ flux measurement at the target α found from Step 2, and produces a one-dimensional $j(E)$ curve. This step can be done by stepping through each energy channel and fitting the pitch angle flux distribution at that energy to a functional form which is then interpolated. This is best done in combination with time averaging to mitigate the effects of noise that may result from low counting statistics.

Methods for fitting this functional form include fitting to the following functional form:

$$j(\alpha) = c_0 \sin(\alpha) + c_1 \sin^n(\alpha), \tag{4.1}$$

which was used early on in phase space density analysis in Green et al., 2004 [46] and stated to be designed as a method of fitting both butterfly and highly peaked distributions. Other methods

include the simpler functional form [44, 107, 47, 86],

$$j(\alpha) = c \sin^n(\alpha), \tag{4.2}$$

which may be easier to numerically fit [139], but is capable of modeling fewer pitch angle distribution shapes. In the work of Boyd et al., 2012 [21] a method is presented which fits $\log_{10}(j(\alpha))$ to a set of orthogonal basis functions known as the Legendre polynomials, which have the added benefit that the fitted $j(\alpha)$ may be guaranteed symmetric through the use of only even-term basis functions, which is desirable as a method of removing noise when $j(\alpha)$ truly is symmetric.

Step 5 involves finding the target E where we will interpolate along the $j(E)$ curve. This is done by using the fixed first invariant M, which can be written as a function of E, our target α, and the magnetic field strength $|B|$. The equation for M written this way is [49],

$$M = \frac{(E^2 + 2m_0c^2E)\sin^2(\alpha)}{2m_0|B|c^2}. \tag{4.3}$$

When α, M, and $|B|$ are known and E is considered the independent variable, this can be solved as a quadratic equation. The real solution for E is given by,

$$E = -c^2m_0 + c^2\sqrt{m_0^2 + \frac{2m_0|B|M}{c^2\sin^2(\alpha)}}. \tag{4.4}$$

The implementation variation for this step comes from whether to take $|B|$ from the model or an onboard magnetometer. Strictly speaking, the $|B|$ in Equation 4.3 corresponds to the magnetic field averaged over a gyration [26], but it is common practice to use $|B|$ at the spacecraft location as a simplification.

When the target E is obtained, Step 5 involves interpolating the $j(E)$ curve at the target E. This $j(E)$ curve is expressed from Step 3 in data as a series of points, and the most common approaches to interpolating involve fitting it to a smoother function and then evaluating that function at the target E. Methods of doing include (a) using a smoothing spline such as the with the `make_smoothing_spline()` function in the Python SciPy package [140], (b) fitting to a power law distribution [49], or (c) converting to units of phase space density and fitting to an exponential distribution [46]. Our experiments yielded the conclusion that a smoothing spline produced the

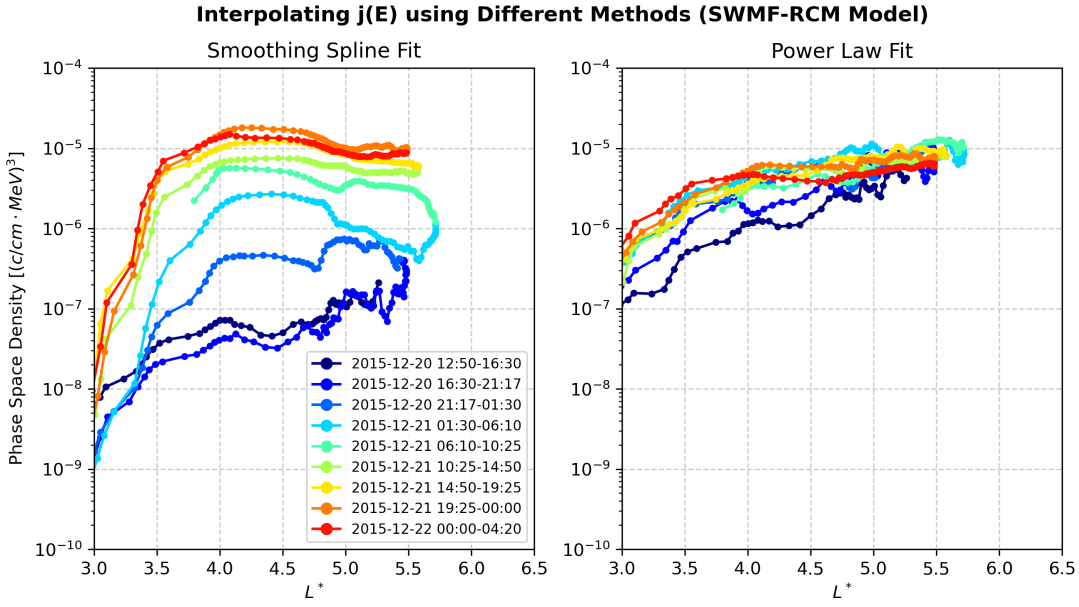

Figure 4.2: Two different options for satisfying Step 5 (Figure 4.1), which lead to very different conclusions regarding whether the event exhibits signatures of local acceleration (left) or radial transport (right). Per discussion in the text, the smoothing spline fit is the recommended option, with the power law distribution deemed a poor fit for the data observed (see Figure 4.3).

strongest results, both due to visual inspection, the smoothing spline's ability to adapt to structure in $j(E)$ without a-priori assumptions about that structure, and even the ability to adapt to reverse energy spectra with higher fluxes at higher energies [150]. Experiments were done with a non-smoothing spline (specifically a cubic spline), and it was found this degraded results over the smoothing spline due to effects of instrument noise.

In Figure 4.2 we display a phase space density analysis with this step performed using a smoothing spline and a power law fit. For this experiment, options 2a, 3c, 4a, 5a, and 7a of Figure 4.1, were used and the background model was SWMF-RCM. In this example, use of the power law distribution for interpolating $j(E)$ over a smoothing spline leads to very different conclusions regarding whether the event exhibits signatures of local acceleration (left) or radial transport (right). On the left panel, one can see a clear unimodal distribution whose peak increases in time, consistent with the local acceleration theory of Boyd et al., 2018 [22] energizing wave-particle acceleration

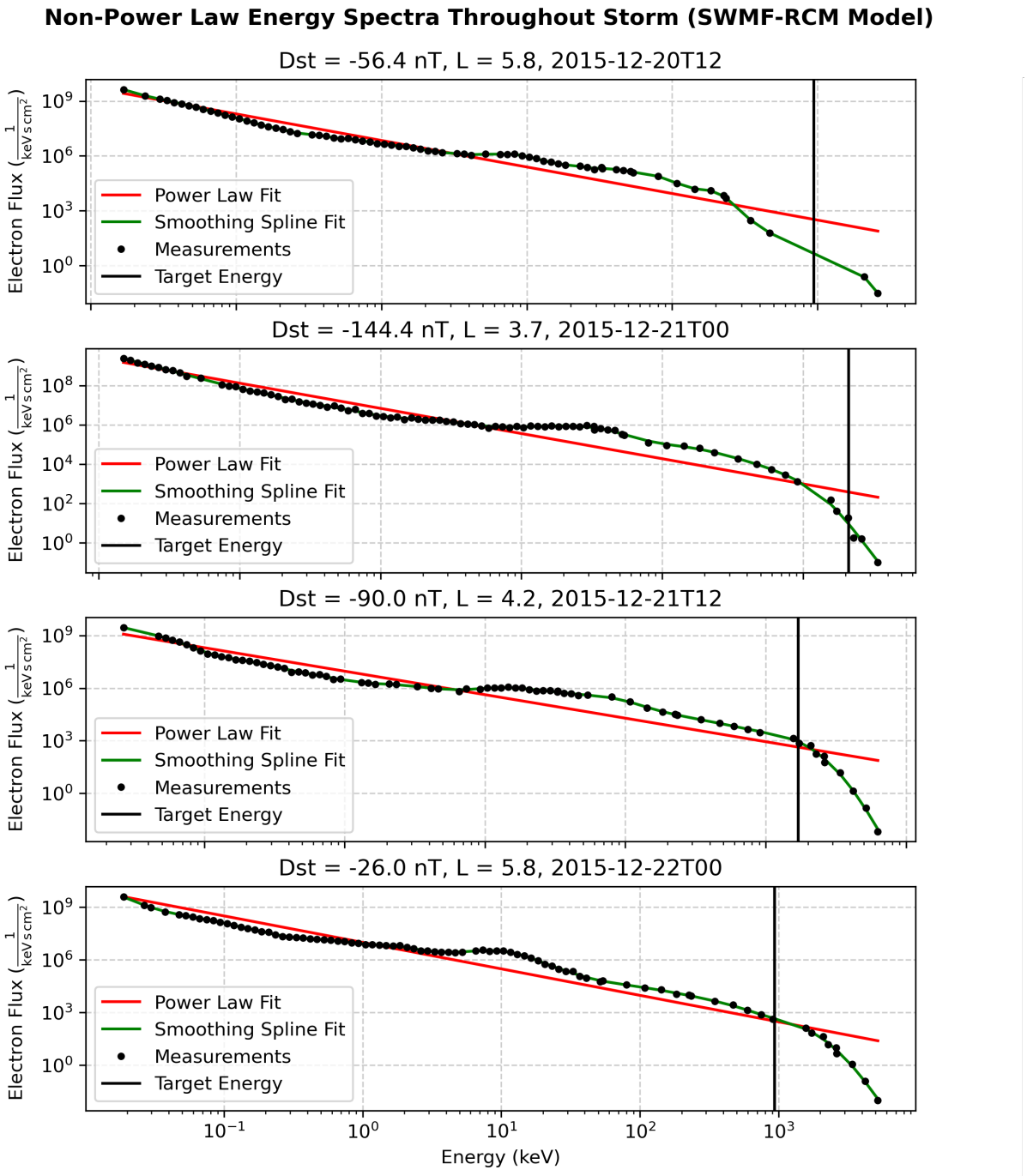

Figure 4.3: Further illustration depicting the issues with interpolating $j(E)$ using a power law distribution fit. In this plot we also notice that the target energy we interpolate (vertical black light) changes throughout a storm in response, leading to interpolation between different energy channels and possibly even between different instruments.

occurring around $L^* \sim 4.5$ in this plot. While on the right, one can see the phase space density at high $L^* \sim 5.5$ remaining high and steady, while the phase space density at lower L^* is gradually increasing consistent with radial transport acceleration [36].

The deeper issues with the power law fit of the $j(E)$ curve is displayed in Figure 4.3, showing multiple fits over the course of the same event shown in Figure 4.2 (and later in the Section 4.3.1). While the power law distribution may be an appropriate fit for certain subset energy ranges of the $j(E)$ curve, it is a poor fit for the full energy range, and yields over or under estimates in almost every panel shown. In this plot the vertical black bar, placed at the target energy E, increases during the main phase of the storm, and decreases during the recovery time in accordance to changing variables in Equation 4.4. We notice that at high energies, particularly above 1 MeV, noise is visible in the $j(E)$ data, which can be connected to lower counting statistics within the instrument. Variations of the power law fit, such as fitting only energies above 50 keV, were evaluated and yielded similarly poor results. We conclude that the smoothing spline represents the strongest approach to satisfying this step.

In Step 6, when the $j(E_0)$ flux value is found, this value is converted to phase space density using the equation the basic equation,

$$f(E_0) = j(E_0)/p^2, \tag{4.5}$$

where p is the relativistic momentum.

Now that a phase space density f has been computed for this time step, the final remaining Step 7 involves assigning a value of L^* for this point. Similar to the calculation of K in Step 2, this can be done with different codes and algorithms for computing the invariants. The implementation option we consider here is similar to Step 2, which is whether the mirror point strength B_m used in the calculation is derive using the $|B|$ from the magnetometer or $|B|$ from the model.

In Figure 4.4 we consider the effect of using $|B|$ from the magnetometer or $|B|$ from the model jointly for the entire calculation. This choice comes into play for options 2a/2b, 4a/4b, and 7a/7b. To simplify the analysis, an experiment was done where $|B|$ was always used from the magnetometer

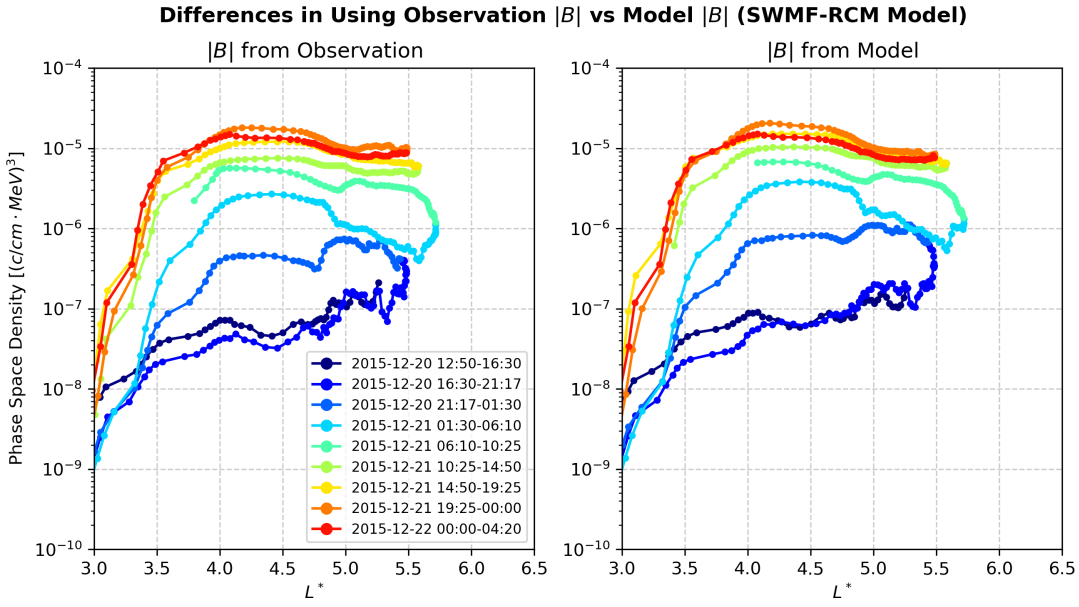

Figure 4.4: This plot shows the only very minor differences that were found when a phase space density analysis was done two ways: (left) using $|B|$ from magnetometer observation, and (right) using $|B|$ from the model. Per the implementation option numbering of Figure 4.1, the left panel depicts options 2a/4b/7a, and the right panel depicts options 2b/4b/7b.

(2a, 4b, 7a) and always from the model (2b, 4b, 7b). It was found that effect of this difference is very minor, and doing it either way leads to a similar interpretation of a growing peak event. Some minor differences in this lines appear, most notably in the line labeled 2015-12-20 21:17-01:30. This line corresponds to around the Dst minimum of the storm, where it can be expected that agreement in $|B|$ between the model and the magnetometer is most difficult. Overall, the conclusion from this study is that the difference in using $|B|$ from either magnetometer or model is of low impact on the final result, provided one avoids poor models.

We note still, that differences in L^* between models do exist, and warrant consideration. This is investigated in more detail in the next section.

4.3 Model Dependence

The three events presented here are used as canonical examples of three corresponding classes of radiation belt enhancement. These are (a) growing peak events (b) flat gradient events and (c) positive gradient events. Growing peak events are defacto examples of internal acceleration, which the other two events inviting alternate interpretation. Growing peak events are defined as those which clearly resolve a growing peak within the Van Allen Probes apogee of 5.8 R_E, while flat gradient events exhibit either flat or slightly negative gradients ($\partial f/\partial L^* \approx 0$ or $\partial f/\partial L^* < 0$) at the Van Allen Probes apogee. Positive gradient events are similar, but have positive monotonic gradients ($\partial f/\partial L^* > 0$) at the Van Allen Probes apogee.

In Boyd's study, 80 outer radiation belt events between October 2012 to April 2017 were analyzed and sorted into these three categories. A key result of that study was that 87% of those events exhibited growing peaks, which suggests that internal acceleration mechanisms are common, but perhaps not exclusively the story of what causes energetic electron enhancements in the radiation belts.

The influence of the magnetic field model enters the calculation in the final calculation of L^* (Step 7), but also more subtly when α is paired with K to determine the pitch angle which corresponds to the fixed K being analyzed (Step 1). In this section, we investigate three events previously written about in Boyd et al., 2018 [22], reproducing previous results in the literature using multiple backing magnetic field models.

In Boyd et al., 2018 the TS05 model was used. The plots displayed in this section utilize the implementation option prescription 2a/3c/4a/5a/7a per Figure 4.1, which fits the pitch angle flux distribution to Legendre polynomials, uses a smoothing spline to interpolate $j(E)$, and favors using the magnetometer $|B|$ over the model $|B|$ in every instance. Values of $M = 794$ MeV/G and $K = 0.076\ \sqrt{G R_E}$ were used in each analysis, selected to best illustrate the structural changes in the curves consistent with values used by Boyd. We also note that we use code developed with our own methodology to calculate K and L^*, which differs from what was done in Boyd et al., 2018

[22].

4.3.1 Growing Peaks Event

In Figure 4.5, we process the 20 December 2015 growing peak event processing using the TS05 (Empirical), T96 (Empirical), SWMF-RCM (MHD), and LFM-RCM (MHD) models. The solar wind $\vec{B}$ components are the Dst index visualized below are provided by the OMNI dataset [93]. During this event, we observe a southward B_z component which lasts well into the recovery period, gradually becoming less southward. We also see a B_y component which is positive around the time of Dst minimum, and becomes more negative into the recovery phase. This event was caused by a coronal mass ejection, as identified by NOAA's Space Weather Prediction Center [87].

We first notice that the values of L^* are larger for the MHD models than the empirical models, consistent with previous reports of adiabatic calculation between MHD and empirical models in Chapter 2. In that work, it was noted that ΔL^* is higher at higher L^* where the relative influence or the external field is stronger. Based on whether one trusts the empirical or MHD models more, this challenges previous results stating the range of L^* at which internal acceleration has been observed to occur [46]. The empirical models suggest a range of L^* around $3.5 - 4$, while the MHD models suggest range of $3.5 - 5$.

The MHD models show interesting structure in the recovery period of the storm, labeled in the bottom two panels, that is not visible in the empirical models. The MHD models reveal a more gradual increase in $f(L^*)$ during the recovery period that is consistent with the overall growing peak shape. This may be attributable to more dynamic recovery state and associated persistence modeling by the dynamic simulations. Should the gradual increase during recovery time calls for further investigation into whether the levels of accelerating chorus wave activity during these times are commensurate with earlier times in the event.

The astute reader may notice gaps under the LFM-RCM panel in one of the blue colored lines, within the region of $3.5 < L^* < 4.5$. Values in this region are unavailable because L^* was not able to be calculated. Specifically, at this time the LFM-RCM simulation yielded magnetic

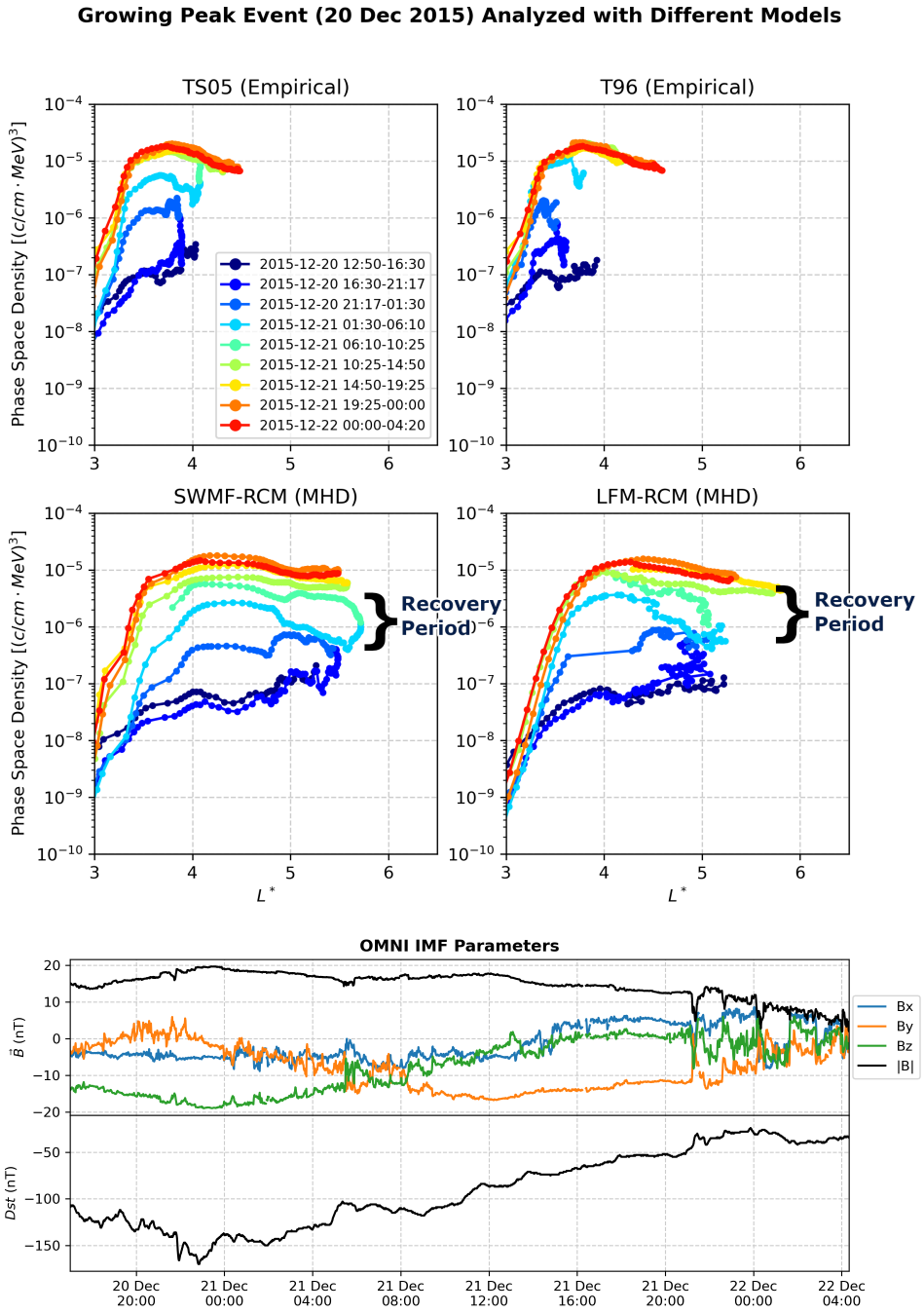

Figure 4.5: A growing peak (internal acceleration) event starting around 20 December, 2015. The phase space density analysis here is performed with four different magnetic field models, and the results from each model largely yield similar interpretations, though the MHD models show a more gradual increase in $f(L^*)$ during the labeled recovery period. Magnetic field components are in the GSM coordinate system.

topology which violated a key assumption in the Roederer method ([100]) which is used by the L^* calculation code. This assumption is that K decreases monotonically as the selected field line is moved further outward, which is the case almost always, and allows a clean search for the field line at each local time which conserves K. In the LFM-RCM simulation at this time "islands" of high $|B|$ are seen throughout the dayside magnetosphere which cause this violation.

Overall, we find that the growing peak event is still a growing peak event when processed with each of these four models. We conclude that the growing peak nature of $f(L^*)$ during this this event exhibits model independence.

4.3.2 Flat Gradients Event

In Figure 4.6 we process a flat gradient event using the four models. Though the formal definition which qualifies it as a flat gradients event is the flat or slightly negative gradient at the Van Allen Probes apogee, we also observe two peak in $f(L^*)$, with only the peak of higher L^* displaying any notable growth during the event. We notice in the bottom panels of the OMNI IMF parameters, throughout this enhancement the magnetic field components vary in time much more frequently than during the growing peak event, and the structure of the Dst index over time does not display a clear main phase and recovery period like during the growing peak event.

This event is also classified the same way when processed with different models. Again, the Tsyganenko empirical models are closer to each other than the MHD models, and the differences in scale of L^* between empirical and MHD models are visible. There are some subtle differences in how slightly negative the slope of $f(L^*)$ is in the final line at apogee between the empirical models, but all models show it being slightly negative. While the main growth in $f(L^*)$ occurs at the peak of higher L^*, there is some growth in the peak of lower L^*, and all models show about the same amount of growth. Unlikely the growing peak event in Figure 4.5, this event does not display more gradual increases to $f(L^*)$ during the recovery period.

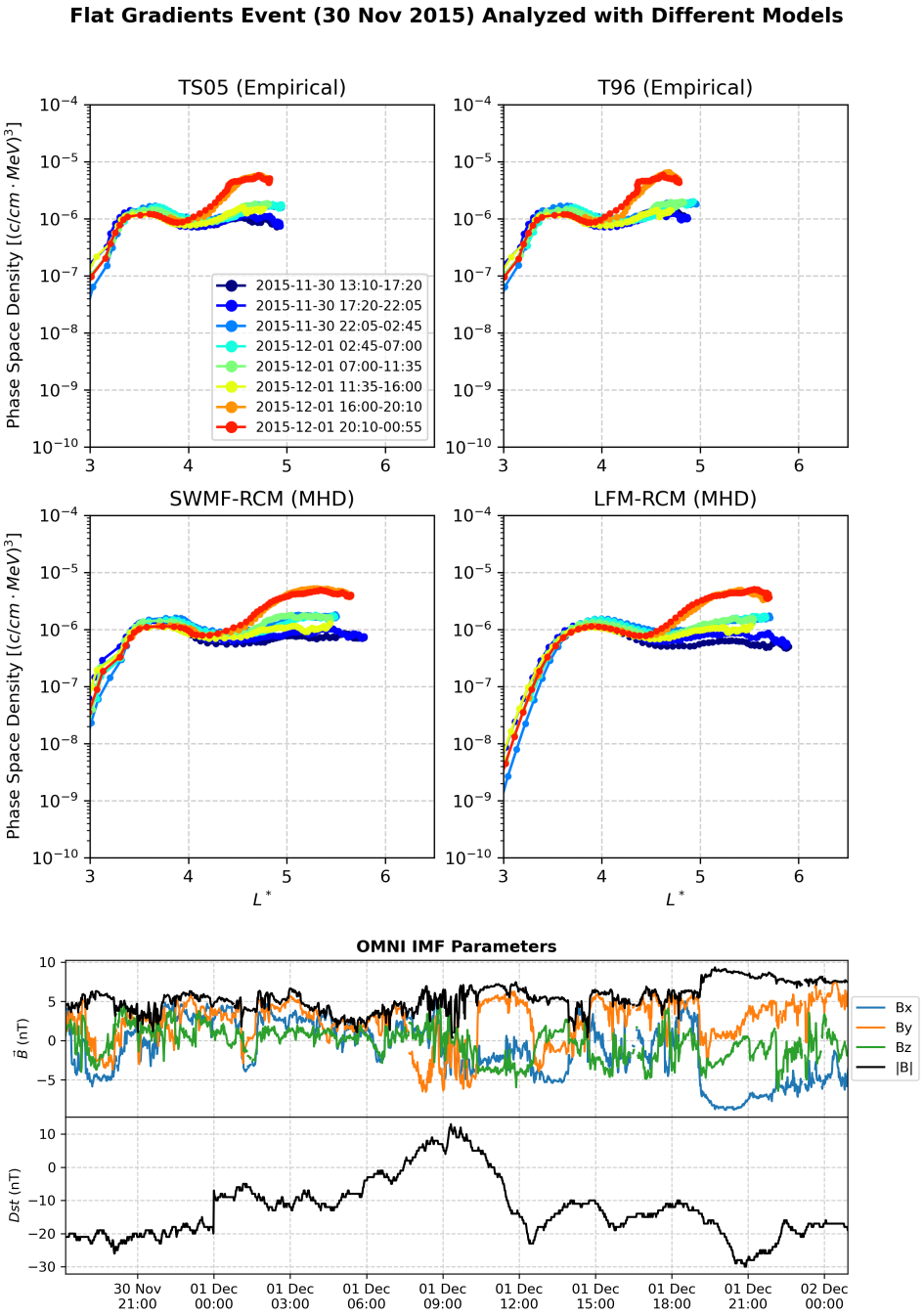

Figure 4.6: A flat gradients event starting around 30 November, 2015. The phase space density analysis here is performed with four different magnetic field models, and the results from each model largely yield similar interpretations. Magnetic field components are in the GSM coordinate system.

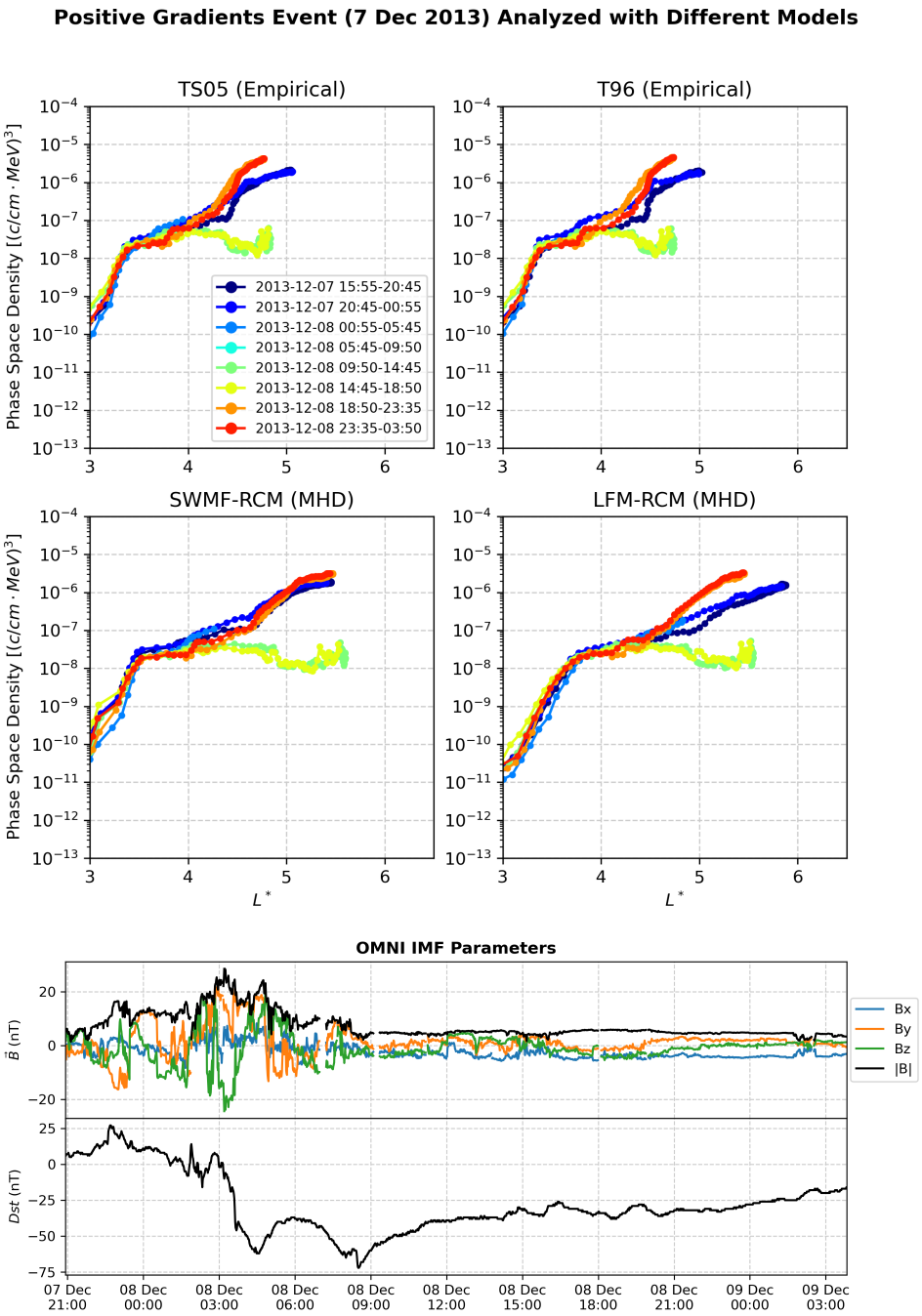

Figure 4.7: A positive gradients event starting around 7 December, 2015. The phase space density analysis here is performed with four different magnetic field models, and the results from each model largely yield similar interpretations. Magnetic field components are in the GSM coordinate system.

4.3.3 Positive Gradients Event

In Figure 4.6 we process a positive event using same four models. In [22], they note that these can sometimes revealed to be growing peak events when data at radii beyond the Van Allen

Probes apogee are used, such as through the Time History of Events and Macroscale Interactions during Substorms (THEMIS) mission [7].

The panels showing the IMF parameters indicate that progression of the Dst index for this storm, which follows the conventional pattern for a storm. Clear main phase and a recovery phase are visible, with the nuance that there is a brief interruption in the Dst index recovery around 8 December at 6:00 UT. Similar to the flat gradients event previously analyzed, the magnetic field components showed significant variation (this was not the case for the growing peak event previously analyzed). We note that this event is unlike the others in the flat gradients event in that the period of varied magnetic field eventually ceases (around 8 December at 9:00 UT), at which point the magnetic field components become more stable, and the magnetospheric response can be expected to transition towards a steady state.

In this section, we observed that processing the Van Allen Probes data using four magnetic fields models lead to similar classifications of the event type (the classes being growing peaks, flat gradients, and positive gradient types). While the classification remained unchanged, we did notice differences in the scaling of $f(L^*)$ between the different models, which implicates conclusions about the particular L^* location of individual changes to phase space density.

4.4 Summary

In this work we study the details of phase space density analysis, wherein one recasts observed flux as phase space density and puts flux in terms of the three adiabatic invariants. Different ways of doing the calculation are presented, with the common ones covered and discussed.

In our analysis of the implementation options, we demonstrated that the interpolation method for $j(E)$ lead to different conclusions as to whether our example event exhibited signatures of internal acceleration or radial transport. In our analysis of the differences to processing our example when $|B|$ from an on-board magnetometer is used over $|B|$ from the magnetic field model, we found that the differences are largely negligible.

This work also studies the degree to which the identification of signatures from phase space

density analyses depend on the magnetic field model used. We processed three events with four models each, including empirical models TS05 and T96 and coupled MHD simulations SWMF-RCM and LFM-RCM. It was found that each of the interpretations are model independent, though some notable differences can be seen in each analysis. These most notable differences are that the MHD models yielded larger values of L^* than their empirical counterparts, especially at higher cartesian radii where the external field dominates. The differences were on the scale of $\Delta L^* = 0.5 - 1.0$ at Van Allen Probe apogee. Within the growing peak event, we also observed a more gradual increase in $f(L^*)$ during the recovery of the storm with MHD models, which was distinct from the more sudden increase of $f(L^*)$ displayed with the empirical models.

In regards to the question as to whether the magnetic field model used impacts the ability to distinguish local acceleration events from radial transport events, the conclusion of this work is that the analysis is overall model independent. It is concluded, however, that use of imprecise implementation options for the steps of calculating f from the observed flux (Figure 4.1) can lead to major issues, up to and including changing the final result of what acceleration mechanism is identified from the analysis. We therefore recommend that delicate care should be taken in the steps for calculating f, and the implementation option for each step be explicitly stated in the literature.

Chapter 5

Conclusion and Future Studies

5.1 Conclusion

This dissertation touches on the adiabatic component of radiation belt dynamics. In Chapter 1, we introduced the magnetosphere, the radiation belts within, and significant open questions around the radiation belts. We reviewed the theoretical foundations of the adiabatic invariant coordinate system, which has underpinnings in dynamical systems and classical mechanics. In Chapter 2, we translated these theoretical foundations to numerical techniques solidly derived from first principles. This dissertation is not the first to numerically compute the adiabatic invariants in the context of the radiation belts. Still, it is the first to publish each step in rigorous detail in the literature, with due consideration to uncertainty and numerical artifacts. The result is a well-documented and transparent methodology worthy of building upon in future work.

In Chapter 3, we apply the methodology to quantify adiabatic motion in the magnetosphere. Through a newly developed method called invariant matching, we can track the displacement of mirror points between a starting and ending magnetic field model. This methodology can reproduce known macroscopic features of radiation belt dynamics, such as the Dst effect, drift shell splitting, and drift orbit bifurcation. These displacements are also computed in response to enhancing individual current groups within the broader magnetospheric system. Though we only visualized two-dimensional cuts, these vector fields are inherently three-dimensional objects with rich information about the morphological displacement of radiation belt populations in response to changing magnetospheric magnetic fields.

Finally, in Chapter 4, we apply the adiabatic invariant methodology as an organizing coordinate system for phase space density measurements. The purpose of this chapter is to better understand the causes of outer radiation belt electron acceleration. In particular, we consider the question by classifying observations by their corresponding signatures of pre-identified candidate mechanisms. The method of recasting measurements in terms of the adiabatic invariants has been used within the community for decades [46] [98] [106], [22]. Still, we now treat it for the first time with rigorous detail and extensive analysis of alternatives. We outline a decision tree of different implementation options (Figure 4.1), testing the effect of performing the calculation in various ways. We conclude that some decisions are trivial, but others carry drastic consequences. The dependence of the calculation on the magnetic field model used to back it is reviewed and discussed, with the reassuring conclusion that most results of the literature are valid and that the results previously demonstrated by the community are model-independent.

Each chapter of this dissertation is tied together by a dynamical systems approach and the development of rigorous numerical methodology. The methodology from Chapters 2, 3, and 4 is robust and deep. We have only begun to scratch the surface of possible applications to magnetospheric science, with many exciting prospects to come.

5.2 Future Studies

In this section, some future studies that will continue the work started in this dissertation are outlined.

5.2.1 Tracking Adiabatic Magnetopause Loss

Magnetopause loss is a process in which particles orbiting at high L^* interact with the magnetopause and break out of their trapped state. Reasons this can occur include inward magnetopause motion (such as in response to an increasing solar wind dynamic pressure), outward motion of the particles (such as due to adiabatic effects or radial diffusion), or some combination of the two. Previously, we labeled a region of the adiabatic mirror point displacement vector plot where particles

become lost to the magnetopause. In this plot, a subset of pitch angles around 90° are susceptible to magnetopause loss, while higher pitch angles are protected. This methodology could be advanced to design specific experiments to answer questions about magnetopause loss due to outward adiabatic motion. In particular, the pitch angle distribution of lost particles over time could be tracked, and this could be compared with observation. One could also ask, "How much loss is due to outward adiabatic motion versus inward magnetopause motion?" the relationship between ring current enhancement and adiabatic magnetopause loss could be investigated.

5.2.2 Quantification of Adiabatic Mass Redistribution

The displacement vector fields developed in Chapter 3 are inherently 3-D objects. Between a starting and ending magnetic field model, one can consider the adiabatic displacement vector field $\mathbf{d_a}(\mathbf{x})$. As a vector field over space that redistributed mass, it has some limited intuitive connection to a flow field, and derived variables like $\nabla \cdot \mathbf{d_a}(\mathbf{x})$ can be computed. One may ask whether large-scale changes to the magnetospheric magnetic field "bunch up" or "spread out" particles due to this adiabatic displacement field in physical space.

5.2.3 Uncertainty Quantification in Phase Space Density Analysis

Calculating $f(L^*)$ at fixed values of M and K outlined in Chapter 4 can be significantly enhanced with statistical methods to quantify the uncertainty. When a proper method for calculating the phase density is used, the remaining sources of error are in the particle measurement and the magnetic field model used.

Several approaches to quantifying the uncertainty could be applied. An ensemble approach previously employed for quantifying uncertainty in space weather modeling [28] could be employed, where the calculation is repeated with perturbed and possibly Monte-Carlo sampled variations to build a set of $f(L^*)$ estimates, S. The estimates in S can be considered a random sample of a probability distribution linked to the underlying $f(L*)$, and visualized as such. In this way, an $f(L^*)$ curve can be drawn with ± 1 σ error bars. This would help strengthen the interpretation of

the phase space density analysis, as the error bars would indicate whether a structure such as a growing peak is present in all variations of the calculation.

We will not discuss some ways we could build this set of variations S. First, a basic measure of the uncertainty in the flux measurement from Poisson counting statistics can be estimated, giving a basic (albeit not comprehensive) uncertainty on the flux measurement. This Poisson distribution could be sampled, and the calculation repeated with different flux inputs.

Next, if the TS05 model is used, previous analysis that quantifies error bars in L_1 measurements for the variables P_{dyn}, B_y, and B_z could be utilized. See Appendix C for results detailing the sensitivity of L^* to changes in these variables, and Walsh et al. 2019 [142] for a report about how error in these variables can originate from the fact that spacecraft nominally at L_1 actually orbit that point, and may be up to 100 R_E away from the sun-earth line at any given time.

5.3 Software and Data Availability

Code which implements the algorithms presented to calculate K and L^* from Chapter 2 is available as a Python package at `https://github.com/ddasilva/dasilva-invariants`. A package home page which includes both API documentation and usage examples is currently available online at `https://dasilva-invariants.readthedocs.io/`. It is recommended that future users of the package check the home page and use the latest available version for their research, and that publications which using the package acknowledge it through citation of the dissertation or journal publication associated with Chapter 2.

The original code for the TS05 model, which this work modified to allow for scaled individual currents, can be found at `https://geo.phys.spbu.ru/~tsyganenko/modeling.html`.

Data for the Qin-Denton dataset used for TS05 inputs (including W parameters) can be found at `http://mag.gmu.edu/ftp/QinDenton/5min/merged/latest/`. Data from the OMNI database is available from OMNIWeb and NASA Goddard Spaceflight Center (GSFC) Space Physics Data Facility (SPDF) at `https://omniweb.gsfc.nasa.gov/`.

Data from the GOES13 magnetometers is available online from the National Centers for Envi-

ronmental Information (NCEI) at `https://www.ngdc.noaa.gov/stp/satellite/goes/`. Runs of LFM are available on-demand from the Community Coordinate Modeling Center's (CCMC's) Run-on-Request System at `https://ccmc.gsfc.nasa.gov/models/LFM~LTR-2_1_5/`. The QinDenton dataset used for TS05 W parameters can be found at `http://mag.gmu.edu/ftp/QinDenton/5min/merged/latest/`.

Bibliography

[1] Jay M Albert, RS Selesnick, Steven Karl Morley, Michael Gerard Henderson, and AC Kellerman. Calculation of last closed drift shells for the 2013 GEM radiation belt challenge events. Journal of Geophysical Research: Space Physics, 123(11):9597–9611, 2018.

[2] Patrick Alken, Erwan Thébault, Ciarán D Beggan, Hagay Amit, J Aubert, J Baerenzung, TN Bondar, WJ Brown, S Califf, A Chambodut, et al. International geomagnetic reference field: the thirteenth generation. Earth, Planets and Space, 73(1):1–25, 2021.

[3] Hayley J Allison, Yuri Y Shprits, Irina S Zhelavskaya, Dedong Wang, and Artem G Smirnov. Gyroresonant wave-particle interactions with chorus waves during extreme depletions of plasma density in the Van Allen radiation belts. Science Advances, 7(5):eabc0380, 2021.

[4] Zeyu An, Yifan Wu, and Xin Tao. Electron dynamics in a chorus wave field generated from particle-in-cell simulations. Geophysical Research Letters, 49(3):e2022GL097778, 2022.

[5] G Anagnostopoulos, V Rigas, and E Vassiliadis. Radiation belt electron precipitation in the upper ionosphere at middle latitudes before strong earthquakes. arXiv preprint arXiv:1012.3588, 2010.

[6] BJ Anderson, RB Decker, NP Paschalidis, and T Sarris. Onset of nonadiabatic particle motion in the near-Earth magnetotail. Journal of Geophysical Research: Space Physics, 102(A8):17553–17569, 1997.

[7] Vassilis Angelopoulos. The THEMIS mission. Springer, 2009.

[8] AV Artemyev, OV Agapitov, D Mourenas, V Krasnoselskikh, and LM Zelenyi. Storm-induced energization of radiation belt electrons: Effect of wave obliquity. Geophysical Research Letters, 40(16):4138–4143, 2013.

[9] Maha Ashour-Abdalla, Raymond J Walker, Vahe Peroomian, and Mostafa El-Alaoui. On the importance of accurate solar wind measurements for studying magnetospheric dynamics. Journal of Geophysical Research: Space Physics, 113(A8), 2008.

[10] Daniel N Baker. How to cope with space weather. Science, 297(5586):1486–1487, 2002.

[11] Daniel N Baker, SG Kanekal, VC Hoxie, S Batiste, M Bolton, X Li, SR Elkington, S Monk, R Reukauf, S Steg, et al. The Relativistic Electron-Proton Telescope (REPT) instrument on board the Radiation Belt Storm Probes (RBSP) spacecraft: Characterization of Earth's radiation belt high-energy particle populations. The van allen probes mission, pages 337–381, 2014.

[12] DN Baker. What is space weather? Advances in Space Research, 22(1):7–16, 1998.

[13] DN Baker, JH Allen, SG Kanekal, and GD Reeves. Disturbed space environment may have been related to pager satellite failure. Eos, Transactions American Geophysical Union, 79(40):477–483, 1998.

[14] DN Baker, S Kanekal, JB Blake, B Klecker, and G Rostoker. Satellite anomalies linked to electron increase in the magnetosphere. Eos, Transactions American Geophysical Union, 75(35):401–405, 1994.

[15] Shanshan Bao, Wenbin Wang, Kareem Sorathia, Viacheslav Merkin, Frank Toffoletto, Dong Lin, Kevin Pham, Jeffrey Garretson, Michael Wiltberger, John Lyon, et al. The relation among the ring current, subauroral polarization stream, and the geospace plume: MAGE simulation of the 31 March 2001 super storm. Journal of Geophysical Research: Space Physics, 128(12):e2023JA031923, 2023.

[16] Christopher M Bard and John C Dorelli. Magnetotail reconnection asymmetries in an ion-scale, Earth-like magnetosphere. In Annales Geophysicae, volume 39, pages 991–1003. Copernicus GmbH, 2021.

[17] Wolfgang Baumjohann and Rudolf A Treumann. Basic space plasma physics. World Scientific, 2012.

[18] JB Blake, PA Carranza, SG Claudepierre, JH Clemmons, WR Crain, Y Dotan, JF Fennell, FH Fuentes, RM Galvan, JS George, et al. The magnetic electron ion spectrometer (MagEIS) instruments aboard the radiation belt storm probes (RBSP) spacecraft. The van Allen probes mission, pages 383–421, 2014.

[19] Daniel Boscher, Sebastien Bourdarie, Paul O'Brien, Tim Guild, Daniel Heynderickx, Steve Morley, Adam Kellerman, Christopher Roth, Hugh Evans, Antoine Brunet, Mykhaylo Shumko, Colby Lemon, Seth Claudepierre, Thomas Nilsson, Erwin De Donder, Reiner Friedel, Stu Huston, Kyungguk Min, Alexander Drozdov, and IRBEM Contributor Community. Prbem/irbem: v5.0.0, July 2022.

[20] Volker Bothmer and Ioannis A Daglis. Springer Science & Business Media, 2007.

[21] Alexander J Boyd, HE Spence, GD Reeves, HO Funsten, Ruth M Skoug, Brian Arthur Larsen, JB Blake, JF Fennell, SG Claudepierre, Daniel N Baker, et al. RBSP-ECT combined pitch angle resolved electron flux data product. Journal of Geophysical Research: Space Physics, 126(3):e2020JA028637, 2021.

[22] Alexander J Boyd, DL Turner, Geoffrey D Reeves, HE Spence, DN Baker, and JBhttps Blake. What causes radiation belt enhancements: A survey of the Van Allen Probes Era. Geophysical Research Letters, 45(11):5253–5259, 2018.

[23] Alain J Brizard and Anthony A Chan. Nonlinear relativistic gyrokinetic Vlasov-Maxwell equations. Physics of Plasmas, 6(12):4548–4558, 1999.

[24] C.A. Kletzing. Van Allen Probe A Fluxgate Magnetometer 4 second resolution data in GSM coordinates, 2022.

[25] Sidney Chapman and Vincent CA Ferraro. A new theory of magnetic storms. Nature, 126(3169):129–130, 1930.

[26] Francis F Chen et al. Introduction to plasma physics and controlled fusion, volume 1. Springer, 1984.

[27] Yue Chen, Reinhard Hans Walter Friedel, and Geoffrey D Reeves. Phase space density distributions of energetic electrons in the outer radiation belt during two Geospace Environment Modeling Inner Magnetosphere/Storms selected storms. Journal of Geophysical Research: Space Physics, 111(A11), 2006.

[28] Daniel da Silva, Charles Arge, and Shaela Jones. Predicting Solar Wind Footpoints as Probability Distributions using WSA/ADAPT. Third Triennial Earth-Sun Summit (TESS), 54(7), 2022.

[29] Daniel da Silva, Scot R Elkington, Xinlin Li, Josh Murphy, Michael James Wiltberger, and Allison N Jaynes. Tools to Calculate Adiabatic Invariants from Dynamic Simulations of Earth's Magnetosphere. In AGU Fall Meeting Abstracts, volume 2022, pages SM42D–2209, 2022.

[30] Daniel E da Silva, Scot Elkington, and Mary K Hudson. Quantifying Adiabatic Motion in the Outer Radiation Belt and Ring Current with Invariant Matching. Frontiers in Astronomy and Space Sciences, 11:1373019.

[31] Daniel E da Silva, SR Elkington, X Li, J Murphy, MK Hudson, MJ Wiltberger, and AA Chan. Numerical calculations of adiabatic invariants from mhd-driven magnetic fields. Journal of Geophysical Research: Space Physics, 129(6):e2023JA032397, 2024.

[32] D.E. da Silva, S. R. Elkington, X. Li, J. Murphy, M. J. Wiltberger, A. A. Chan, and M. K. Hudson. Numerical Calculations of Adiabatic Invariants from MHD-Driven Magnetic Fields. Journal of Geophysical Research: Space Physics, XXX:XXX, 2024.

[33] Ioannis A Daglis, Richard M Thorne, Wolfgang Baumjohann, and Stefano Orsini. The terrestrial ring current: Origin, formation, and decay. Reviews of Geophysics, 37(4):407–438, 1999.

[34] AJ Dessler and El N Parker. Hydromagnetic theory of geomagnetic storms. Journal of Geophysical Research, 64(12):2239–2252, 1959.

[35] John R Dormand and Peter J Prince. A family of embedded Runge-Kutta formulae. Journal of computational and applied mathematics, 6(1):19–26, 1980.

[36] Scot R Elkington. A review of ULF interactions with radiation belt electrons. Magnetospheric ULF waves: Synthesis and new directions, 169:177, 2006.

[37] Scot R Elkington, Mary K Hudson, and Anthony A Chan. Resonant acceleration and diffusion of outer zone electrons in an asymmetric geomagnetic field. Journal of Geophysical Research: Space Physics, 108(A3), 2003.

[38] Scot R Elkington, Mary K Hudson, Michael J Wiltberger, and John G Lyon. MHD/particle simulations of radiation belt dynamics. Journal of atmospheric and solar-terrestrial physics, 64(5-6):607–615, 2002.

[39] CP Escoubet, Michael Fehringer, and Melvyn Goldstein. Introduction the Cluster mission. In Annales Geophysicae, volume 19, pages 1197–1200. Copernicus GmbH, 2001.

[40] Erwin Fehlberg. Classical fifth-and seventh-order Runge-Kutta formulas with stepsize control. Computing, 4:93–106, 1969.

[41] Yue Fei, Anthony A Chan, Scot R Elkington, and Michael J Wiltberger. Radial diffusion and MHD particle simulations of relativistic electron transport by ULF waves in the September 1998 storm. Journal of Geophysical Research: Space Physics, 111(A12), 2006.

[42] Richard Fitzpatrick. Plasma physics: an introduction. Crc Press, 2022.

[43] Herbert O Funsten, Ruth M Skoug, Arthur Alexis Guthrie, EA MacDonald, JR Baldonado, RW Harper, Kevin C Henderson, KH Kihara, James Edward Lake, Brian Arthur Larsen, et al. Helium, Oxygen, Proton, and Electron (HOPE) mass spectrometer for the radiation belt storm probes mission. Space Science Reviews, 179:423–484, 2013.

[44] JL Gannon, X Li, and D Heynderickx. Pitch angle distribution analysis of radiation belt electrons based on Combined Release and Radiation Effects Satellite Medium Electrons A data. Journal of Geophysical Research: Space Physics, 112(A5), 2007.

[45] G Gloeckler, H Balsiger, A Bürgi, P Bochsler, LA Fisk, AB Galvin, J Geiss, F Gliem, DC Hamilton, TE Holzer, et al. The solar wind and suprathermal ion composition investigation on the WIND spacecraft. Space Science Reviews, 71:79–124, 1995.

[46] Janet C Green and MG Kivelson. Relativistic electrons in the outer radiation belt: Differentiating between acceleration mechanisms. Journal of Geophysical Research: Space Physics, 109(A3), 2004.

[47] Xudong Gu, Zhengyu Zhao, Binbin Ni, Yuri Shprits, and Chen Zhou. Statistical analysis of pitch angle distribution of radiation belt energetic electrons near the geostationary orbit: CRRES observations. Journal of Geophysical Research: Space Physics, 116(A1), 2011.

[48] G Haerendel. Diffusion Theory of Trapped Particles and the Observed Proton Distribution. Technical report, Max-Planck-Institut fuer Physik und Astrophysik, Garching, Ger., 1968.

[49] DP Hartley and MH Denton. Solving the radiation belt riddle. Astronomy & Geophysics, 55(6):6–17, 2014.

[50] M Heinemann and RA Wolf. Relationships of models of the inner magnetosphere to the Rice Convection Model. Journal of Geophysical Research: Space Physics, 106(A8):15545–15554, 2001.

[51] Michael G Henderson, Steven K Morley, Jon Niehof, Marcelo Banik, and Andrew Walker. drsteve/LANLGeoMag: v2.0.0, 2024.

[52] Mike Henderson, Steve Morley, Jon Niehof, and Brian Larsen. drsteve/lanlgeomag: v1.5.16, March 2018.

[53] D Heynderickx, B Quaghebeur, E Speelman, and E Daly. ESA's Space Environment Information System (SPENVIS): a WWW interface to models of the space environment and its effects. 2000.

[54] Richard B Horne, Richard M Thorne, Sarah A Glauert, Jay M Albert, Nigel P Meredith, and Roger R Anderson. Timescale for radiation belt electron acceleration by whistler mode chorus waves. Journal of Geophysical Research: Space Physics, 110(A3), 2005.

[55] JD Huba. Hall magnetohydrodynamics in space and laboratory plasmas. Physics of Plasmas, 2(6):2504–2513, 1995.

[56] Roger HA Iles, Nigel P Meredith, Andrew N Fazakerley, and Richard B Horne. Phase space density analysis of the outer radiation belt energetic electron dynamics. Journal of Geophysical Research: Space Physics, 111(A3), 2006.

[57] JC Ingraham, TE Cayton, RD Belian, RA Christensen, RHW Friedel, MM Meier, GD Reeves, and M Tuszewski. Substorm injection of relativistic electrons to geosynchronous orbit during the great magnetic storm of March 24, 1991. Journal of Geophysical Research: Space Physics, 106(A11):25759–25776, 2001.

[58] Allison Jaynes and Maria Usanova. The Dynamic Loss of Earth's Radiation Belts: From Loss in the Magnetosphere to Particle Precipitation in the Atmosphere. Elsevier, 2019.

[59] Allison N Jaynes, Daniel N Baker, Howard J Singer, Juan V Rodriguez, TM Loto'Aniu, AF Ali, Scot R Elkington, Xinlin Li, Shrikanth G Kanekal, Seth G Claudepierre, et al. Source and seed populations for relativistic electrons: Their roles in radiation belt changes. Journal of Geophysical Research: Space Physics, 120(9):7240–7254, 2015.

[60] May-Britt Kallenrode. Space physics: an introduction to plasmas and particles in the heliosphere and magnetospheres. Springer Science & Business Media, 2013.

[61] May-Britt Kallenrode. Space physics: an introduction to plasmas and particles in the heliosphere and magnetospheres. Springer Science & Business Media, 2013.

[62] H-J Kim, K-C Kim, S-J Noh, Larry Lyons, D-Y Lee, and W Choe. New perspective on phase space density analysis for outer radiation belt enhancements: The influence of MeV electron injections. Geophysical Research Letters, 50(14):e2023GL104614, 2023.

[63] Hee-Jeong Kim and Anthony A Chan. Fully adiabatic changes in storm time relativistic electron fluxes. Journal of Geophysical Research: Space Physics, 102(A10):22107–22116, 1997.

[64] Margaret G Kivelson and Christopher T Russell. Introduction to space physics. Cambridge university press, 1995.

[65] CA Kletzing, WS Kurth, M Acuna, RJ MacDowall, RB Torbert, T Averkamp, D Bodet, SR Bounds, M Chutter, J Connerney, et al. The electric and magnetic field instrument suite and integrated science (EMFISIS) on RBSP. Space Science Reviews, 179:127–181, 2013.

[66] Konstantinos Konstantinidis and Theodore Sarris. Calculations of the integral invariant coordinates I and L* in the magnetosphere and mapping of the regions where I is conserved, using a particle tracer (ptr3D v2. 0), LANL*, SPENVIS, and IRBEM. Geoscientific Model Development, 8(9), 2015.

[67] L Kos, RA Pitts, G Simič, M Brank, H Anand, and W Arter. SMITER: A field-line tracing environment for ITER. Fusion Engineering and Design, 146:1796–1800, 2019.

[68] Janet U Kozyra and Michael W Liemohn. Ring current energy input and decay. Magnetospheric Imaging—the Image Prime Mission, pages 105–131, 2003.

[69] Michel Kruglanski, Neophytos Messios, Erwin De Donder, Emmanuel Gamby, Stijn Calders, Laszlo Hetey, and Hugh Evans. Space environment information system (SPENVIS). In EGU General Assembly Conference Abstracts, page 7457, 2009.

[70] Shu T Lai. A critical overview on spacecraft charging mitigation methods. IEEE Transactions on Plasma Science, 31(6):1118–1124, 2003.

[71] RA Langel. International geomagnetic reference field the sixth generation. Journal of geomagnetism and geoelectricity, 44(9):679–707, 1992.

[72] Louis J Lanzerotti. Space Weather Effects on Communications: An overview of historical and contemporary impacts of solar and geospace disturbances on communications systems. Space storms and space weather hazards, pages 313–334, 2001.

[73] Zhao Li, Scot Elkington, Mary Hudson, Maulik Patel, Alex Boyd, and John Wygant. Modeling advective transport of radiation belt electrons. Journal of Atmospheric and Solar-Terrestrial Physics, 214:105509, 2021.

[74] Zhao Li, Miles Engel, Mary Hudson, Brian Kress, Maulik Patel, Murong Qin, and Richard Selesnick. Solar energetic proton access to the inner magnetosphere during the September 7–8, 2017 event. Journal of Geophysical Research: Space Physics, 126(7):e2021JA029107, 2021.

[75] Zhao Li, Mary Hudson, Maulik Patel, Michael Wiltberger, Alex Boyd, and Drew Turner. ULF wave analysis and radial diffusion calculation using a global MHD model for the 17 March 2013 and 2015 storms. Journal of Geophysical Research: Space Physics, 122(7):7353–7363, 2017.

[76] TM Loto'Aniu, HJ Singer, CL Waters, V Angelopoulos, IR Mann, SR Elkington, and JW Bonnell. Relativistic electron loss due to ultralow frequency waves and enhanced outward radial diffusion. Journal of Geophysical Research: Space Physics, 115(A12), 2010.

[77] JG Lyon, JA Fedder, and CM Mobarry. The Lyon–Fedder–Mobarry (LFM) global MHD magnetospheric simulation code. Journal of Atmospheric and Solar-Terrestrial Physics, 66(15-16):1333–1350, 2004.

[78] Susan Macmillan and Stefan Maus. International geomagnetic reference field—the tenth generation. Earth, planets and space, 57:1135–1140, 2005.

[79] BH Mauk, Nicola J Fox, SG Kanekal, RL Kessel, DG Sibeck, and a A Ukhorskiy. Science objectives and rationale for the Radiation Belt Storm Probes mission. The van Allen probes mission, pages 3–27, 2014.

[80] JP McCollough, SR Elkington, and DN Baker. The role of Shabansky orbits in compression-related electromagnetic ion cyclotron wave growth. Journal of Geophysical Research: Space Physics, 117(A1), 2012.

[81] JP McCollough, SR Elkington, ME Usanova, IR Mann, DN Baker, and ZC Kale. Physical mechanisms of compressional EMIC wave growth. Journal of Geophysical Research: Space Physics, 115(A10), 2010.

[82] Kyungguk Min, Jacob Bortnik, and Jeongwoo Lee. A novel technique for rapid L* calculation using UBK coordinates. Journal of Geophysical Research: Space Physics, 118(1):192–197, 2013.

[83] Joshua J Murphy. Advanced Analysis and Visualization of Space Weather Phenomena. PhD thesis, University of Colorado at Boulder, 2017.

[84] NASA. Aurora in new york on oct. 2, 2013, 2013.

[85] NASA Heliophysics Divison. Voyager 2 Uranus Ephemeris in Uranian U1 Coordinates, Version 1.0, 48 s Summary Data, 2023.

[86] Binbin Ni, Zhengyang Zou, Xudong Gu, Chen Zhou, Richard M Thorne, Jacob Bortnik, Run Shi, Zhengyu Zhao, Daniel N Baker, Shrikhanth G Kanekal, et al. Variability of the pitch angle distribution of radiation belt ultrarelativistic electrons during and following intense geomagnetic storms: Van Allen Probes observations. Journal of Geophysical Research: Space Physics, 120(6):4863–4876, 2015.

[87] NOAA. G2 (Moderate) Geomagnetic Storms Observed on 20 December — NOAA / NWS Space Weather Prediction Center, 2015. [Accessed 15-03-2024].

[88] Theodore G Northrop. Adiabatic charged-particle motion. Reviews of Geophysics, 1(3):283–304, 1963.

[89] Leonid Olifer, Ian R Mann, Steven Karl Morley, Louis G Ozeke, and D Choi. On the role of last closed drift shell dynamics in driving fast losses and Van Allen radiation belt extinction. Journal of Geophysical Research: Space Physics, 123(5):3692–3703, 2018.

[90] Nils Olsen, Terence J Sabaka, and Lars Tøoffner-Clausen. Determination of the IGRF 2000 model. Earth, planets and space, 52(12):1175–1182, 2000.

[91] Willard Paul Olson and Ko A Pfitzer. A quantitative model of the magnetospheric magnetic field. Journal of Geophysical Research, 79(25):3739–3748, 1974.

[92] M Kaan Öztürk and Richard A Wolf. Bifurcation of drift shells near the dayside magnetopause. Journal of Geophysical Research: Space Physics, 112(A7), 2007.

[93] Papitashvili, Natalia E.; & King, Joseph H. OMNI 1-min Data Set, 2020.

[94] Asher Pembroke, Frank Toffoletto, Stanislav Sazykin, Michael Wiltberger, John Lyon, Viacheslav Merkin, and Peter Schmitt. Initial results from a dynamic coupled magnetosphere-ionosphere-ring current model. Journal of Geophysical Research: Space Physics, 117(A2), 2012.

[95] Kevin H Pham, Binzheng Zhang, Kareem Sorathia, Tong Dang, Wenbin Wang, Viacheslav Merkin, Huixin Liu, Dong Lin, Michael Wiltberger, Jiuhou Lei, et al. Thermospheric density perturbations produced by traveling atmospheric disturbances during August 2005 storm. Journal of Geophysical Research: Space Physics, 127(2):e2021JA030071, 2022.

[96] William H Press. Numerical recipes 3rd edition: The art of scientific computing. Cambridge university press, 2007.

[97] Joachim Raeder, Douglas Larson, Wenhui Li, Emil L Kepko, and Timothy Fuller-Rowell. OpenGGCM simulations for the THEMIS mission. Space Science Reviews, 141:535–555, 2008.

[98] GD Reeves, KL McAdams, RHW Friedel, and TP O'brien. Acceleration and loss of relativistic electrons during geomagnetic storms. Geophysical Research Letters, 30(10), 2003.

[99] GD Reeves, Harlan E Spence, MG Henderson, SK Morley, RHW Friedel, HO Funsten, DN Baker, SG Kanekal, JB Blake, JF Fennell, et al. Electron acceleration in the heart of the Van Allen radiation belts. Science, 341(6149):991–994, 2013.

[100] Juan G Roederer and Hui Zhang. Dynamics of magnetically trapped particles. Springer, 2016.

[101] Shinji Saito, Yoshizumi Miyoshi, and Kanako Seki. A split in the outer radiation belt by magnetopause shadowing: Test particle simulations. Journal of Geophysical Research: Space Physics, 115(A8), 2010.

[102] Theodore E Sarris, Xinlin Li, Hong Zhao, Leng Ying Khoo, Wenlong Liu, and Michael A Temerin. On the association between electron flux oscillations and local phase space density gradients. Journal of Geophysical Research: Space Physics, 126(2):e2020JA028891, 2021.

[103] M Schulz. Canonical coordinates for radiation-belt modeling. Radiation Belts: Models and Standards, 97:153–160, 1996.

[104] Michael Schulz and Louis J Lanzerotti. Particle diffusion in the radiation belts, volume 7. Springer Science & Business Media, 1974.

[105] Norbert Sckopke. A general relation between the energy of trapped particles and the disturbance field near the Earth. Journal of Geophysical Research, 71(13):3125–3130, 1966.

[106] RS Selesnick and JB Blake. On the source location of radiation belt relativistic electrons. Journal of Geophysical Research: Space Physics, 105(A2):2607–2624, 2000.

[107] RS Selesnick and SG Kanekal. Variability of the total radiation belt electron content. Journal of Geophysical Research: Space Physics, 114(A2), 2009.

[108] VP Shabansky. Some processes in the magnetosphere. Space Science Reviews, 12(3):299–418, 1971.

[109] X Shao, Shing F Fung, Lun C Tan, Konstantinos Papadopoulos, Michael Wiltberger, and Mei-Ching Fok. Investigation of 3D energetic particle transport inside quiet-time magnetosphere using particle tracing in global MHD model. UMBC Goddard Planetary Heliophysics Institute (GPHI), 2005.

[110] MA Shea and DF Smart. Space weather: The effects on operations in space. Advances in Space Research, 22(1):29–38, 1998.

[111] Yuri Shprits, Marianne Daae, and Binbin Ni. Statistical analysis of phase space density buildups and dropouts. Journal of Geophysical Research: Space Physics, 117(A1), 2012.

[112] Yuri Y Shprits, Scot R Elkington, Nigel P Meredith, and Dmitriy A Subbotin. Review of modeling of losses and sources of relativistic electrons in the outer radiation belt I: Radial transport. Journal of Atmospheric and Solar-Terrestrial Physics, 70(14):1679–1693, 2008.

[113] Yuri Y Shprits, Dmitriy A Subbotin, Nigel P Meredith, and Scot R Elkington. Review of modeling of losses and sources of relativistic electrons in the outer radiation belt II: Local acceleration and loss. Journal of atmospheric and solar-terrestrial physics, 70(14):1694–1713, 2008.

[114] J-H Shue, P Song, CT Russell, JT Steinberg, JK Chao, G Zastenker, OL Vaisberg, S Kokubun, HJ Singer, TR Detman, et al. Magnetopause location under extreme solar wind conditions. Journal of Geophysical Research: Space Physics, 103(A8):17691–17700, 1998.

[115] DG Sibeck, RW McEntire, ATY Lui, RE Lopez, and SM Krimigis. Magnetic field drift shell splitting: Cause of unusual dayside particle pitch angle distributions during storms and substorms. Journal of Geophysical Research: Space Physics, 92(A12):13485–13497, 1987.

[116] Artem G Smirnov, Elena A Kronberg, Patrick W Daly, Nikita A Aseev, Yuri Y Shprits, and Adam C Kellerman. Adiabatic invariants calculations for Cluster mission: A long-term product for radiation belts studies. Journal of Geophysical Research: Space Physics, 125(2):e2019JA027576, 2020.

[117] Harlan E Spence, Geoffrey D Reeves, DN Baker, JB Blake, M Bolton, S Bourdarie, AA Chan, SG Claudepierre, JH Clemmons, JP Cravens, et al. Science goals and overview of the radiation belt storm probes (RBSP) energetic particle, composition, and thermal plasma (ECT) suite on NASA's Van Allen probes mission. Space Science Reviews, 179:311–336, 2013.

[118] Frances A Staples, A Kellerman, Kyle Robert Murphy, I Jonathan Rae, Jasmine Kaur Sandhu, and Colin Forsyth. Resolving magnetopause shadowing using multimission measurements of phase space density. Journal of Geophysical Research: Space Physics, 127(2):e2021JA029298, 2022.

[119] Richard Mansergh Thorne. Radiation belt dynamics: The importance of wave-particle interactions. Geophysical Research Letters, 37(22), 2010.

[120] RM ea Thorne, W Li, B Ni, Q Ma, J Bortnik, L Chen, DN Baker, Harlan E Spence, GD Reeves, MG Henderson, et al. Rapid local acceleration of relativistic radiation-belt electrons by magnetospheric chorus. Nature, 504(7480):411–414, 2013.

[121] Frank Toffoletto, Stanislav Sazykin, Robert Spiro, and Richard Wolf. Inner magnetospheric modeling with the Rice Convection Model. Space science reviews, 107:175–196, 2003.

[122] Gábor Tóth, Igor V Sokolov, Tamas I Gombosi, David R Chesney, C Robert Clauer, Darren L De Zeeuw, Kenneth C Hansen, Kevin J Kane, Ward B Manchester, Robert C Oehmke, et al. Space Weather Modeling Framework: A new tool for the space science community. Journal of Geophysical Research: Space Physics, 110(A12), 2005.

[123] Gábor Tóth, Bart Van der Holst, Igor V Sokolov, Darren L De Zeeuw, Tamas I Gombosi, Fang Fang, Ward B Manchester, Xing Meng, Dalal Najib, Kenneth G Powell, et al. Adaptive numerical algorithms in space weather modeling. Journal of Computational Physics, 231(3):870–903, 2012.

[124] NA Tsyganenko. Methods for quantitative modeling of the magnetic field from Birkeland currents. Planetary and space science, 39(4):641–654, 1991.

[125] NA Tsyganenko. Modeling the Earth's magnetospheric magnetic field confined within a realistic magnetopause. Journal of Geophysical Research: Space Physics, 100(A4):5599–5612, 1995.

[126] NA Tsyganenko. A model of the near magnetosphere with a dawn-dusk asymmetry 1. Mathematical structure. Journal of Geophysical Research: Space Physics, 107(A8):SMP–12, 2002.

[127] NA Tsyganenko. A model of the near magnetosphere with a dawn-dusk asymmetry 1. Mathematical structure. Journal of Geophysical Research: Space Physics, 107(A8):SMP–12, 2002.

[128] NA Tsyganenko. A model of the near magnetosphere with a dawn-dusk asymmetry 2. Parameterization and fitting to observations. Journal of Geophysical Research: Space Physics, 107(A8):SMP–10, 2002.

[129] NA Tsyganenko and Toshifumi Mukai. Tail plasma sheet models derived from Geotail particle data. Journal of Geophysical Research: Space Physics, 108(A3), 2003.

[130] NA Tsyganenko and MI Sitnov. Modeling the dynamics of the inner magnetosphere during strong geomagnetic storms. Journal of Geophysical Research: Space Physics, 110(A3), 2005.

[131] NA Tsyganenko and MI Sitnov. Magnetospheric configurations from a high-resolution data-based magnetic field model. Journal of Geophysical Research: Space Physics, 112(A6), 2007.

[132] Nikolai A Tsyganenko. A magnetospheric magnetic field model with a warped tail current sheet. Planetary and Space Science, 37(1):5–20, 1989.

[133] Nikolai A Tsyganenko and David P Stern. Modeling the global magnetic field of the large-scale Birkeland current systems. Journal of Geophysical Research: Space Physics, 101(A12):27187–27198, 1996.

[134] No A Tsyganenko. Effects of the solar wind conditions in the global magnetospheric configurations as deduced from data-based field models. In International conference on substorms, volume 389, page 181, 1996.

[135] Weichao Tu, Richard Selesnick, Xinlin Li, and Mark Looper. Quantification of the precipitation loss of radiation belt electrons observed by SAMPEX. Journal of Geophysical Research: Space Physics, 115(A7), 2010.

[136] DL Turner, Vassilis Angelopoulos, Wen Li, MD Hartinger, Maria Usanova, IR Mann, Jacob Bortnik, and Yuri Shprits. On the storm-time evolution of relativistic electron phase space density in Earth's outer radiation belt. Journal of Geophysical Research: Space Physics, 118(5):2196–2212, 2013.

[137] AY Ukhorskiy, BJ Anderson, K Takahashi, and NA Tsyganenko. Impact of ULF oscillations in solar wind dynamic pressure on the outer radiation belt electrons. Geophysical research letters, 33(6), 2006.

[138] AY Ukhorskiy, K Takahashi, BJ Anderson, and H Korth. Impact of toroidal ULF waves on the outer radiation belt electrons. Journal of Geophysical Research: Space Physics, 110(A10), 2005.

[139] AL Vampola. Outer zone energetic electron environment update. In Conference on the high energy radiation background in space. Workshop record, pages 128–136. IEEE, 1998.

[140] Pauli Virtanen, Ralf Gommers, Travis E Oliphant, Matt Haberland, Tyler Reddy, David Cournapeau, Evgeni Burovski, Pearu Peterson, Warren Weckesser, Jonathan Bright, et al. SciPy 1.0: fundamental algorithms for scientific computing in Python. Nature methods, 17(3):261–272, 2020.

[141] Andrew P Walsh, Stein Haaland, Colin Forsyth, Amy M Keesee, Jennifer Kissinger, Kun Li, Andrei Runov, Josef Soucek, Brian M Walsh, Simon Wing, et al. Dawn–dusk asymmetries in the coupled solar wind–magnetosphere–ionosphere system: A review. In Annales Geophysicae, volume 32, pages 705–737. Copernicus GmbH, 2014.

[142] BM Walsh, T Bhakyapaibul, and Y Zou. Quantifying the uncertainty of using solar wind measurements for geospace inputs. Journal of Geophysical Research: Space Physics, 124(5):3291–3302, 2019.

[143] Elden C Whipple Jr. (U, B, K) coordinates: A natural system for studying magnetospheric convection. Journal of Geophysical Research: Space Physics, 83(A9):4318–4326, 1978.

[144] M Wiltberger, TI Pulkkinen, JG Lyon, and CC Goodrich. MHD simulation of the magnetotail during the December 10, 1996, substorm. Journal of Geophysical Research: Space Physics, 105(A12):27649–27663, 2000.

[145] Y Yu, J Koller, and SK Morley. Quantifying the effect of magnetopause shadowing on electron radiation belt dropouts. In Annales geophysicae, volume 31, pages 1929–1939. Copernicus Publications Göttingen, Germany, 2013.

[146] Yiqun Yu, Josef Koller, Sorin Zaharia, and Vania Jordanova. L* neural networks from different magnetic field models and their applicability. Space Weather, 10(2), 2012.

[147] Yiqun Yu and Aaron J Ridley. Validation of the space weather modeling framework using ground-based magnetometers. Space Weather, 6(5), 2008.

[148] Binzheng Zhang, Kareem A Sorathia, John G Lyon, Viacheslav G Merkin, Jeffrey S Garretson, and Michael Wiltberger. GAMERA: A three-dimensional finite-volume MHD solver for non-orthogonal curvilinear geometries. The Astrophysical Journal Supplement Series, 244(1):20, 2019.

[149] H Zhao, DN Baker, X Li, AN Jaynes, and SGhttps Kanekal. The acceleration of ultrarelativistic electrons during a small to moderate storm of 21 April 2017. Geophysical Research Letters, 45(12):5818–5825, 2018.

[150] H Zhao, B Ni, X Li, DN Baker, WR Johnston, W Zhang, Z Xiang, X Gu, AN Jaynes, SG Kanekal, et al. Plasmaspheric hiss waves generate a reversed energy spectrum of radiation belt electrons. Nature Physics, 15(4):367–372, 2019.

Appendix A

OMNI IMF Parameters during 2 October 2013 Storm

The IMF parameters propagated from L1 observations to the bow shock by the OMNI data product show the type of incoming solar wind during the storm as seen in Figure A.1. This data was taken from the OMNI database (`https://omniweb.gsfc.nasa.gov/`). The CME-driven enhancement associated with abrupt increases in IMF number density and velocity occurred around 2 October at 06:00. Following this abrupt increase, the IMF number density reduced to a nominal state, while the solar wind speed gradually decreased over the next few days. Around 3 October at 18:00 is a "blip" of increased IMF number density with in-trend IMF velocities, increasing the IMF dynamic pressure and affecting L^* in the tail, as shown in Figure 2.8.

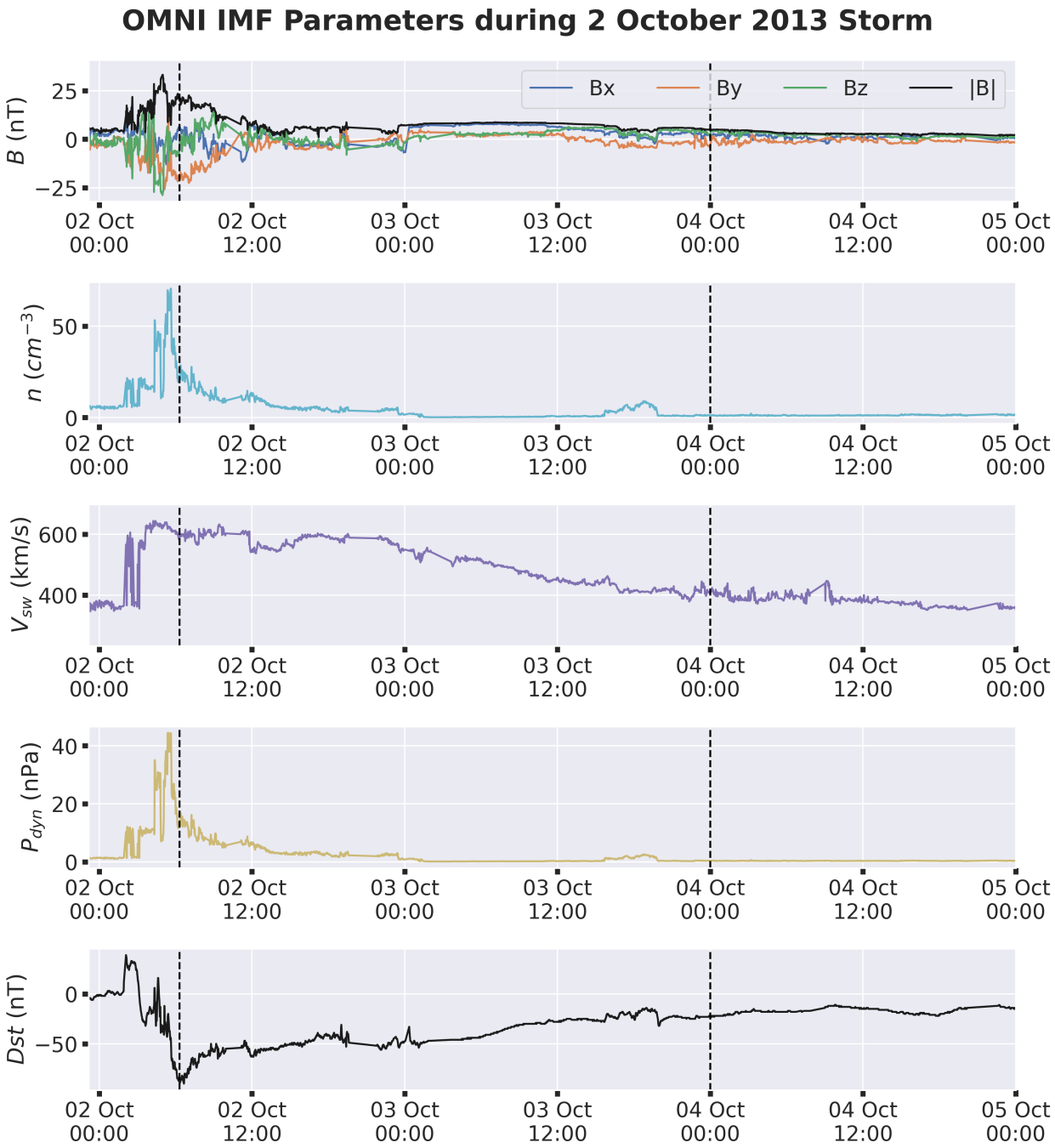

Figure A.1: OMNI IMF Parameters during the 2 October 2013 storm. This data was taken from the OMNI database, which propagates satellite observations of the upstream solar wind at the L1 point to Earth's bow shock for geomagnetic storm analysis. The two vertical bars identify the minimum D_{st} (left vertical bar) and the quiet period referenced in Figures 2.1 and 2.6.

Appendix B

Example of Non-Closed Drift Shell

The calculation of L^* is only valid for trapped particle radiation and when the magnetic field changes slowly compared to the drift period. However, during particular disturbed periods of the magnetosphere, previously trapped particles will no longer be trapped and will escape along open field lines. Furthermore, during particularly disturbed periods, the magnetic field will change much faster than the drift period, and using one snapshot of the magnetospheric magnetic field will be insufficient to describe the particle's trajectory.

Here, we illustrate one example of a particularly disturbed magnetosphere, illustrated by an equatorial slice of the TS05 empirical model during the 2 October 2013 storm. In this plot, the colors correspond to the log-scale magnetic field intensity, and the black lines are isolines of magnetic field intensity drawn at cubically decreasing intensity levels.

We recall that particles with 90° pitch angles will orbit along isolines of B_{min}. However, in this plot, we see that night-side "islands" of magnetic field intensity exist in the equatorial plane, which would prevent such a trajectory from making a complete orbit around the Earth. The drift shell calculation description in Chapter 2 describes visiting each magnetic local time assuming a complete orbit is made. However, that will not be the case in a field such as this.

Additionally, on the dayside, we encounter what we refer to as "reversals" in the equatorial magnetic field intensity isolines. These reversals are in direct conflict with the drift shell calculation. The calculation assumes that each magnetic local time is visited only once, making the drift shell convex. However, if the isolines of B reverse direction, the drift shell becomes concave, and a single

drift shell distance for that magnetic local time is no longer sufficient.

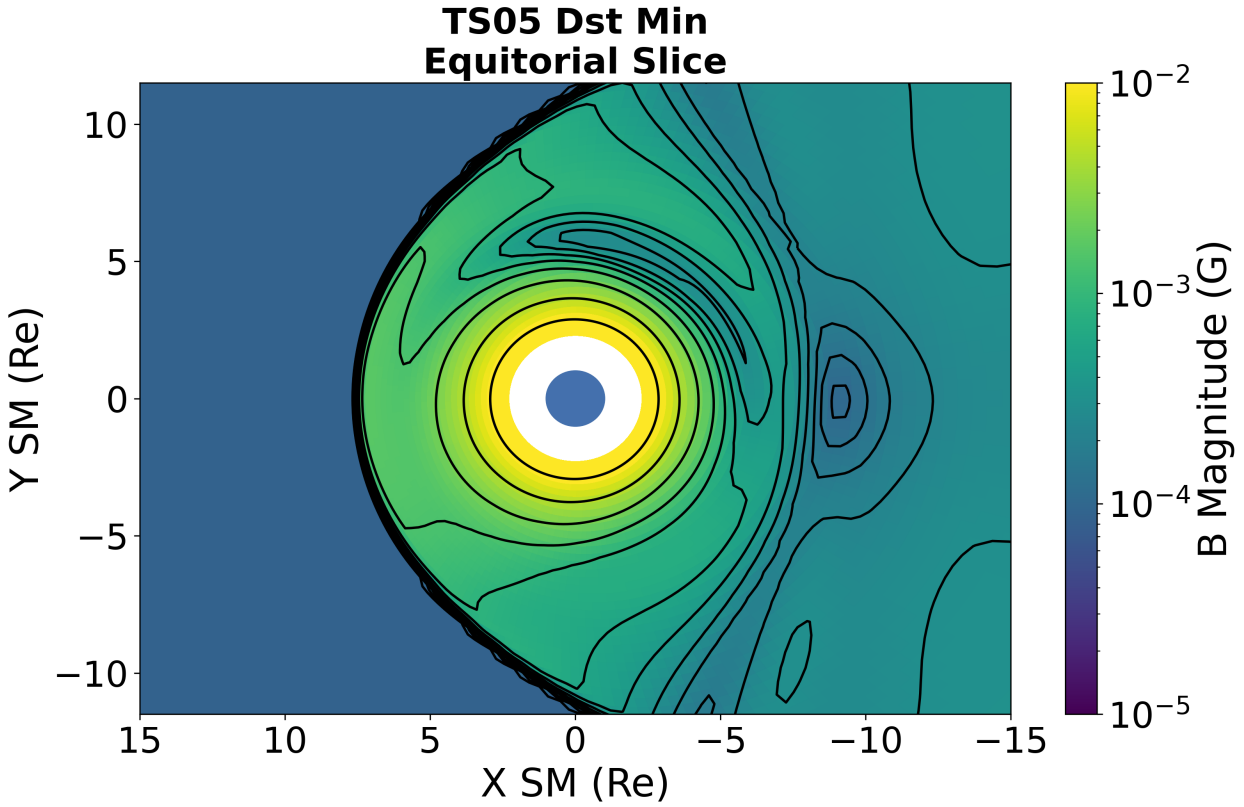

Figure B.1: An example of a non-closed drift shell exhibits at least two features that complicate the calculation of the drift shell and, in turn, L^*. First, night-side "islands" of equatorial magnetic field intensity exist on the nightside, which would prevent particles mirroring at B_{min} from making a complete orbit around Earth. Secondly, on the dayside, there exist reversals in the direction of the equatorial magnetic field intensity isolines, which prevent the drift shell from being convex (a condition required for our algorithm).

Appendix C

Influence of Solar Wind Measurement Error on L^* with TS05

The TS05 and T96 models are driven by measurements of the Dst index and solar wind at the location of the foreshock. The solar wind parameters, including B_y, B_z, and the dynamic pressure P_{dyn}, are typically measured at the L_1 location by a satellite such as ACE or WIND and propagated to the foreshock using physical modeling such as in the OMNI data product.

The measurement of these variables is not without error. Previous work by Walsh et al., 2019 [142] studied the uncertainty associated with using solar wind measurements for geospace modeling inputs. Similar work appears in Ashour-Abdalla et al., 2008 [9], where the influence of solar wind errors was considered concerning MHD simulations. Issues with measuring the solar wind at L_1 and propagating to the foreshock include (a) the fact that spacecraft nominally located at L_1 orbit that point and may be up to 100 R_E off the spacecraft-sun line, (b) the plasma may undergo significant changes between L_1 and the foreshock which are difficult to capture using propagation algorithms. An illustration of the relative sizes of ACE and WIND's orbit compared to the magnetosphere can be found in Figure C.1.

For instance, Walsh et al., 2019 [142] displays an interval where two different spacecraft nominally at L_1 (ACE and WIND) make simultaneous measurements of solar wind but notably report opposing signs for B_y and B_z (with $B_z \approx \pm 3$ nT and $B_y \approx \pm 1$ nT). In their comparison of ACE and WIND measurements, it was found that P_{dyn} differed between the two satellites with a mean of 0.45 nPa and a standard deviation of 0.67 nPa, and the clock angle $\theta_{clock} = \tan^{-1}(\frac{B_y}{B_z})$ differed with a mean of 38.4 degrees.

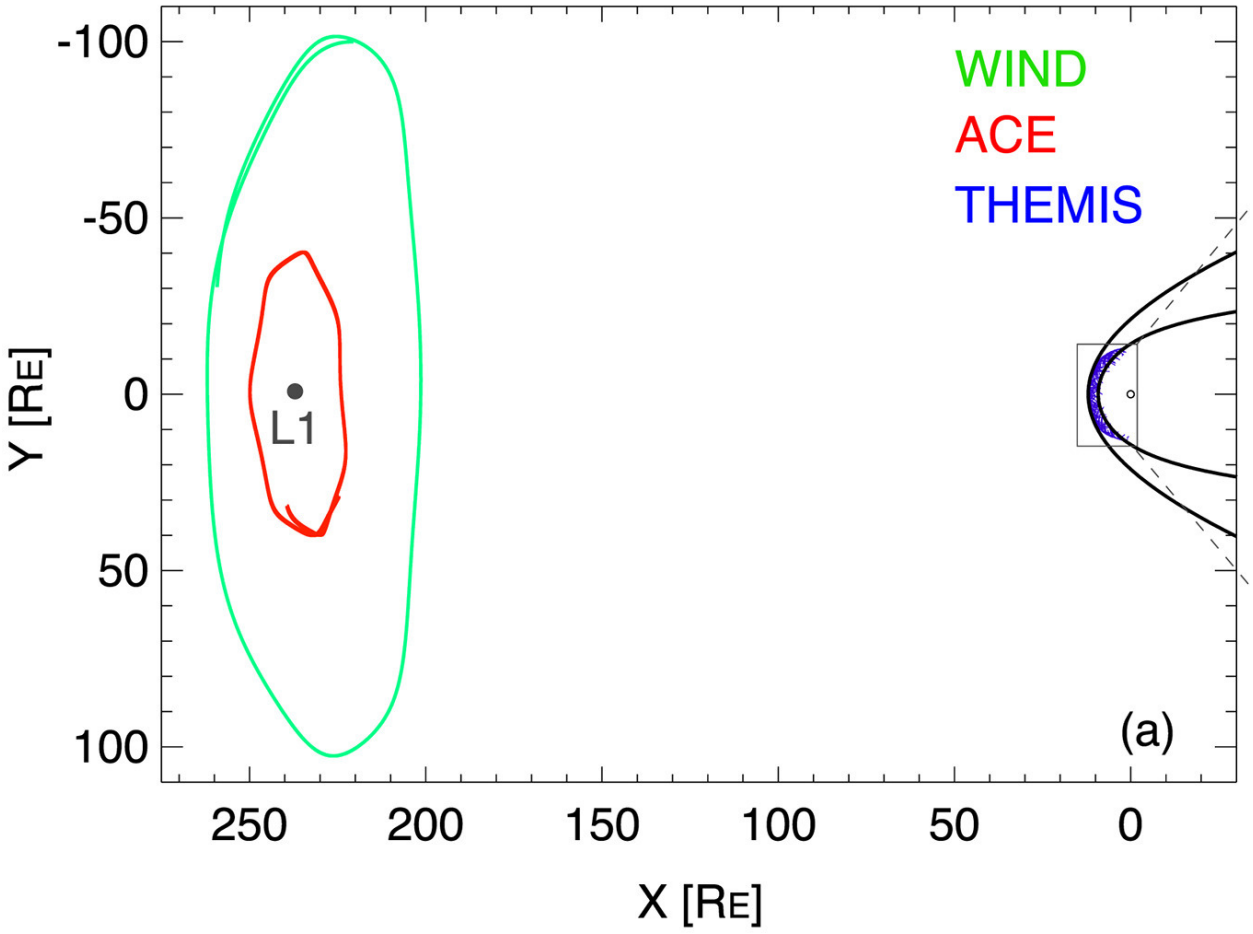

Figure C.1: The Relative sizes of the ACE/WIND orbits compared to Earth's magnetosphere. Image taken from Walsh et al., 2019 [142]

.

Since the focus of this dissertation is on the calculation and associated analyses using the adiabatic invariants, and a common driver of that calculation is using empirical models like TS05 driven by L_1 solar wind measurements, it is prudent to study the effect of input errors on the resultant adiabatic invariants. In this appendix, we will look at how L^* changes as different input parameters to the TS05 model are varied to simulate errors in the upstream input data source. Though the Dst index measurement is not identified as much of an issue as the solar wind measurement error, results for the Dst index are included here for completeness.

To study this, we designed the following experiment using TS05. We took a nominal set of inputs corresponding to typical solar wind conditions, varied each parameter, and recalculated L^*. This is repeated for multiple starting points extending along the nightside $-X$ axis (SM Coordinates) to display the radial dependence. The nominal set of inputs is $P_{dyn} = 4.18$ nPa (corresponding to $n = 10$ cm^{-3} and $v = 500$ km/s), $B_y = B_z = 5$ nT, and $W_1 = W_2 = W_3 = W_4 = W_5 = W_6 = 0$. The results are calculated from 1 January 2023 for a particle with an equatorial pitch angle $\alpha_{eq} = 45°$.

Overall, given the scale errors reported by Walsh et al. 2019, the downstream effect of miscalculating L^* is limited. In Figure C.2, we see a strong dependence of L^* on P_{dyn}, especially further out into the magnetosphere, but the relative change in L^* is small. The same is true when considering errors in B_y and B_z.

A by-product of this analysis is that with TS05, the influence of B_z is much more significant on the resultant L^* than B_y; changing B_y had little effect. While not a solar wind parameter, we display a comparable analysis for the Dst index in Figure C.5. This plot similarly found that the L^* response to changes in the Dst index is greater further out into the magnetosphere. Still, appreciable differences do not occur within the realm in which error is expected to exist.

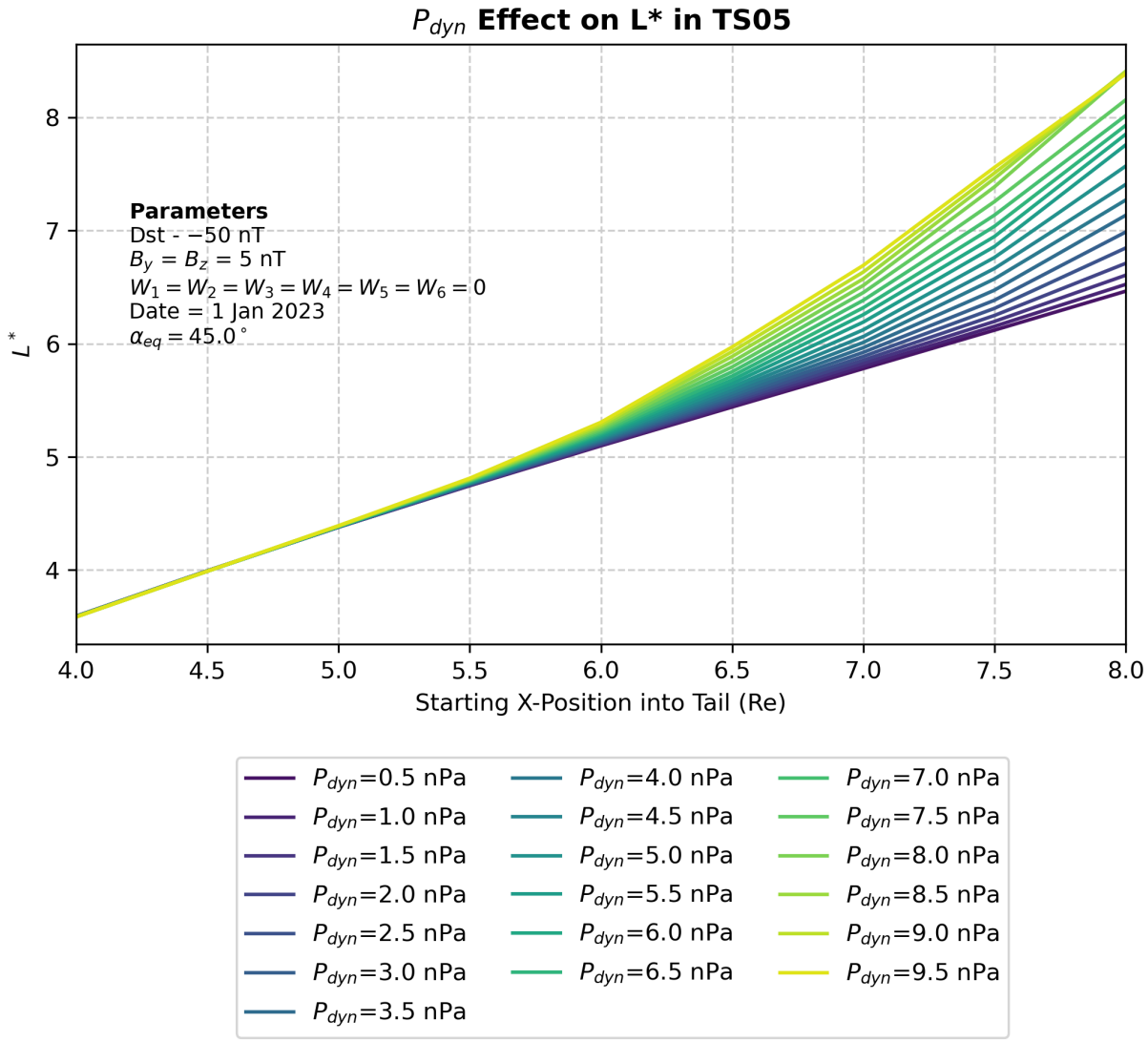

Figure C.2: Changes to L^* using TS05 as the solar wind dynamic pressure P_{dyn} changes and other inputs are held constant.

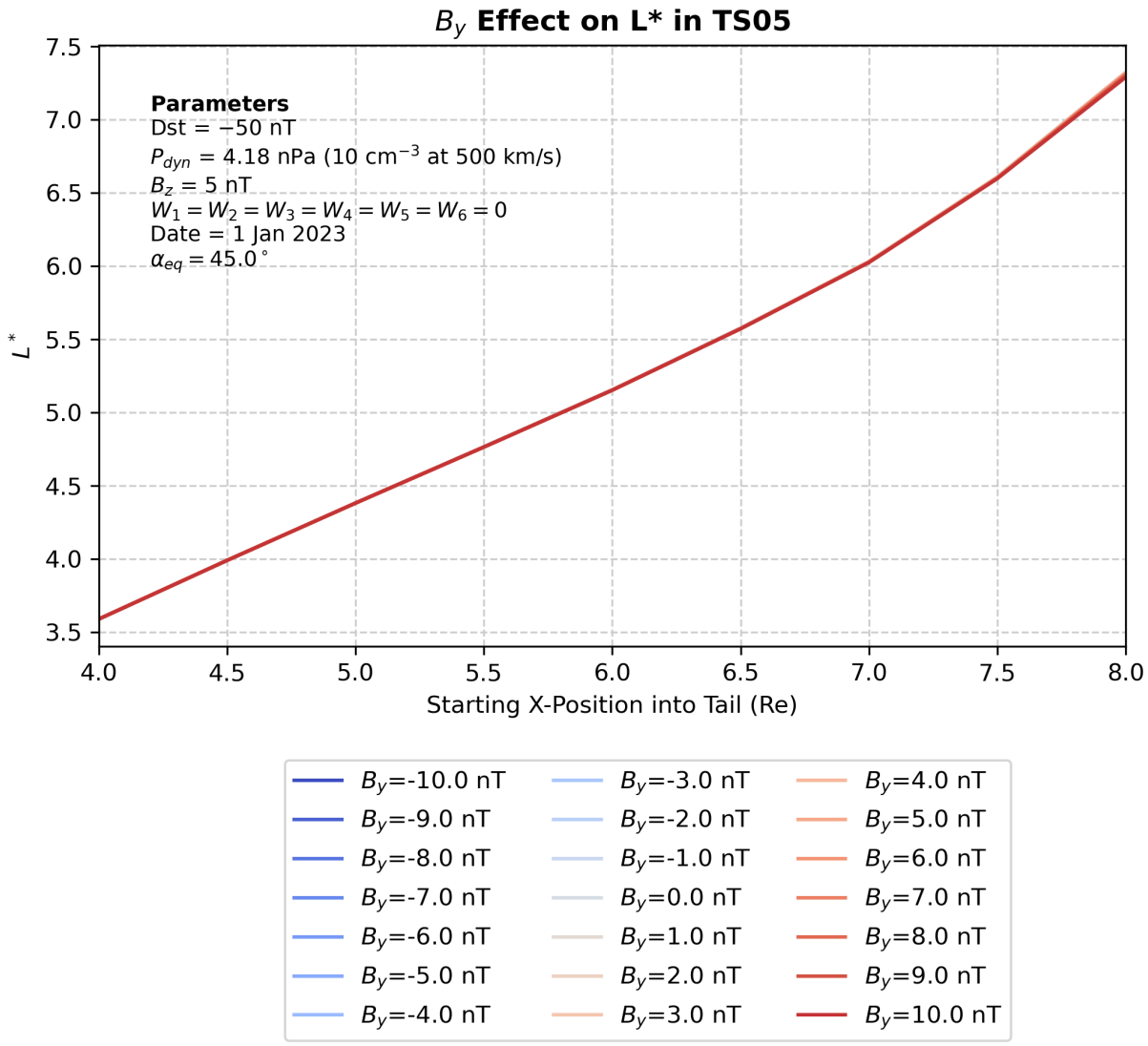

Figure C.3: Changes to L^* using TS05 as the IMF B_y (GSM) changes and other inputs are held constant.

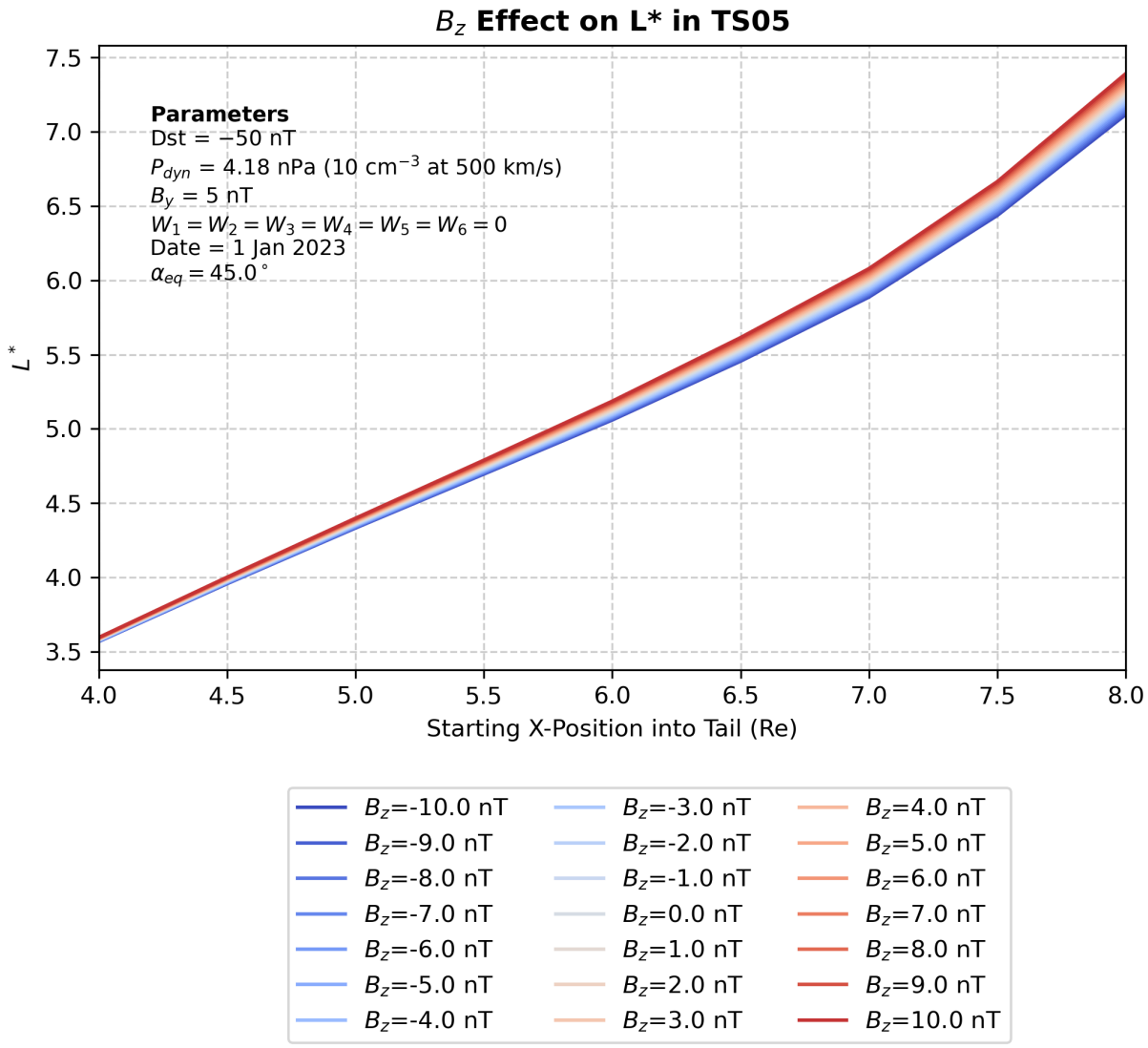

Figure C.4: Changes to L^* using TS05 as the IMF B_z (GSM) changes and other inputs are held constant.

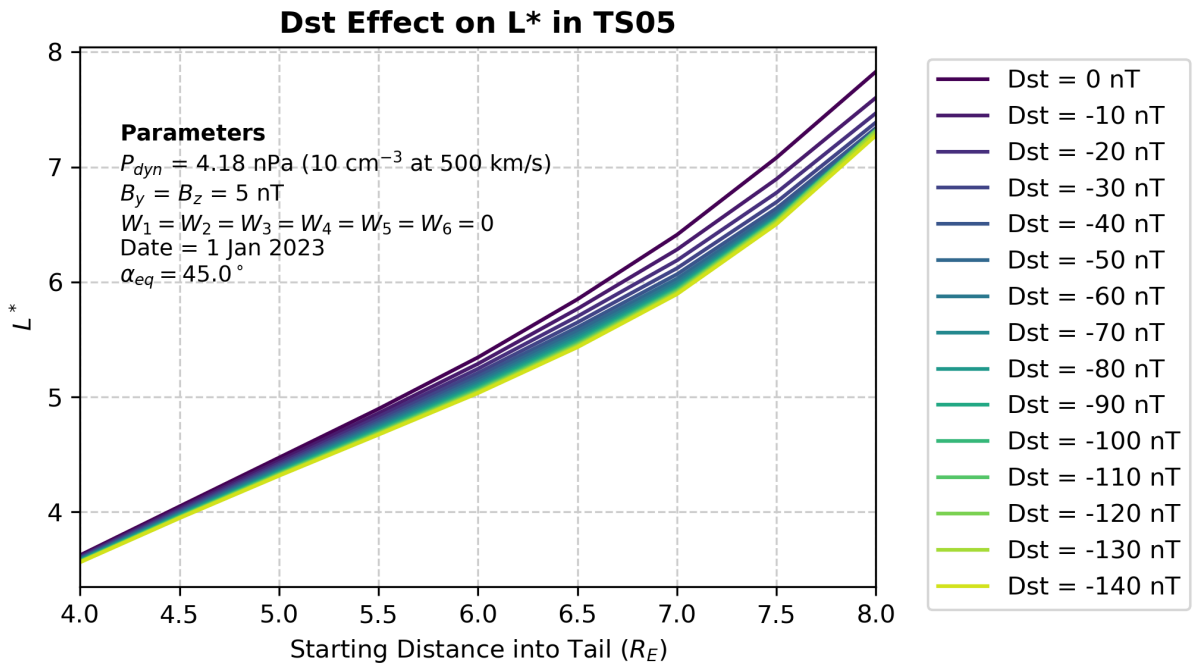

Figure C.5: Changes to L^* using TS05 as the Dst index changes and other inputs are held constant.

Appendix D

Grid Comparison for Magnetic Field Models

In this Appendix, we visually compare the grids used for comparing phases space density analysis in Chapter 4. There are two grids used: the native LFM grid, and a rectangular grid. The rectangular grid is used with SWMF, TS05, and T96 unless otherwise noted (in some cases, TS05 and T96 are evaluated on the LFM grid). For SWMF, the data is regridded to the rectangular grid. For TS05 and T96, the model is evaluated at each grid point.

Overall, the grids are of comparable resolution within the relevant region of the Van Allen Probes orbit ($r < 5.8\ R_E$). This is true for all local times. For this reason, the differing grids should not be an issue when comparing the resultant phase space density analysis from the different models.

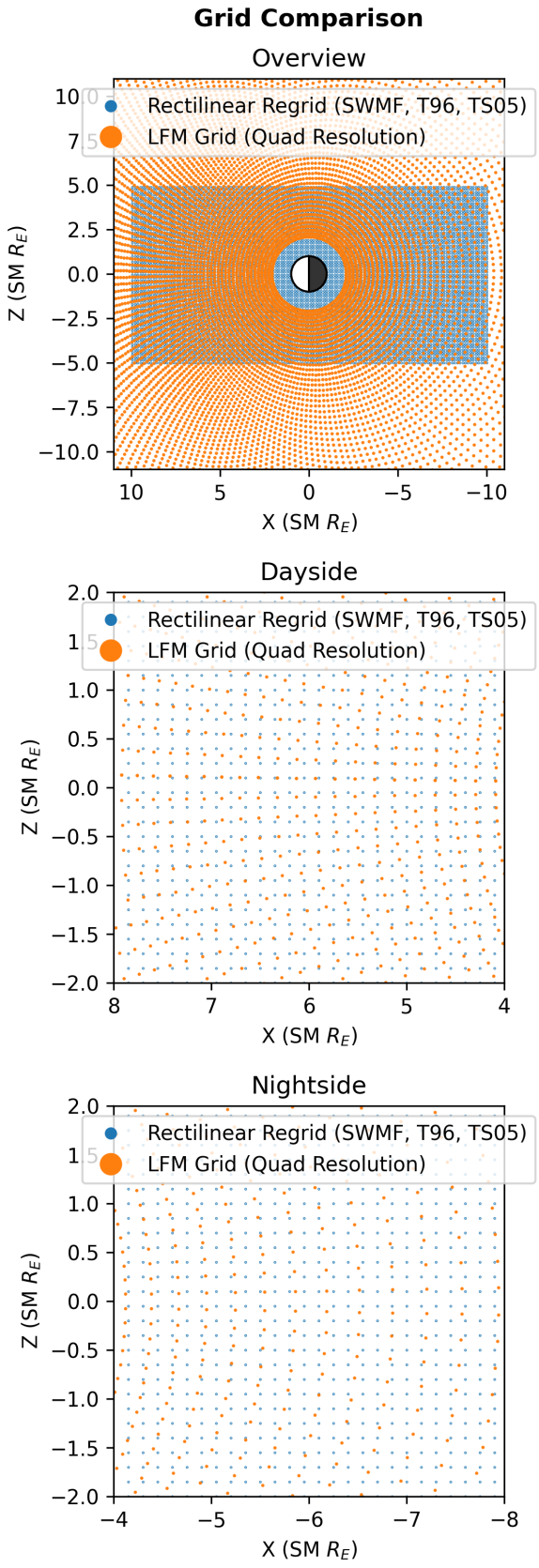

Figure D.1: Comparison of the grids used between the rectangular grid (regridded SWMF and evaluation grid for TS05 and T96) and the native LFM grid.